UC San Diego
UC San Diego Electronic Theses and Dissertations

Title

Nanoporous, Transparent, and Doped Magnesium Aluminate Spinel – Nanostructural Flexibility by Densification of Metastable Powders

Permalink

Author

Dewitt, Darren Michael

Publication Date

2021

Peer reviewed|Thesis/dissertation

UNIVERSITY OF CALIFORNIA SAN DIEGO

**NANOPOROUS, TRANSPARENT, AND DOPED MAGNESIUM ALUMINATE SPINEL –
NANOSTRUCTURAL FLEXIBILITY BY DENSIFICATION OF METASTABLE POWDERS**

A dissertation submitted in partial satisfaction of the

requirements for the degree

Doctor of Philosophy

in

Materials Science and Engineering

by

Darren Michael Dewitt

Committee in charge:

       Professor Javier E. Garay, Chair
       Professor Olivia A. Graeve
       Professor Jian Luo
       Professor Marc Meyers
       Professor Vitali Nesterenko

2021

The dissertation of Darren Michael Dewitt is approved, and is acceptable in quality and form for

publication on microfilm and electronically:

_____

_____

_____

_____

_____

Chair

University of California San Diego

2021

iii

DEDICATION

This work is dedicated to the PhD student or aspiring PhD student (*anyone* really) who faces the overwhelmingly uncomfortable reality of how uncertain the future is. Take deep breaths. Be sure to find joy in the simplest of things. Be sure to tell yourself that you're not *scared* of the future, but *excited*. Many mountainous challenges lay ahead, but you have summitted many to get where you are today! There will be days where you don't want to get out of bed because nothing is working, and there will be days where everything is clicking, and you feel on top of the world. As long as you continue to persevere, no matter how uncertain the future may be, you will certainly succeed. Everything is going to be OK! Most importantly, don't even trip!!!

This work is also dedicated to those who have helped me get to where I am at today. The age-old proverb "It takes a village" really resonates with me, as there have been countless numbers of people who have assisted me along my journey. I would not be where I am at today if it weren't for the inspiration, guidance, companionship, and discussions with the many people I've crossed paths with over the years. Whether it be pre-grad school companions (Jeff Clark, Jared Cramer, David Ruiz, Paul Minnis, Dan Jones, Mike Hill, Caitlyn Comyns, Brian Myers, MFEBFFs, TBP crew) or some of the many people I've met during my masters and PhD (Benjamin Sommerkorn, Nicholas Derimow, Stephanie Pham, Max Mayther, Kyle Chan, Chad Warren, Andy Zhao, Meir Shachar, Wilson Wu, AMPers, Arash Yazdani, Audrey Hogan, Isaac Cabrera, Keisuke Matsushita, Juan Ybarra, Nada Qari) From me to you, the sincerest thanks! To Rebecca, thanks for being patient with me over the past few months. I am so glad to have met you! To my parents, thanks for providing me with endless support over the years. I appreciate you never giving up on me, despite my bumpy teenage years. To Daylee and Daniel, I look up to you more than you know. You all inspire and motivate me!

Finally, to those who have assumed the role of mentor, I would not have succeeded without your knowledge, motivation, experience, and inspiration. Dr. Victor Okhuysen from CPP, you helped build the foundation. Thank you for your time and energy. Dr. Javier Garay, Dr. Yasuhiro Kodera, and Dr. Harry Green, words cannot explain how much you have inspired and motivated me over the years. Thank you for believing in my abilities, and for providing this opportunity. I am forever grateful for everything that you have provided me.

TABLE OF CONTENTS

LIST OF FIGURES

LIST OF TABLES

ACKNOWLEDGEMENTS

I would like to acknowledge the rich and fruitful scientific discussions with the many members of AMPS lab (both past and present), in addition to those that have been had with members outside of AMPS lab. The many support staff that make UCSD laboratories run like a well oiled machine. Finally, the contributions from Dr. Javier Garay, Dr. Yasuhiro Kodera, and the late Dr. Harry Green, who have all been integral to the successes of these works.

Chapter 2 is co-authored with Professor Javier E. Garay and Dr. Yasuhiro Kodera, and is published in *Scripta Materialia* 169 (2019): 33-37. The dissertation author was the primary author on this paper.

Chapters 3 is co-authored with M.H. Shachar, Professor Javier E. Garay and Dr. Yasuhiro Kodera, and is currently in preparation for submission as a publication. The dissertation author was the primary author on this paper.

Chapter 4 is co-authored with Professor Javier E. Garay and Dr. Yasuhiro Kodera, and is currently in preparation for submission as a publication. The dissertation author was the primary author on this paper.

2014	Bachelor of Science, California State Polytechnic University, Pomona
2014-2016	Research Assistant, University of California Riverside
2016	Master of Science, University of California Riverside
2016-2021	Research Assistant, University of California San Diego
2016-2020	Teaching Assistant, University of California San Diego
2021	Doctor of Philosophy, University of California San Diego

PUBLICATIONS

Dewitt, D. M., Y. Kodera, and J. E. Garay. "High (10^{-3} s^{-1}) densification rates at< 0.25 homologous temperature in pressure assisted densification of nanocrystalline MgO: Effects of water absorption and grain size." *Scripta Materialia* 169 (2019): 33-37.

A. Yazdani, D. Dewitt, W. Huang, R. Borja-Urby, H. Luo (Karagozian & Case, Inc.), J.Magallanes (Karagozian & Case, Inc.), D. Kisailus, J. E. Garay, O. A. Graeve, "Effect of Crystallinity on The Mechanical Properties of an *in situ* Amorphous Steel Matrix Composite", *In preparation.*

D.M. Dewitt, M.H. Shachar, Y. Kodera, and J. E. Garay. "From Nanoporous to Transparent $MgAl_2O_4$ Spinel—Nanostructural Flexibility by Reaction Densification of Metastable Powders", *In preparation.*

D. M. Dewitt, Y. Kodera, and J. E. Garay. "Broadband Blue Emission in Transparent Polycrystalline Titanium Doped Spinel", *In preparation.*

ABSTRACT OF THE DISSERTATION

Nanoporous, Transparent, and Doped Magnesium Aluminate Spinel – Nanostructural Flexibility by Densification of Metastable Powders

by

Darren Michael Dewitt

Doctor of Philosophy in Materials Science and Engineering

University of California San Diego, 2021

Professor Javier E. Garay, Chair

Nanocrystalline oxides can have attractive properties such as high mechanical hardness, wear resistance, and high temperature plasticity. Fine (<500nm) grain and pore sizes are also beneficial for optical transparency and can help reduce dopant agglomeration beneficial for photoluminescence. However, most transparent polycrystalline oxides have large grains (>10µm) as a byproduct of their high-temperature fabrication conditions. Use of nanocrystalline powders as precursors and reactants seems an obvious choice for producing nanocrystalline oxides, but their use is complicated by high surface energies and reactivity with the environment. An improved understanding of the reaction and densification of nanocrystalline reactants is necessary to produce oxide ceramics of varying grain sizes, porosity ranges, and functionalities.

Here, the reaction and densification kinetics of three important oxide ceramics, MgO, Al_2O_3, and Magnesium Aluminate Spinel ($MgAl_2O_4$) are studied. Investigations lead to novel method to produce polycrystalline $MgAl_2O_4$ via widely available metastable and nanocrystalline reactants using current-activated, pressure-assisted densification (CAPAD). First, a comprehensive processing and densification study was performed, exploring the effects of nanocrystallinity and moisture adsorption on nanocrystalline MgO - which may be used as an analogue for alternative hygroscopic oxide systems and is an integral part of synthesizing $MgAl_2O_4$ by reaction densification. Second, the effects of metastability and nanocrystallinity (MgO and $\gamma-Al_2O_3$, <30nm) on $MgAl_2O_4$ phase formation, densification, and transparency of CAPAD densified reactant powder was considered. Finally, transition metal doping of $MgAl_2O_4$ from reactant powder is explored.

These results show metastable and nanocrystalline reactant powders combined with the flexibility of CAPAD allow for enhanced densification and reactivity. A wide array of microstructures, and new functionalities in polycrystalline $MgAl_2O_4$ are demonstrated. The metastable/nanocrystalline reactant powders facilitate comparably low temperatures for product formation and full density in $MgAl_2O_4$ – with up to 400°C reduction in the temperature for full phase formation and 300°C reduction for full density when compared to large-grained, stable reactant densification studies. The microstructural flexibility of this route is also highlighted with the production of both fully-dense transparent and robust nanoporous spinels, which conventionally arise from entirely different processing routes. Inclusion of transition metal dopants with reactant powders yields dense polycrystalline $MgAl_2O_4$, capable of tunability in the visible and previously unreported in published literature in polycrystalline form.

1. INTRODUCTION TO PROCESSING, DENSIFICATION, AND FUNCTIONALIZATION OF BULK OXIDE MATERIALS

1.1 Oxide Ceramic Materials – Introduction/Motivation

Oxide compounds are those which contain a metal or metalloid atom combined with oxygen, and are common in many applications. Several common oxide and mixed oxide ceramics frequently used in engineering applications include Al_2O_3, MgO, Y_2O_3, $Y_3Al_5O_{12}$, and $MgAl_2O_4$. These materials are often produced for extreme applications, where exposure to high temperatures, mechanical robustness, and mechanical properties are crucial. Prior use of these materials is vast, and includes use in refractories, laser host materials, porous materials, and thermal barriers.

Powder processing and consolidation (densification) methods for the production of these materials are often heavily researched as many different variables exist (processing conditions, temperatures, etc.), and manipulation of these variables typically effects the resultant microstructure and density of samples/parts – which are typically engineered for specific uses.

Microstructures with fine-grain sizes have many benefits relevant to engineering applications, including enhanced mechanical and optical properties. However, achieving these fine-grained microstructures in bulk ceramic oxides is often complicated, as high temperatures are often encountered in sintering procedures, which are known to facilitate large grain sizes. In addition, fine-grained microstructures generally require use of fine powders – which can be challenging to work with due to high surface energies and enhanced reactivity. It is crucial to investigate the consolidation of these fine-grained powders, as a better understanding could unlock further advances in the production of more robust ceramics that can assist with pushing the boundaries of modern engineering and science.

The subsequent chapters and sections of this dissertation include a brief introduction to some areas where fine-grained oxide ceramics are used, how they are processed, previous variables that have been explored, and various functionalities of these materials. Within this work, emphasis is placed upon grain size and adsorption effects, as several nanocrystalline oxide powders are known to be hygroscopic. In addition, an exploration will occur to elucidate the effects of nanocrystallinity and metastability on reactivity and densification. Analysis of highly dense, highly porous, and doped oxides will also be considered.

1.2 Transparent Ceramics

For much of the 20th century, the successful manufacturing of transparent polycrystalline ceramics was not a reality. The momentous R.L. Coble patent in the early 1960s regarding the production of highly dense, translucent polycrystalline alumina showed the potential to produce these materials and laid the foundation for future works [1]. Several decades later, the seminal work of Ikesue *et al.* [2] exhibited fully dense, highly transparent, polycrystalline yttrium aluminum garnet (YAG) via reaction densification in a vacuum furnace. The resulting materials had comparable thermal, and optical properties and superior mechanical properties to that of single-crystal counterpart, cementing the future potential of polycrystalline transparent ceramics.

There are several technological and economical motivations behind the desire to produce these ceramic materials. Most importantly, the fact that they perform *significantly* better than glass in many engineering applications where exposure to high temperatures and extreme conditions are common, requiring materials with superior mechanical properties and melting temperatures. Another driving force stems from the limited capabilities of single crystal production techniques,

which restrict part geometries, require temperatures that exceed melting and involve long durations – all of which could be overcome using novel processing and densification routes.

1.2.1 Microstructural Requirements for Transparency

The previously discussed landmark papers highlight the requirements for transparency in polycrystalline ceramics and provide guidelines for future work. When discussing the requirements for achieving transparency it is first important to distinguish between cubic optically isotropic ($n_1 = n_2$) and birefringent optically anisotropic ($n_1 \neq n_2$) materials, as these have different requirements for achieving transparency.

Figure 1.1 clarifies the effects of birefringence, porosity (density), and grain size on the propogation of light through both cubic (isotropic) and birefringent (anisotropic) polycrystalline optical materials. In both types of materials high density is crucial, as the interaction between light and large pores will lead to scattering caused by changes in index of refraction. If pore sizes remain very small (sub 100nm), the interaction between visible light and the pore is less significant and generally yields higher transparency. Figure 1.1c,d highlights the case of optically
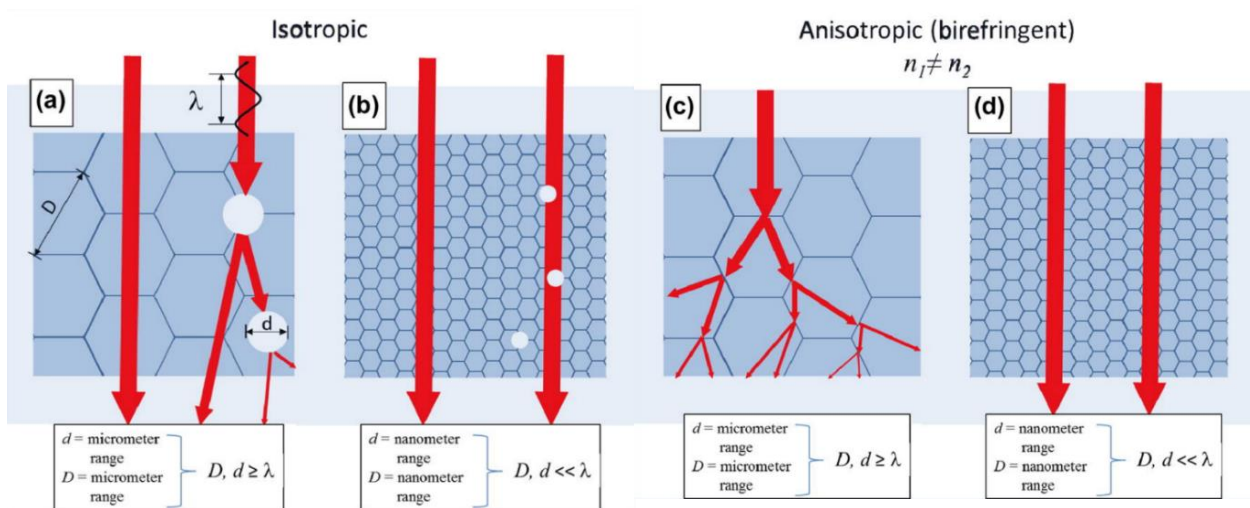
Figure 1.1 Schematic displays the interaction of light with cubic (isotropic, n1=n2 ; a,b) and birefringent (anisotropic, n1 ≠ n2 ; c,d) materials, highlighting the effects of pore size and grain size on scattering. Reproduced with permission from [3]

isotropic materials (ex: Al_2O_3), where grain size also plays an important role. As light propagates through randomly oriented large grains of birefringent materials it will experience a sudden change of index of refraction, which causes scattering and will result in a translucent or opaque sample (Figure 1.1c). This effect is negligible when the grain size is of comparable size to the incoming wavelength of light (Figure 1.1d). In the case of optically isotropic materials (AlON, YAG, $MgAl_2O_4$), there are no effects of grain size on scattering [3].

1.3 Porous Ceramics

Porous materials are of interest due to the capabilities of being used in chemical filtering and catalytic processes. Use of oxide materials for materials with high porosity are often considered due to many different attractive properties, including chemical stability, mechanical strength, wear resistance, and high melting temperatures. For example, natural zeolites (aluminosilicates) are often used as molecular sieves [4].

Spinels are a robust class of oxide materials that have been used in the creation of porous materials, with recent advances including include fabrication of hollow nanowires of zinc spinel [5], enhanced catalytic behavior in Cu-Al spinel [6], and successful fabrication of spinel nanocomposites [7].

The high melting point (2135C), low thermal conductivity, and chemical stability have led to the promotion of porous $MgAl_2O_4$ spinel for many different applications, however typical production methods including foam gel casting [8], [9] and templated growth [10] are complicated and typically yield pore sizes well into the micron range.

4

1.4 Densification Methods

There exists multiple routes that researchers have used for achieving oxides of varying density and grain size. Pressureless sintering is one of the earliest methods used, where very high temperatures and long hold times are typical to achieve full density. Consequently, this method is not suitable for producing highly transparent birefringent materials due to favorability of grain growth at these temperatures, which yields scattering. However, cubic isotropic materials have been successfully densified to high density/transparency using this method, as previously highlighted in the YAG work of Ikesue *et al*. [2].

The addition of pressure in the consolidation of powders has been shown to enhance densification by mechanisms such as particle sliding/rearrangement and plastic deformation, which are not apparent in pressureless sintering methods. Pressure also is known to affect the driving force for sintering, which occurs as a result of surface energy reduction [11]. These benefits are significant for acquiring full density and fine grains, which contribute to transparency in both cubic isotropic and birefringent anisotropic materials.

The advent of hot-pressing of ceramics powders was facilitated by this desire for microstructural improvement and control, where the addition of pressure facilitates lower densification temperatures and shorter durations than those encountered in pressureless sintering. For example, 99% relative density was achieved in pressureless sintered $MgAl_2O_4$ after >1 hour at 1900°C [12], while full density was achieved comparable powders hot-pressed at only 1450°C after 1 hour with minimal pressure (38.3 MPa) [13].

Although the benefits of pressure in hot-pressing are clear, the slow heating rates used (<

50 °C/min) present issues with achieving small grain sizes in bulk samples, as they permit longer

times exposed at temperatures favorable for grain growth. This has provoked researchers to utilize

current-activated, pressure-assisted densification (CAPAD, also known as spark plasma sintering,

or SPS) for the flexible consolidation of ceramics of varying grain sizes and densities. A schematic

for the CAPAD apparatus can be seen in Figure 1.2a.
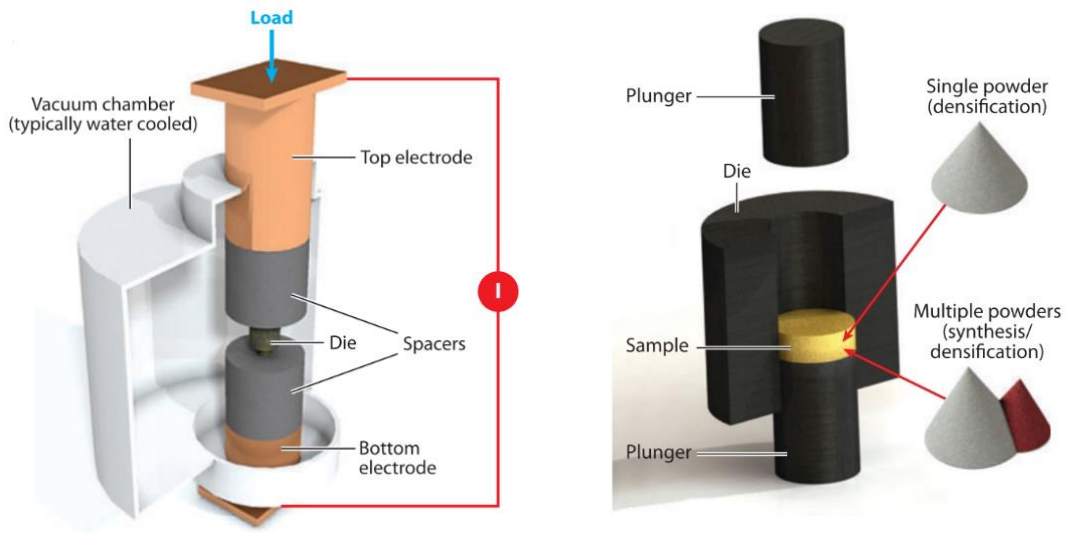
Figure 1.2 a) A schematic of the CAPAD apparatus. B) Powder containing die and plunger assembly. Reproduced with permission [11]

High heating-rates in CAPAD are facilitated by direct-current induced joule-heating

which flows through the die and plungers (Figure 1.2b) via the copper electrodes, which

simultaneously apply pressure to the powders. If beginning with nanometric powders, the high

heating-rates (50-600 °C/min) and applied pressure in CAPAD assist with retention of these small

grain sizes through reduction in hold temperature and decreased durations at hold temperatures.

High heating rates facilitate the drastic reduction in time powders are exposed to temperatures

where coarsening (necking) takes place, resulting in more densification via grain boundary and

volume diffusion [11]. Mechanisms for enhanced densification via pressure application have been discussed previously.

Other methods and routes for the consolidation of transparent polycrystalline ceramics also exist, including hot-isostatic pressing (HIP) and combinations of previous routes. These will not be thoroughly discussed in this introduction as these methods generally utilize higher pressures, temperatures, and complex processing routes. These conditions have been shown to be favorable for high transparency, but generally result in significant grain growth [14].

A detailed comparison grain sizes and densities of additive-free MgO retrieved from literature can be found in Figure 1.3-1.5, where the benefits of pressure-based densification methods can be clarified. A clear difference in the temperatures required to achieved full-density can be seen, where full density is achieved at much higher temperatures in pressureless sintering when compared to pressure-based consolidation techniques (1300 °C vs. <1000 °C, respectively). In addition, the fine grain sizes produced by these pressure-based techniques relative to pressureless sintering can be clarified. Lastly, the benefits of CAPAD can be seen by the highest densities and smallest grain sizes when compared to the other previously discussed methods for powder consolidation.
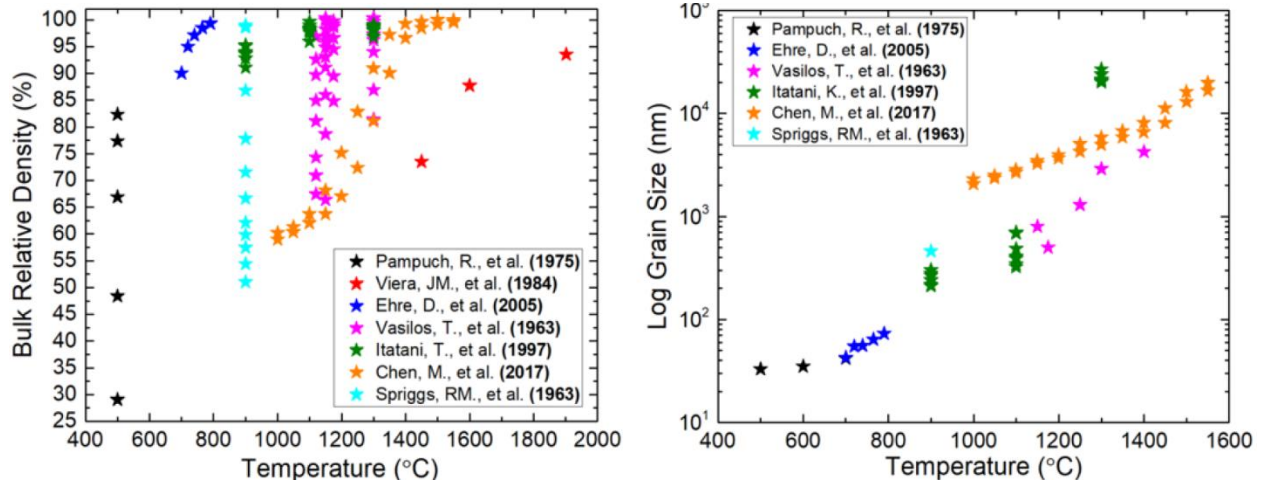
Figure 1.3 Grain size/relative density VS. temperature for pressureless sintered, additive-free magnesia
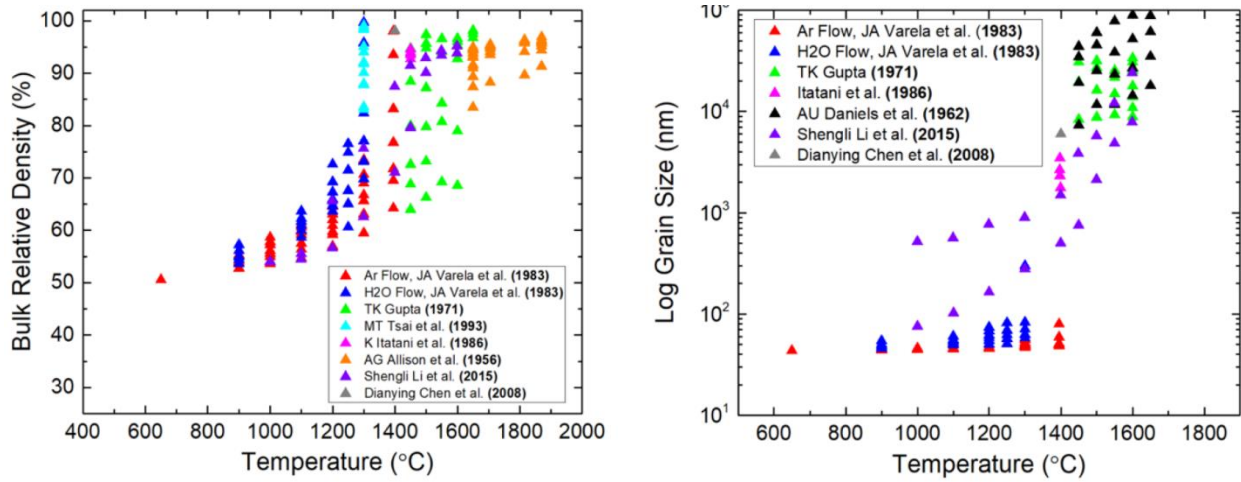
Figure 1.4 Grain size/relative density VS. temperature for hot-pressed, additive-free magnesia
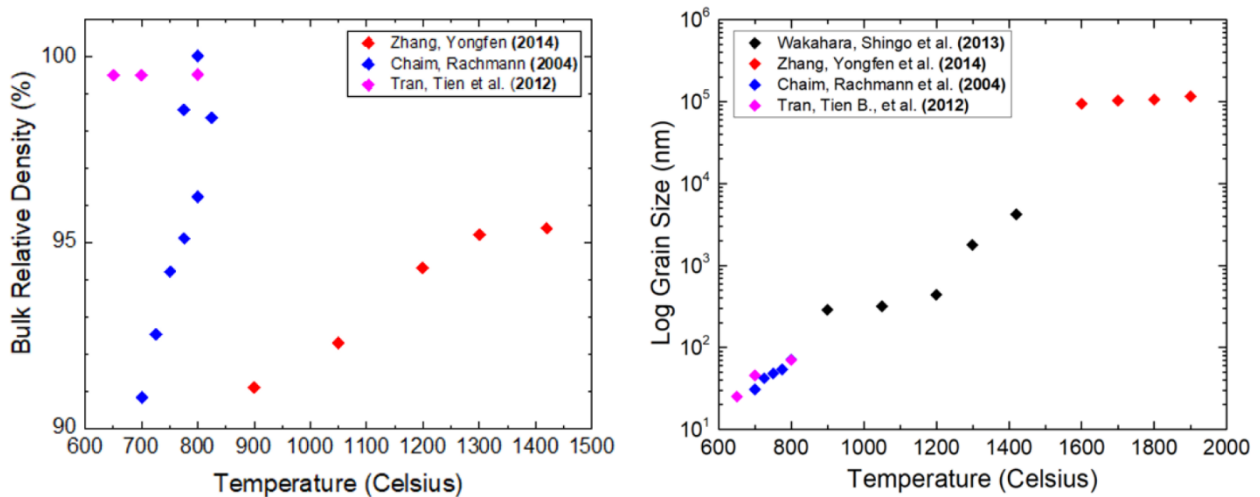
Figure 1.5 Grain size/relative density VS. temperature for CAPAD densified, additive-free magnesia

1.5 Densification of Magnesium Oxide

1.5.1 Background

MgO is a useful engineering ceramic that has high temperature structural applications as well as interesting optical applications[15]–[18] Consequently, the fabrication of MgO has been extensively studied by pressureless sintering, hot-pressing, and CAPAD. Due to of MgO's high temperature resistance, pressure-less sintering typically requires high temperatures (>1300°C) and long durations (>1 hr.) for full density, leading to substantial grain growth [>1μm]. For example, S. Li *et al*. fabricated near fully dense (98% RD) magnesia using a two-step free-sintering procedure. Despite the reduced grain sizes encountered using this innovative procedure, temperatures and durations exceeded 1400°C and 20 hours to achieve near full density, with grain sizes exceeding 20 μm [19].

As mentioned previously, the application of pressure in powder densification has drastically reduced the temperatures required acquiring full density in bulk ceramics by inducing particle rearrangement, plastic deformation mechanisms, and enhancing the driving force for sintering [11]. Using the HP technique D. Ehre *et al*. densified 10nm MgO at 790°C for 4 hours, resulting in a sample with (RD) of >99% and a grain size < 100nm. To better understand the effects of pressure, experiments were performed from 100 to 200 MPa at a constant temperature and hold duration, showing increasing densities and decreased grain sizes with added pressure [20].

Although the application of pressure in HP generally yields higher densities, the slower heating rates and long hold durations encountered with use of the HP technique allow for prolonged exposure to higher temperatures. The rapid heating rates facilitated by joule heating and application of pressure in CAPAD result in fast processing kinetics and have yielded the potential for even finer microstructures and metastable phases. For example, T. B. Tran *et al.* achieved full

density in 10 nm MgO and Ca-Doped MgO at temperatures ranging from 650-800°C using high pressure (>300 MPa) and low holding times (5-30min), resulting in samples with high transparency and grain sizes from ~25-70 nm. [16].

1.5.2 Effects of Grain Size on Densification of MgO

Use of a smaller starting grain size in powder consolidation allows for a considerably larger grain boundary area, favorable for enhanced densification due to shorter diffusion distances and enhanced grain boundary diffusion. Despite the wide spectrum of available MgO grain sizes that are commercially accessible and the known benefits of nanocrystallinity on densification, systematic CAPAD experiments investigating the effects of grain size are lacking. Considering alternative consolidation methods, comprehensive studies of grain size effects are still few.

Grain size effects on the densification of CeO_2 by pressureless sintering were studied by Y.C. Zhou and M.N. Rahaman, where 10 nm, 100 nm, and 500 nm after pressing to 50 MPa. Upon heating at 5 °C/min in oxygen and measuring contraction via dilatometry, it was found that the magnitude of densification at a particular temperature was strongly dependent on temperature, with the smaller grained powders concluding densification at hundreds of °C less than the 1000 µm powder (Figure 1.6) [21]
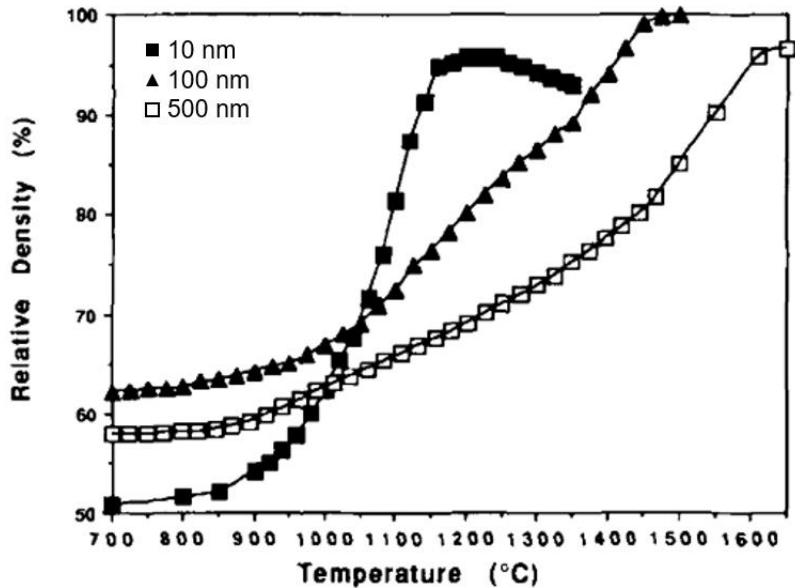
Figure 1.6 Relative density vs. temperature for CeO_2 powder of varying zise, free-sintered using heating rate of 5°C/min. Reproduced with permission [21]

The effects of starting particle size of the consolidation MgO via hot-pressing was studied by Itatani *et al.,* where 7 different sized powders were heated to temperatures from 900 to 1300 °C under 30 MPa. Shrinkage rate vs. temperature for a constant heating rate (10 °C/min) showed lower temperature densification mechanisms active in smaller grained powders, increasing in magnitude with decreasing grain size. Isothermal holds (5 °C /min) at varying temperatures and durations yielded higher densities for all powder sizes relative to 250 nm powder, showing highest densities achieved using 44nm powder [22].

Based off previously discussed examples, it even more clear that the effect of grain size on densification is considerable. However, it is important to consider grain coarsening during heating when highlighting these works, as the production methods (free sintering, hot pressing) used more than likely cause considerable grain growth during densification due to exceptionally low heating rates (5-10 °C/min). The higher heating rates typical of powder consolidation in CAPAD could potentially elucidate the effects of starting particle size, but this processing method has yet to be

utilized for this type of study. Work has been done by Reis and Chaim [23] on densification maps

for CAPAD of MgO using a previously developed HIP model [24], considering the effects of

coarsening and grain growth on consolidation. The effects of particle size on relative density at a

fixed temperature and pressure for a variety of hold times were shown and can be seen in Figure

1.7. This figure further demonstrates the drastic effects that particle size has on densification.

However, but experimental verification is lacking.
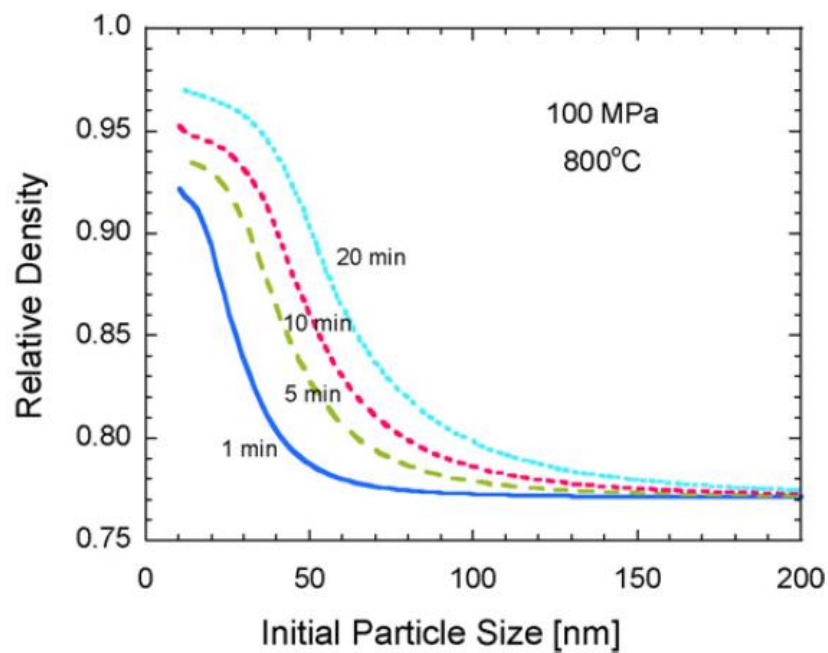
Figure 1.7 Relative density vs. initial particle size for varying hold durations at 800°C, 100 MPa. Derived from HIP model [24], with grain coarsening considered. Reproduced with permissions from [23]

1.5.3 Effects of Humidity on Densification of MgO

It is well-known that MgO powder is hygroscopic – highlighted by Figure 1.8 below, showing fully dried MgO nanopowder of varying sizes exposed to air for extended durations. This effect is magnified with very fine powders (high surface area), exemplified by nearly 15% of the total mass 20nm powder corresponding to adsorbed moisture after 3 hours. This percent decreases as the particle size increases, where the 29 and 42 nm MgO powders have adsorbed nearly 12 and 5% of their total weight, respectively.
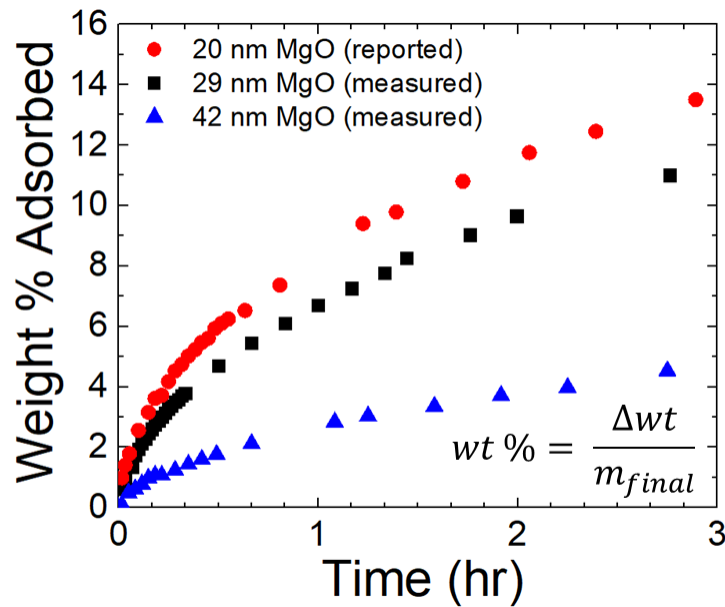
Figure 1.8 Weight % adsorbed V. Time for magnesia nanopowders of varying sizes.

Accordingly, researchers have realized that the presence of water/humidity can significantly affect the sintering of MgO[25]–[27]. Anderson and Morgan found that water vapor enhances agglomeration and increases sintering and crystal growth rates—effects attributed to enhanced by adsorbed H_2O. Large crystallite sizes were achieved in 3 minutes under humidified atmosphere, while it took 125 hours in vacuum conditions to achieve crystals of a comparable size at similar temperatures [25]. Varela and Whittmore concluded that surface diffusion and particle

rearrangement were enhanced during the free-sintering of magnesia in moistened argon, yielding drastic differences in bulk properties of samples produced by the two different methods. Experiments performed at 1300 °C for 4 hours in humidified argon resulted in samples with 95% and 300nm of grain size, while experiments in dry argon produced samples with relative densities of 70% with 52nm grain sizes [26].

Recently there has been interest in application of water and other liquid phases to dramatically reduce the consolidation temperatures in a process called cold sintering[28]. Luo and co-workers also demonstrated impressively low temperatures and short times required to densify ZnO using currents (flash sintering) and ZnO powders that had been exposed to water vapor[29]

1.5.4 Clarification of Densification Mechanisms

Analysis of densification kinetics can clarify the effects that specific variables (i.e. grain size, humidity) have on the consolidation of ceramic powders and assist with elucidation of mechanisms. Well known HP experiments and models show that using nanocrystalline (nc) powders and application of pressure can dramatically increase densification rates. The effect of pressure, σ and grain size, d on diffusion-controlled densification rates, $\dot{\rho}$ can be described using relations of the form[30], [31]:

$$\dot{\rho} = C \left[\frac{D_i}{kT}\right] [f(\rho)] \left[\frac{1}{d^m}\right] \sigma^n \tag{1}$$

where C encompasses material dependent constants, D_i is the controlling diffusion coefficient, $f(\rho)$ is a function of the instantaneous density, m is an exponent usually between 1-3 and n is the stress exponent usually between 1-3.

Zhou and Rahaman utilized densification rates to clarify the effects of grain size on densification of CeO_2, free sintered to temperature at 5 °C/min. Figure 1.9 shows the densification rates of 10 nm, 100 nm, and 500 nm powders. The rate of densification increases significantly with smaller particle size, highlighted by the near 5×10^{-3} min^{-1} increase in densification rate that occurs with a decrease in particle size from 500 nm to 10nm. The temperature at which the maximum densification rate occurs also is strongly dependent on particle size, where the 10 nm powder yields a max that is approximately 500 °C lower than the curve representing 500 nm powder [21], [32]. This increase in rate/decrease in temperature where maximum rate occurs is likely caused by the enhanced surface area encountered with smaller particle size, which vastly increases the contribution that grain boundary diffusion has on densification [33].
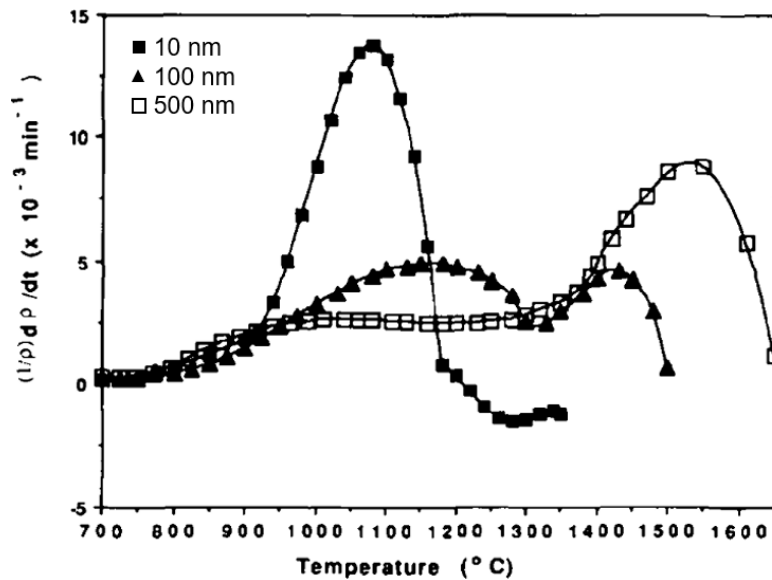
Figure 1.9 Densification rate vs. temperature for CeO_2 with varying starting particle size. Reproduced with permission from [21], [32]

To investigate the differences in transparency resulting from the use of different heating rates during the densification of polycrystalline $MgAl_2O_4$ made by CAPAD, Morita *et al.* utilized densification rates. It was found that the magnitude of the densification rate increased and shifted

to higher temperatures with increasing heating rate. By correlating the densification kinetics with microstructural observations, it was determined that slow heating rates were favorable for pore shrinkage, as higher temperature diffusion mechanisms were active for longer durations. High heating rates enhanced grain boundary sliding (increased densification rates), but decreased the amount of time spent at temperatures suitable for pore shrinkage [34].

Alaniz et al. utilized densification rates better to understand the role of pressure on the densification kinetics of metallic, ionic, and covalent powders. Aluminum, silicon, and fully stabilized zirconia nanopowders were subjected to a variety of pressures in CAPAD. It was found that increasing pressure has a drastic effect on the maximum densification rate, changing by 60% when increasing the pressure from 35 to 106 MPa in fully-stabilized zirconia, 80% and 120% in aluminum and silicon (respectively) when increasing the pressure from 71 to 106 MPa. The increase in magnitude of the maximum densification rate with increasing pressure was thought to be an effect of increased diffusional driving forces. It was also found that the temperature where the maximum densification rate occurs did not vary, indicating no change in mechanism [35].

The real-time output of multiple variables from CAPAD allows for the simple analysis of densification rates. The effects of particular r variables in pressure assisted densification techniques are not very well studied, and the previously mentioned texts offer some clarification on the particular roles of these variables. Despite the known benefits of nanocrystallinity on densification and the lack of knowledge regarding what role adsorption has on the densification in pressure-assisted methods, there has been little work on the role of grain size or water absorption in *in-situ* measured densification rates. Future chapters will explore the effect of grain size and water adsorption on the densification and densification kinetics of nc-MgO densified using

CAPAD, in addition to utilizing other characterization methods in conjunction with densification rates to understand the dominant mechanisms during consolidation.

1.6 Processing and Densification of Magnesium Aluminate Spinel

1.6.1 Background

Polycrystalline $MgAl_2O_4$ spinel has been shown to exhibit robustness in many engineering applications due to its high melting temperature, attractive mechanical properties, chemical stability, and transparency at many wavelengths. The initial patent involving the processing of transparent polycrystalline spinel by Bruch in 1970 [36] paved the way for many researchers and led to dozens of publications and several reviews[37]–[41] . Since then, many different processing routes and consolidation techniques have been explored - many with the final goal of achieving full density (transparency) and decreasing grain size (enhanced mechanical properties).

The fast-processing kinetics and applied pressure of Current-Activated, Pressure-Assisted Densification (CAPAD) have yielded many materials with high densities and fine grain sizes[11], provoking many researchers to utilize CAPAD for achieving bulk spinel. Morita *et al.* was able to achieve transparency and high bending strength from additive-free, pure-phase $MgAl_2O_4$ powders using low heating rates (<10°C/min)[34], [42]. In an attempt to reduce durations at high temperatures, Wang and Zhao succeeded in achieving transparency in additive-free spinel using a fast heating rate (100°C/min) and a two-step load procedure [43]. High-pressure (300-400MPa) CAPAD experiments of additive-free spinel by Sokol *et al.* yielded samples with superior transmission, smallest grain size, and excellent mechanical properties when compared to other literature of transparent spinel produced from additive-free powders by CAPAD[44].

1.6.2 Use of Additives to Enhance Densification

The push to achieve higher densities has led some researchers to examine the effects of additives on the transparency of CAPAD produced spinel[45]–[48], arguably the most common being LiF. As an additive to $MgAl_2O_4$, LiF has been proposed to remove impurities from particle surfaces which enhances diffusion in addition to enhancing particle rearrangement during compaction, both of which may yield higher densities.

Despite these benefits, use of LiF to aid densification has been shown to promote significant grain growth during densification, which could have negative effects on bulk mechanical properties. Frage *et al.* showed enhanced transparency and significantly larger grain size when doping spinel powders with 1 wt% LiF, but failed to see significant differences in mechanical properties when compared to the undoped samples produced under comparable conditions[45]. However, a more thorough work showed higher hardness (+150HV) and bending strength (100% increase) in LiF-free nanocrystalline spinel, despite having inferior transmission when compared to 40µm bulk spinel with 1 wt% LiF added[46]. LiF has also been shown to degrade transparency by reaction with aluminium in the $MgAl_2O_4$ matrix, potentially forming precipitates $LiAlO_2$ with insufficient mixing prior to consolidation [49]

1.6.3 Processing and Densification of Spinel from Reactants

Challenges existing with commercial availability of $MgAl_2O_4$ spinel powder have led some

to take advantage of the reaction between MgO-Al_2O_3, both of which are available in a variety of

different particle sizes and purities. The MgO-Al_2O_3 phase diagram can be seen in Figure 1.10

below [50], where the formation of spinel occurs at elevated temperatures upon combining the

reactants 1 to 1 by mol.
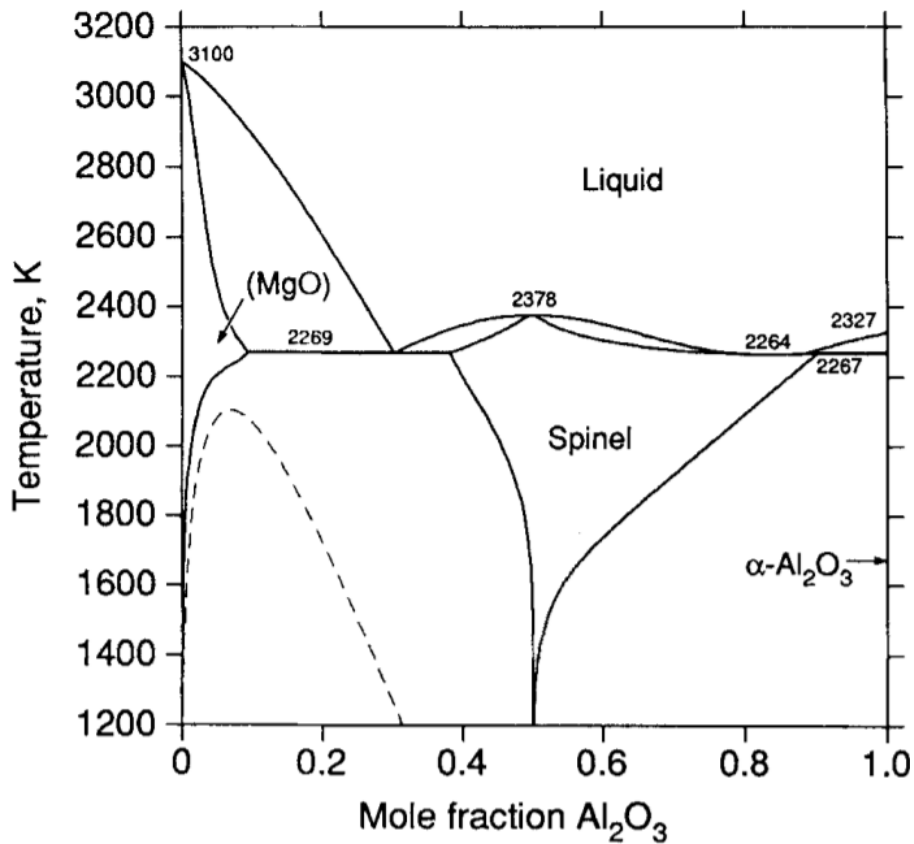
Figure 1.10 MgO – Al2O3 phase diagram from [50]. Reproduced with permission.

However, potential issues with the densification of spinel from reactants could arise from

incomplete reaction, which could yield scattering in bulk samples due to mismatched indices of

refraction. This led some of the earlier pioneers to employ very high temperatures and additives to

achieve transparency using free sintering methods. In the work of A. Gatti [12], very high

temperatures (1900C), complex firing schedules at long durations, and additives were used to achieve densities above 99%.

Works on reaction densification of bulk transparent spinel utilizing more novel methods (HP, CAPAD) are lacking. The use of reactants for spinel formation typically involves pre-reaction *prior* to densification. Alhaji and co-workers used reactants to synthesize sub-micron spinel powders, showing enhanced reactivity of the powders in the presence of LiF additive prior to densification, and enhanced transparency in the CAPAD samples densified from these powders[51].

Meir *et al.* utilized CAPAD to achieve transparency in reaction densified spinel, showing similar benefits of LiF as previously mentioned works. Use of additives in the reaction densification of ~200nm Al_2O_3 and >10μm agglomerated MgO yielded enhanced reactivity, density, and transparency at significantly lower temperatures when compared to densification of reactants lacking LiF. However, as seen in many of the previous studies involving LiF as an additive, grain sizes of bulk samples were well within the micron range [52].

The notable work from A. Krell to produce highly transparent, fine grained spinel from reactants is one of the only few works involving *additive-free* reaction densification. Powders with particle sizes of 150nm and 2-3μm (Al_2O_3 and MgO, respectively) were first slip-cast into specific molds, annealed to 800°C to burn off any organics, heated at 2 °C /min until ~96% RD, followed by HIP at 200 MPa. Upon HIP for an undisclosed duration at 1540°C, a highly transparent (80% in-line transmission @ 640nm) spinel with grain sizes ranging from 3-5 μm was produced (Figure 1.11) [14].
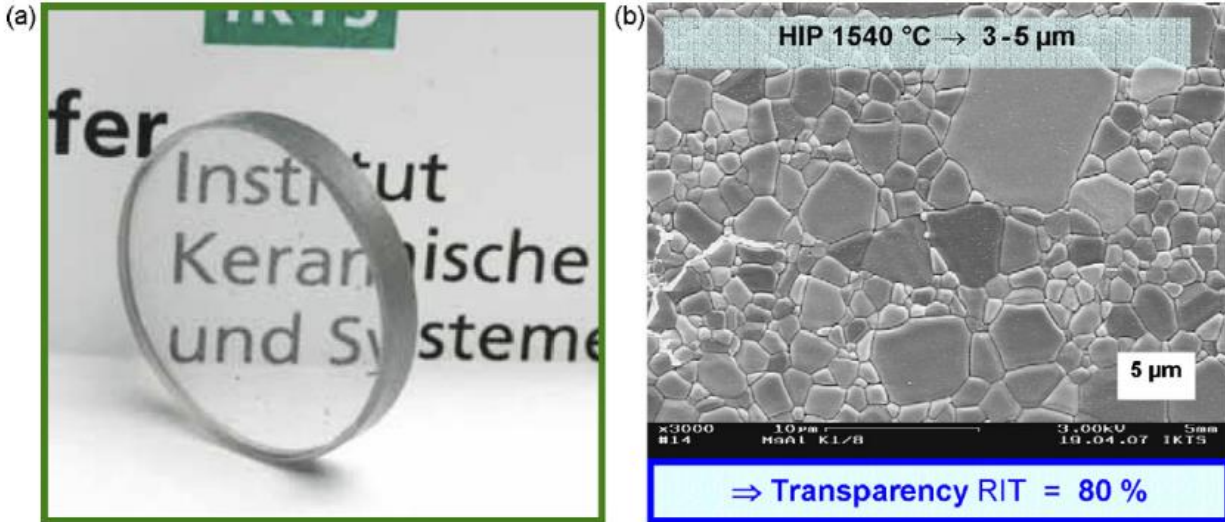
Figure 1.11 Transparent spinel sample acquired from HIP of reactants (1.11a), and corresponding microstructure (1.11b). [14]. Reproduced with permission.

Despite the significant benefits LiF has on the densification, transparency, and reactivity of spinel from reactants, rapid grain growth occurs in its presence. Additive-free methods that have been explored involve complicated procedures and extended durations at high temperatures, also resulting in runaway grain growth. Both of these techniques to achieve high densities and the resulting large grain sizes can be detrimental to uses involving high mechanical strength. The availability of *very* fine-grained nanocrystalline reactants and the enhanced densification that occurs as a result of nanocrystallinity[53], provides a necessity for further exploration. Future chapters will explore the processing and densification of sub 50 nm reactants in CAPAD for fine-grained transparent spinel.

1.6.4 Reaction Kinetics of MgAl$_2$O$_4$ from MgO-Al$_2$O$_3$ reactants

When considering the densification of MgAl$_2$O$_4$ from reactants, it is important to analyze the kinetics of reaction. Numerous reaction kinetics studies have occurred, including classic single-crystal diffusion couple experiments [54] and polycrystalline diffusion couple experiments at both atmospheric [55] and at elevated pressures [56]. These studies all indicate a parabolic time dependence of spinel growth between MgO and Al$_2$O$_3$ interfaces, indicating diffusion-controlled growth. Reaction rate constant (m^2/s) for diffusion-controlled growth, k, can be represented by equation 2 below:

$$k = \frac{(\Delta X)^2}{2t} \tag{2}$$

Rearranged, we see the parabolic time dependence between thickness (ΔX) and time (t) in equation 3:

$$\Delta X = \sqrt{2kt} \tag{3}$$

Derivation of activation energies for spinel formation can be acquired by plotting experimental values for k at specific temperatures, in the form of ln(k) vs. 1/T by using the classic Arrhenius equation:

$$k = A exp^{\left(\frac{-Q}{RT}\right)} \tag{4}$$

Where A is the pre-exponential factor (m^2/s), and the slope of the ln(k) vs. 1/T plot represents a ratio of the activation energy (Q_a, J/mol) and the ideal gas constant (R, J/mol*K).

Despite kinetics experiments occurring with both single crystals and polycrystals, they yield comparable activation energies at ambient pressure conditions, ranging from ~520 kJ/mol (1560-1750°C, [54]) to ~540kJ/mol (1200-1600°C, [55]). At higher temperatures (1750-1900°C), the activation energy was reported as 370 kJ/mol, likely occurring due to a change in diffusion mechanism [54]. At higher pressures (1-4 GPa,), Watson and Price experimentally derived an activation energy of 473 kJ/mol irrespective of pressure, with the reaction rate constant (k) decreasing with increasing pressure [56]. Although agreements exist amongst reported activation energies for spinel formation, differences exist with describing the actual mechanism, with suggested controlling mechanisms varying from grain-boundary diffusion [57] to cation interdiffusion [55].

Reaction kinetics experiments using powders is minimal, as the literature on densification of $MgAl_2O_4$ mostly consists of densification of single-phase powder. However, Sinhamahapatra used dilatometry and XRD to determine kinetics constants in MgO rich $MgAl_2O_4$ from large-grained (>6 µm) powders and validate a proposed kinetic model, acquiring an activation energy of 409 kJ/mol [58].

Although many works have been done studying the reaction between the MgO-Al_2O_3 system, a lot of work remains. All works utilize α-Al_2O_3 in conjunction with MgO, with most being classical coupling experiments involving either single crystals or dense polycrystals. In works involving powder experiments, the role of alternative Al_2O_3 phases is unknown and comprehensive studies involving nanocrystallinity are lacking.

1.7 Titanium-doped polycrystalline $MgAl_2O_4$

1.7.1 Background

There are many benefits to using polycrystalline laser hosts over doped single crystals, including the many previously discussed technological and economic benefits of using transparent polycrystalline ceramics *in lieu* of single crystals (see *section 1.1.1. –* part geometry, production challenges). Most importantly, polycrystalline production techniques allow for the potential for high dopant concentrations and homogeneous dopant distributions, whereas doping of single crystals presents challenges with dopant solubility and gradients. In addition, polycrystalline materials have far superior mechanical properties when compared to their single crystal counterparts, which could be beneficial for the use of polycrystalline laser hosts in demanding engineering applications. The capabilities of transparent polycrystalline ceramics as viable laser hosts was realized shortly after the seminal Ikesue *et al.* [2] paper demonstrating polycrystalline YAG with optical and mechanical properties comparable to that of a single crystal. In a later publication, Ikesue *et al.* also showed Nd-doped polycrystalline YAG with properties equivalent or superior to those of a single crystal with similar doping concentration [59]. Since then, there have been many works involving many different dopants, host materials, and processing methods, with varying levels of success.

The use of CAPAD as a method for the production of doped polycrystalline ceramics also has many benefits. As previously discussed, the rapid processing kinetics facilitated by high heating rates and applied pressure allow for enhanced transparency by retaining small grain and pore sizes. When doping polycrystalline materials, the high heating rates and applied pressure allow for non-equilibrium processing, resulting in the capabilities to dope with out of equilibrium dopant concentrations. For example, CAPAD densified transparent 0.5 at% $Tb:Al_2O_3$ yielded high

transparency (~75% @ 800nm), long lifetimes, and characteristic Tb^{3+} emission in a sample doped well over the equilibrium solubility limit (~10^{-3} %) [60].

Of the many successfully doped polycrystalline laser host materials, $MgAl_2O_4$ is a potentially robust alternative due to its high melting temperature, robust mechanical properties cubic crystal structure (no birefringent scattering), and previous success with achieving high transparency. These features have provoked the successful CAPAD densification and characterization of rare earth doped (Ce^{3+} [61], [62], Tb^{3+} [61], [63], Dy^{3+} [63], Eu^{3+} [62], Y^{3+}, Gd^{3+}, La^{3+} [64], and Nd^{3+} [65]) and transition metal doped (Co^{2+} [66], [67]) polycrystalline spinel.

1.7.2 Ti-Doped MgAl₂O₄

Titanium-doped Al_2O_3 is arguably one of the most commercially successful laser materials, outside of the most commercially successful Nd:YAG laser crystal. The excellent mechanical and thermal properties of Al_2O_3 as a host are desired in laser applications. In addition, doping Ti^{3+} into Al_2O_3 single crystals yields a laser crystal with one of the widest tunable emission bands (~600-1200nm), which also provides capabilities for producing very short pulse widths. The characteristic absorption and wide emission bands of $Ti:Al_2O_3$ can be seen in Figure 1.12.

The success of $Ti:Al_2O_3$ and the novel dopant characteristics of Ti^{3+} have provoked some researchers to utilize alternative host materials, as this can potentially allow for tunability at
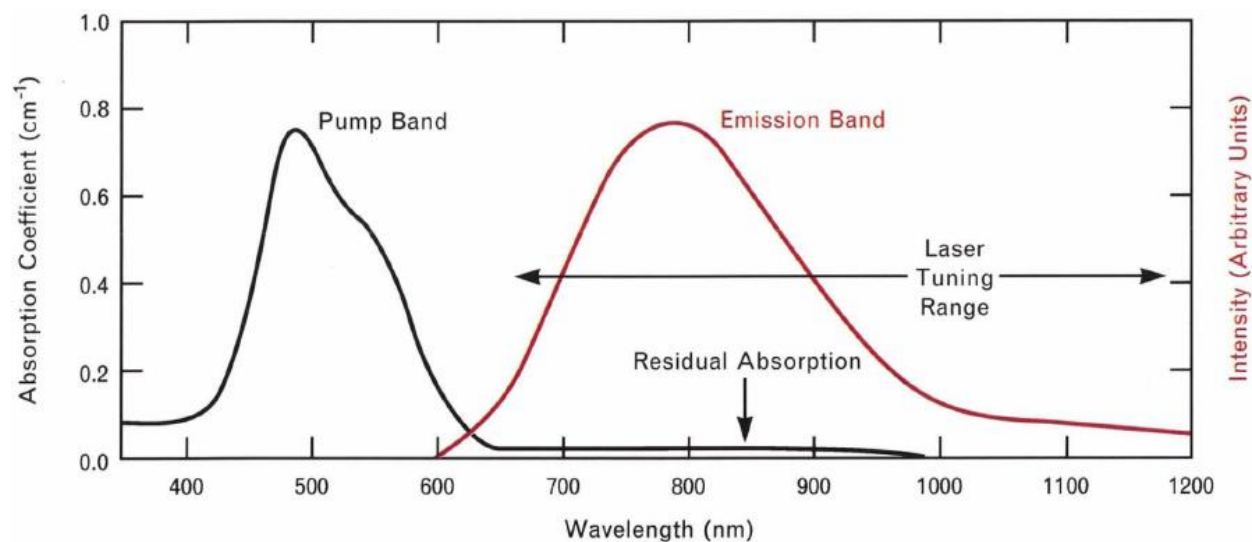
Figure 1.12 Absorption Coefficient/Emission intensity vs. wavelength for single crystal Ti-doped Al_2O_3 / Retreived from [106] with permission.

different emission ranges and alternative pumping schemes. The short radiative lifetime of Ti:Al_2O_3 (3.85 μs) prohibits the use of flashlamp pumping as short pulses limit their lifetimes due to high peak currents, also providing motivation for exploration of different host materials.

1.7.2.1 Ti^{3+}/Ti^{4+} Absorption

Doping of single crystal $MgAl_2O_4$ has been explored by numerous researchers, and multiple single crystal production methods have been utilized with varying levels of success [68]–[72]. By use of different atmospheres (air, reducing) during production and annealing of doped single crystals, absorption and emission information corresponding to electronic transitions of specific titanium valence states has been clarified.

Bausa *et al.* was the first to successfully dope single crystal $MgAl_2O_4$ with 0.05at% Ti by the Verneuil technique. Transmission measurements of the Ti-doped crystal showed an absorption edge starting at approximately 300nm (~4.8 eV) and peaking at 230nm, far from the band gap

energy of 9 eV. The absorption edge red shifts upon doping and is thought to be provoked by the charge transfer bands of the Ti^{3+} and Ti^{4+} ions. Two more absorption bands occur at approximately 490nm and 790nm, corresponding to the $T_{2g} \rightarrow E_g$ electron transition of the Ti^{3+} ion (octahedral site) and the $Fe^{2+} + Ti^{4+} \rightarrow Fe^{3+} + Ti^{3+}$ charge transfer transition, respectively[68]. The large absorption band at 790nm is attributed to iron contamination and has been further clarified by intentionally co-doping with Fe^{3+} by Jouni and coworkers [71]. Similar absorption schemes were reported Jouni *et al.,* who swept Ti-dopant concentrations in single crystal $MgAl_2O_4$ grown using the micro-pull down method under argon environment [71], [72]. Slight differences in absorption locations in this work were attributed to argon growth environments. The absorption data from these works and corresponding electronic transition information can be elaborated upon in Figure 1.13, The effects of varying Ti-dopant concentration on absorption can be seen in Figure 1.14a.

In order to better understand the absorption bands of the two cation valence states, alternative production parameters and processing techniques were employed. First, Ti-doped $MgAl_2O_4$ single
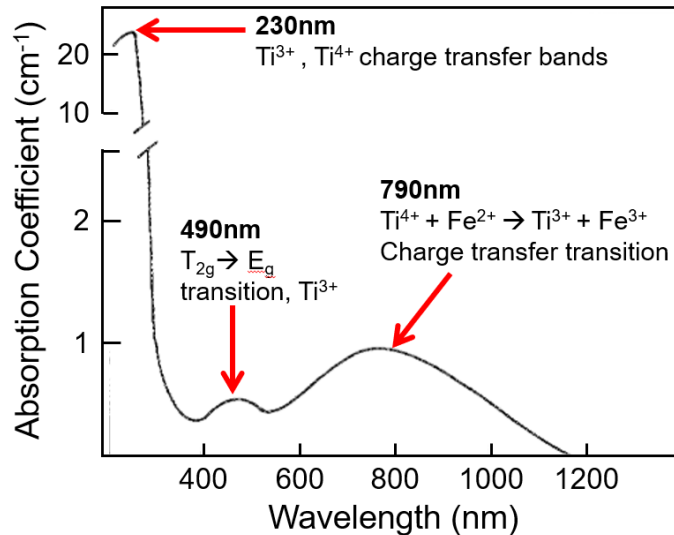
Figure 1.13 Absorption for 0.05at% Ti-doped $MgAl_2O_4$ single crystals grown by Verneuil technique, showing the peak location and corresponding electronic transition responsible for absorption. Modified from[68] Reproduced with permission from AIP publishing.

crystals were grown under an oxidizing environment via the floating-zone method [69], [70]. Due to the oxidizing environment, it was assumed that the titanium ions converted to the Ti^{4+} state, evidenced by no signal being detected from the absorption corresponding to Ti^{3+} valence state (~490nm) and no absorption related to the charge transfer transition of $Ti^{4+} + Fe^{2+} \rightarrow Ti^{3+} + Fe^{3+}$ (~790nm).

Isolation of the two valence states was also achieved by exposure of grown crystals to high temperatures for extended periods, as shown in the annealing of Ti-doped crystals grown in minimal oxygen environments , where characteristic Ti^{3+} absorption initially occurred. Upon annealing these crystals for 2 hours at 1100C in a reducing environment, Bausa *et al.* showed an increase in the absorption edge (~230nm), a decrease in the 790nm absorption band, while the 490nm signal attributed to the Ti^{3+} cation remained unaffected. The simultaneous growth of the absorption edge and decrease of the 790nm absorption band is attributed to the redistribution of the Ti^{4+} cations [68]. Oxygen annealing of Ti-doped $MgAl_2O_4$ single crystals grown under argon environment (initially showing characteristic Ti^{3+} absorption) was performed by Jouni *et al.*, resulting in similar absorption results to that of Ti-doped crystals grown under oxidizing environment [71]. Oxygen annealing of these crystals at 1400C for 30 hours resulted in the increase of the magnitude of the absorption edge, and the loss of the absorption bands corresponding to Ti^{3+} cation (495nm) and the absorption related to the charge transfer transition of $Ti^{4+} + Fe^{2+} \rightarrow Ti^{3+} + Fe^{3+}$ (~780nm). The disappearance of these absorption peaks is attributed to the oxidation of the Ti^{3+} cation (absence of 495nm) and cation redistribution (780nm, previously discussed). A comparison of doped Ti-$MgAl_2O_4$ crystals as-grown under argon environment and after annealing in oxygen can be seen in figure 1.14.
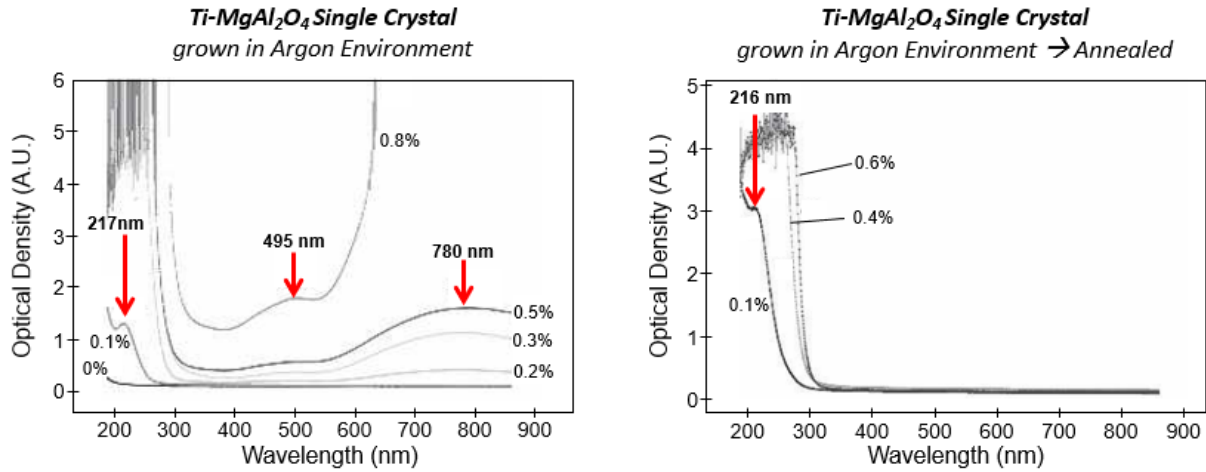
Figure 1.14 Absorption bands of Ti-doped $MgAl_2O_4$ single crystals made from micro-pulldown technique with varying Ti concentrations, considering two different scenarios. 14a shows the absorption bands of the as grown crystal in an oxygen free environment. 14b is the resulting absorption data of these as grown crystals annealed in oxygen, showing the absence of absorption bands at 495nm and 780nm. Results in 14b are similar to as grown crystals in oxygen environment. Figures modified from [71]. Reproduced with permission.

1.7.2.2 Ti^{3+}/Ti^{4+} Emission

Emission of Ti-doped $MgAl_2O_4$ single crystals has been shown to occur by pumping within the absorption edge (250-290nm) and by pumping the absorption band at 490 nm. Pumping within the absorption edge regime has produced broadband blue (FWHM ~ 100nm) emission centered in the visible range from 455nm – 500nm depending on the excitation wavelength, and has been reported by all groups [68]–[71] irrespective of production technique. This broadband emission seen with excitation of the absorption edge is attributed to the Ti^{4+} cation instead of the Ti^{3+} cation. First, it appears when pumping the absorption edge for crystals grown in both oxidizing and reducing environments. Second, the absorption edge becomes more prominent after annealing grown Ti-doped (Ti^{3+} rich) in both reducing [68] and oxidizing [71] environments, where cation redistribution and Ti^{3+} oxidation occurs. Lastly, it is thought that the blue emission is a result of

the Ti^{4+} cation, as similar emission schemes under UV excitation are characteristic of TiO_6 (Ti^{4+}) octahedral complexes seen in titanium functionalized spinels, zirconates, and stannates [73]. It is proposed that the mechanism involves empty 3d orbitals of the Ti^{4+} ion, that are well hybridized with states at the conduction band consisting of surrounding cation orbitals, and a valence band consisting of mainly O^{2-} orbitals. Upon excitation, charge-transfer occurs from the O^{2-} $(2p)^6$ electron into the empty (3d) conduction band of the Ti^{4+} ion, yielding an excited state Ti^{3+} ion. Blue emission occurs with the radiative recombination of the trapped electron as Ti^{3+} ion into the hole attracted to the nearest O^{2-} ions [69].

Excitation at the lower energy absorption band at 490nm corresponding to the $T_{2g} \rightarrow E_g$ transition of the Ti^{3+} ion in octahedral sites yields a broad IR emission band that peaks at 805nm with FWHM approaching 200nm, which would allow for broader tunability than that of the Ti-doped Al_2O_3 laser. However, thermal quenching occurs at room temperature, decreasing the overall emission intensity when compared to values at liquid nitrogen temperatures [68].

When pumped within the absorption edge in the UV emission decay has been reported to be exponential and have a strong temperature dependence, with decay times decreasing with increasing temperature. At 77K, Bausa et $al.$ reported an emission lifetime of 25 µs (at 465nm) [68], whereas room temperature values reported by Jouini et $al.$[71] and Sato et al [69]. were reported as 5.7 µs (at 455nm) and 6.6 µs (at 490nm), respectively.

Measuring the emission at 805 nm corresponding to the $T_{2g} \rightarrow E_g$ electron transition (λ_{exc} = 490nm) yields a non-exponential decay time that also has a strong temperature dependence, where decay constants decrease with increasing temperature. These values for short and long lifetimes from liquid nitrogen to room temperature range from 4.2 – 0.8 µs and 41-10 µs, respectively [68]. These lifetime values are slightly larger than the values reported for the

exponential decay in the IR of the Ti-doped Al_2O_3 single crystals at room temperature (3.15 μs, $\lambda_{exc} = 490nm$), which corresponds to a similar electronic transition [74].

1.7.3 Ongoing Challenges

One of the biggest issues that exists with the doping of single crystals are the dopant gradients that result with production. This issue has been seen in 0.3 at% Ti-doped $MgAl_2O_4$ made by micro-pulldown technique, where no gradient was seen in the pulling direction, but a large gradient seen in the axial direction [75]. In this case, the highest dopant concentration exists at the edges with minimal (if any) dopant within the crystal. A similar result has been seen in the case of Ti-doped Al_2O_3 grown by the Kyropolous technique [76]. A schematic representation of this radial dopant gradient for the previously mentioned case of 0.3% Ti-doped $MgAl_2O_4$ single crystal can be seen in Figure 1.15.
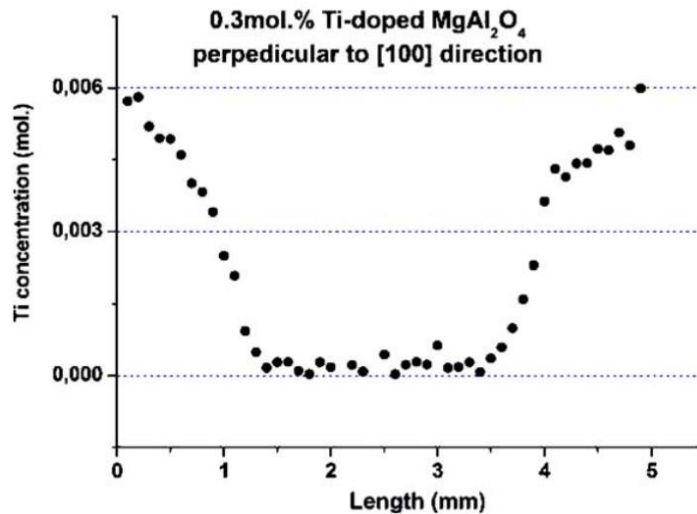
Figure 1.15 Electron probe microanalysis profile (axial) of 0.3 mol% Ti-doped $MgAl_2O_4$ spinel single crystal made by micro pulldown technique. Taken from [75] with permission.

Considering the known drawbacks that arise with Ti doping of single crystal $MgAl_2O_4$, alternative production methods have yet to be explored. The known benefits of using CAPAD as a method to produce homogeneously doped, highly transparent polycrystalline materials and the wide emission range of Ti-doped single crystals leave room for the exploration. A future chapter devoted to this exact topic, exploring the consolidation of Ti-doped $MgAl_3O_4$ from nanocrystalline reactants, and considerable spectroscopic and microstructural characterization.

2. CAPAD DENSIFICATION OF NANOCRYSTALLINE MGO: EFFECTS OF GRAIN SIZE AND HUMIDITY

2.1 Background

The use of CAPAD for the production of fully dense MgO was first performed by Chaim *et al.* [15], who showed transparency and sub 100nm grain sizes at relatively low processing temperatures (<800 ℃). Since then, many works have been done in an attempt to enhance transparency, including use of very fine grain sizes and high pressures [16], very high temperatures [17], and LiF additives [18].

Despite the benefits of enhanced densification with small particle size, little work has been done utilizing the high heating rates of CAPAD to explore these effects. In addition, the inherent hygroscopicity of MgO and the large amounts of work showing the potential benefit on low temperature consolidation (cold sintering) in its presence [28], yield necessity for study. This chapter is devoted to the examination of the effect of grain size and water vapor absorption on the densification rates of nc-MgO densified using CAPAD, as little work has been done studying these specific variables on the densification kinetics in pressure-assisted densification methods. Although the temperatures used here are significantly higher than those used in cold sintering, we believe that the water absorption aspects of this study are relevant to cold sintering in addition to the densification of MgO in CAPAD.

2.2 Experimental Procedure

Commercially available nc-MgO powder with a nominal grain size of 50 nm (US Res. Nano.) was used. In order to obtain finer powder, commercially available $Mg(OH)_2$ powder (US Res. Nano.) with a reported 10 nm grain size was also used. All starting powders were calcined at 500 °C for 2 hours in a box furnace and *immediately* placed under vacuum and transferred into an Ar glove box to prevent surface adsorption of water. The resulting powder from 10 nm $Mg(OH)_2$ reaction was planetary ball-milled at 300 RPM for 3 hours, ground using a mortar and pestle and sieved through 325 mesh in a glove box.

In order to study the effect of water content on the densification, the converted MgO powder (from $Mg(OH)_2$)was exposed to ambient environments for 24hrs. Some of the converted powder was exposed to a humid environment for varying durations (1-3hr), in which ambient air was filtered and passed through the blubber filled with UHP water with flow-controller.

0.55 g of powder was packed in a graphite die with a 9.5 mm inner diameter. The die and plunger assemblies were uniaxially pressed at 200 MPa for 5 minutes at room temperature prior to densification in CAPAD. The CAPAD parameters were 150 MPa, approximately 180 °C/min to 700 °C, with a 5 min. hold time at 700 °C. After CAPAD, the samples were polished and characterized. The RD of the samples was measured using the Archimedes method and the theoretical density for MgO (3.58 g/cm³).

Densification as a function of time, $\rho(t)$, was measured using the real time data acquired during CAPAD experiments and the relation:

$$\rho(t) = \frac{m(t)}{V(t)} = \frac{m(t)}{A_c(l_0 - l(t))} \tag{5}$$

where m is mass, V, is the sample volume, A_c is the cross-sectional area, l_o initial height and l is the height change measured during the experiment. Since the A_c of the die is known, and l_o can be measured, the denominator in Eq. 2 depends only on the length contraction during the experiment. The load frame in our CAPAD instrument has a displacement resolution of 0.0747 μm and a load measurement accuracy of 0.4%. As is typically done[11], [35], we removed thermal expansion/elastic deformation caused by machine and graphite tooling from $l(t)$ by running blank die experiments with the same temperature profile.

It was expected that the MgO powders exposed to humidity would lose mass during densification. To correct the densification curves, the measured chamber pressure was integrated to obtain total pressure, normalized, and converted to mass multiplying by the measured mass loss. The $m(t)$ data was corrected for time dependent chamber pressure change from system (caused by temperature changes and de-gas from the chamber/tooling) by removing data recorded using a blank die experiment.

Acquisition of densification rate curves was performed by taking the derivative of the relative density vs. time curves, acquired experimentally by procedures previously discussed.

2.3 Results and Discussion

To ensure completed reaction of the starting $Mg(OH)_2$ to MgO, DSC-TGA (TA Instruments, SDT-Q600) was performed. **Figure 2.1a** shows DSC-TGA on the starting $Mg(OH)_2$. There is a sharp weight loss and corresponding endothermic peak starting around 300 °C, which is attributed to the $Mg(OH)_2 \rightarrow MgO$ reaction. Although the weight loss continues until ~700 °C, most of the weight loss occurs by ~500 °C. One of the primary goals is to produce MgO with finer grains, so choosing a low temperature is crucial to minimize grain growth. To confirm that 500 °C
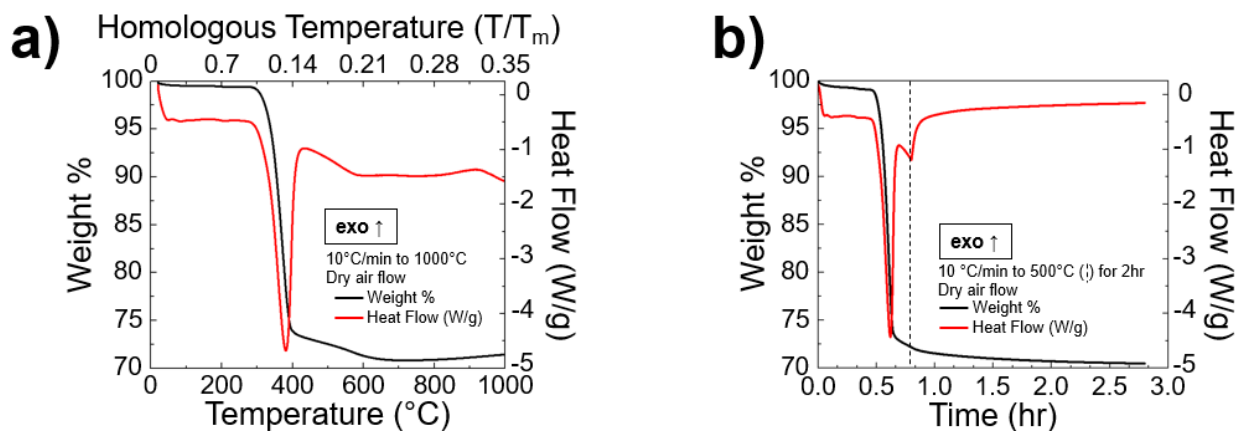
Figure 2.1 2.1a) DSC-TGA of as-received Mg(OH)$_2$, showing endothermic reaction and weight loss beginning at 300°C. 2.1b) DSC-TGA of Mg(OH)$_2$ emulating furnace reaction for discussed experiments.

for 2 hours in a box furnace are sufficient reaction conditions, we replicated the conditions in the DSC-TGA (10 °C/min to 500 °C holding for 2 h); these results are shown **Figure 2.1b**. The weight loss indicates negligible weight loss after 2 hours hold and over 95% conversion.

SEM Micrographs (**Fig. 2.2b**) of converted powder reveals very fine grain sizes. The histogram shown in the inset show an average grain size, AGS is 29 nm with a tight distribution (standard deviation of 13 nm). By contrast the commercially available nc-MgO powder (**Figure 2.2a**) has a measured AGS of 42 nm with a broader distribution (22 nm). We consider a
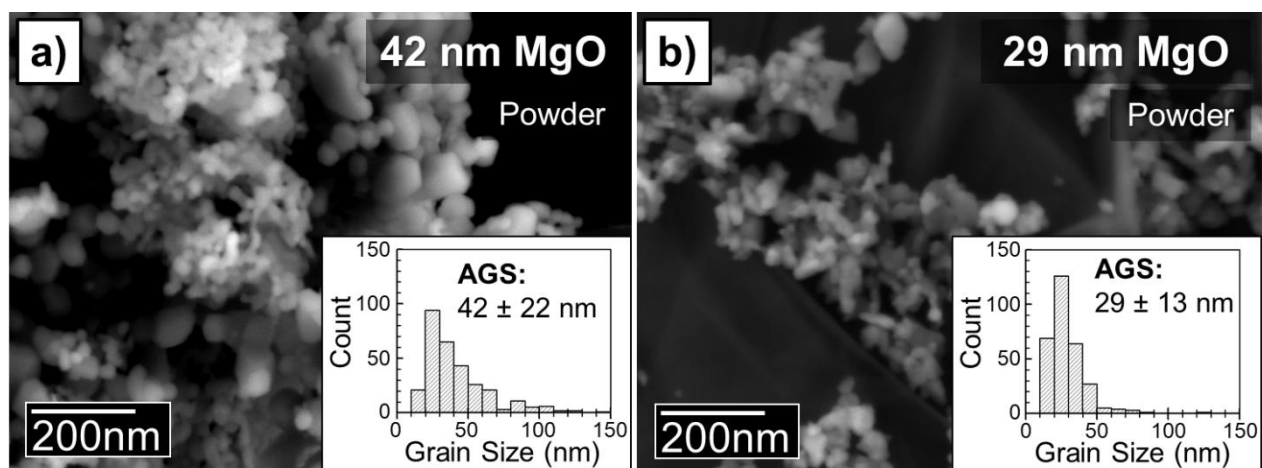
Figure 2.2 SEM of processed MgO powders from as-received 50 nm MgO (figure 2.2a) and reacted 10nm Mg(OH)$_2$ (figure 2.2b)

conservative estimate, since only grains that could be clearly identified within SEM resolution were counted to obtain AGS.

To ascertain the absorbed amount of water, the powder was weighed before and after exposure to the environment. The data is reported according to two limiting case conditions: 1) Assuming absorbed water remains H_2O on the MgO surface and 2) Assuming absorbed water reacts with MgO to form $Mg(OH)_2$. The latter is a good assumption since the hydroxylation reaction is thermodynamically favorable ($\Delta G < 0$) at room temperature. The results are tabulated in two columns, wt% H_2O-gained and mol% $Mg(OH)_2$ in **Table 1.1**. The results indicate 0-17 wt% H_2O or 0-39 mol% $Mg(OH)_2$. XRD did not suggest the formation of crystalline $(MgOH)_2$ after the exposure.

Table 2.1 Summary of 5 samples prepared with varying weight percent of adsorbed species, ordered by wt% adsorbed by powder pre-CAPAD. Wt% calculations are both a function of the initial weight (pre-absorption). Mol% $Mg(OH)_2$ calculations consider all weight gained as contributing to $Mg(OH)_2$ formation.

Powder	wt% H_2O gained pre CAPAD	mol% $Mg(OH)_2$ pre CAPAD	wt% H_2O lost post CAPAD	Bulk R.D. (%)	Composite Bulk R.D. (%)*
42 nm MgO	0	0	0.9	93.5	-
29 nm MgO	0	0	0.9	96.1	-
	7.6	17.0	7.7	95.3	-
	10.8	24.2	8.4	93.2	95.7
	17.2	38.5	10.9	92.9	99.5

*Assuming all remaining H_2O post CAPAD converts to $Mg(OH)_2$
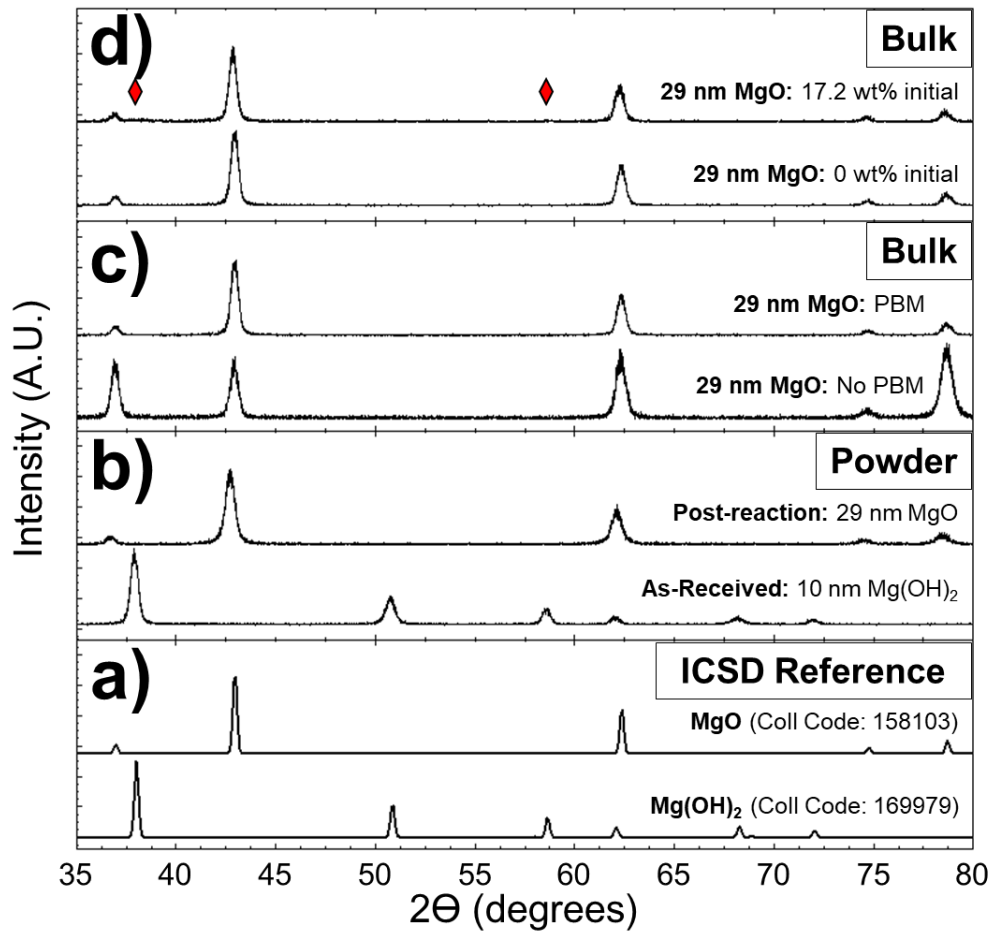
Figure 2.3 X-ray diffraction of powders and densified bulk samples. ICSD references included for comparison.

Figure 2.3a,b shows XRD of as-received 10 nm $Mg(OH)_2$ powder and converted MgO powder along with ICSD references for comparison. The as-received powder shows only $Mg(OH)_2$ peaks while the converted shows only MgO peaks, supporting DSC-TGA data. Interestingly, the XRD profile of the sample densified from 0 wt%-29 nm powder initially showed a different peak intensity-ratio compared to the 42 nm powder and MgO standard, indicating preferential grain alignment (texturing) in the bulk sample (**Fig. 2.3c**, No PBM). Planetary ball-milling (PBM) of the 29 nm powder prior to densification in CAPAD resulted in a bulk sample with same peak intensity-ratio as the standard, solving the texturing issue (**Fig. 2.3c**, PBM). XRD of densified

bulk from powder with the highest water content, 17.2 wt% initial, shows very minor hydroxide peaks indicated by red diamonds.

Micrographs of fracture surfaces of bulk samples are shown **Figure 2.4a,b**. Densified samples from 29 nm MgO powders with and without exposure to humidity were examined. The microstructure is remarkably similar and shows a fine nanocrystalline grain structure. The AGS was measured using the longest distance across a grain for >300 individual grains from each micrograph, and the corresponding distributions can be found in the inset. Interestingly, there was no significant difference in AGS and distribution; The AGS = 51.6 ± 18.1 nm for the 0 wt% and 52.1 ± 21.9 for the 17.2 wt% sample.
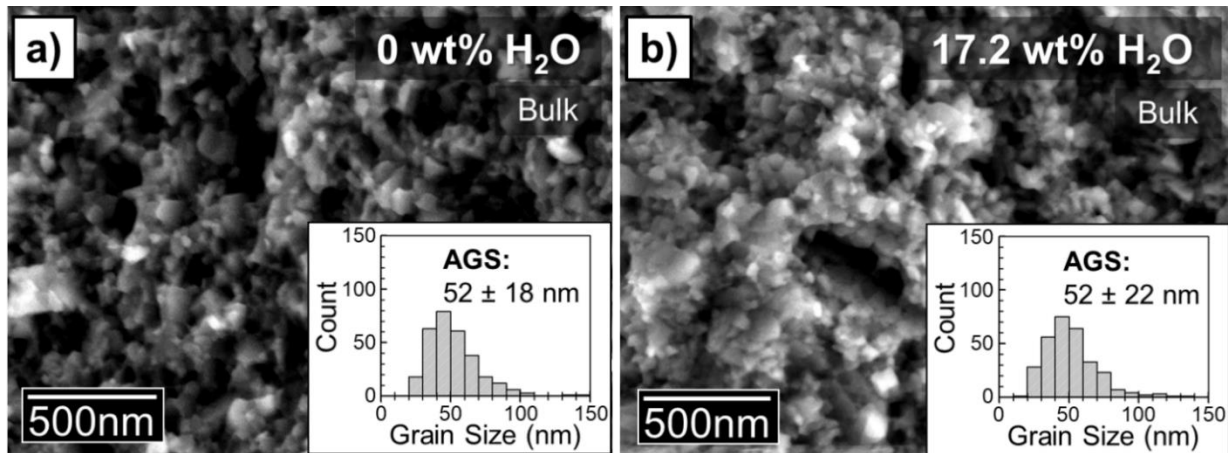
Figure 2.4 Micrographs of fractured surfaces of samples densified from 29nm powder exposed to no humidity (0 wt%) and for longest duration (17.2 wt%). Grain size distributions are inset

Figure 2.5 shows the RD of the CAPAD densified samples as a function of grain size and dswt% H_2O gained. The RD of the sample densified from 42 nm MgO was 93.5 % while the sample densified from 29 nm powder was 96%. We attribute the higher density of the latter to increased densification rates caused by finer grain sizes as will be discussed below. Although 96% density is typically interpreted as 4% porosity, we believe that the porosity in the densified samples could be significantly lower. Grain boundary (gb) regions are known to have lower density (more open

structure) compared with grain interiors especially in nanocrystalline materials. The RD can be lowered even with little/no porosity. In a sample with AGS = 51 nm, a 4% reduction in RD can be caused by an effective grain boundary density of 31% of the density of the MgO theoretical density (assuming gb thickness = 1 nm) which is in-line with calculations and experimental observation of grain boundaries structures in MgO[77].
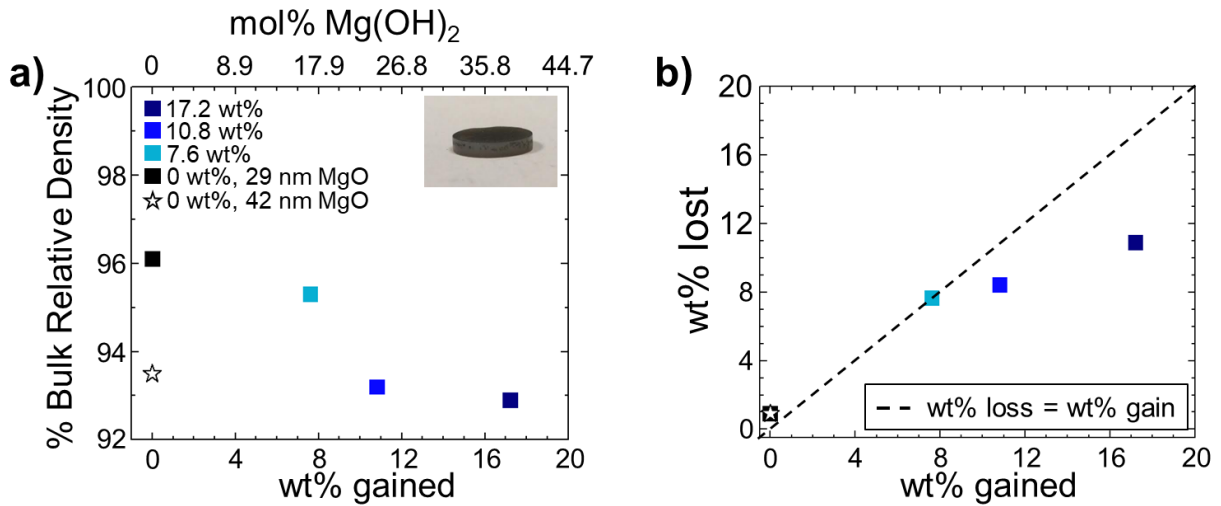
Figure 2.5 Relative density of CAPAD processed samples as a function of wt% gained of powder pre-CAPAD shown in Fig. 2.5a. The inset shows a picture of a densified sample (0 wt% 29nm MgO) with 9.5mm diatmeter. Fig. 2.5b) Measured wt% gained of powder before CAPAD vs. sample wt% lost after CAPAD.

The processing times and temperatures required for densification are in-line with previous CAPAD of nc-MgO. Chaim *et al.* achieved densifying >98% RD of nc-MgO at 150MPa and 825°C for 5 minutes [15]. TB Tran and coworkers used significantly higher pressures (300-500 MPa) and temperatures ranging from 650 to 800°C and achieved >99% RD with very fine grain sizes ~25 nm [16].

The presence of Mg(OH)$_2$ (2.34 g/cm^3, 61% of MgO) in the bulk sample can also contribute to lower RD. Figure 3b plots the *wt*% gained by the powder vs. the wt% lost after densification; the dashed line represents same wt% lost = wt% gained. We attribute the weight loss to water leaving the sample as a result of the conversion of MgO from Mg(OH)$_2$ during the densification process. The low wt% samples lost the same wt% as they initially gained, while the higher wt% samples retained some of the gained weight, likely as a hydroxide phase. The conclusion that the weight loss was in the form of water vapor is corroborated by chamber pressure measurements taken during the CAPAD experiments (**Figure 3c**). These results show that the 0 wt% samples show virtually no increase in chamber pressure, while the 7-17wt% samples have a significant pressure rise starting a low temperature ~100 °C and increasing dramatically at ~ 350 °C corresponding to the Mg(OH)$_2$ to MgO conversion (**Fig. 1a**). If we assume that the remaining water is Mg(OH)$_2$ after densification (suggested by XRD shown in **Figure 1c**, top), the RD of composite MgO-Mg(OH)$_2$ bulk samples can be recalculated and is shown in Table 1. Recalculation suggests all samples exhibit RD>95%.
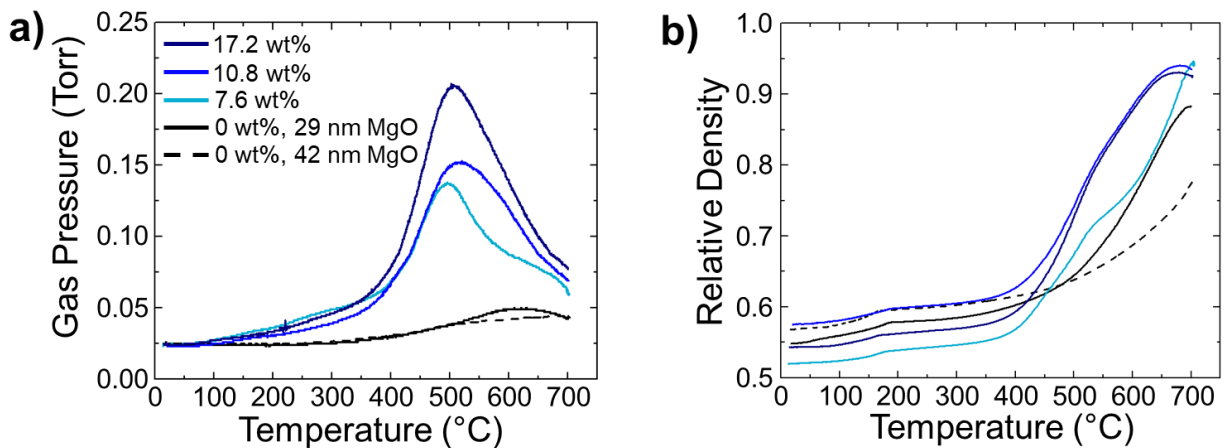
Figure 2.6 Vacuum curve vs. temperature (**Fig. 2.6a**) and relative density vs. temperature (**2.6b**) for MgO samples densified in CAPAD from powders of varying grain size and wt% gained of H$_2$O.

A temperature of 700 °C required to densify MgO is surprisingly low given its high melting point. However, the grain sizes of the starting powder are fine < 50 nm. Another reason for a low densification temperature is the possible influence of gained water or hydroxide which has been previously shown to influence densification temperatures in MgO and other oxides.

Since 7-17 wt% samples have significant weight loss, we used the chamber pressure (vacuum) data recorded during CAPAD experiments (**Figure 2.6a**) calibrated with measured weight loss (Table 1) to find time dependent mass, $m(t)$. The measured chamber pressure was integrated to obtain total pressure, normalized, and converted to mass multiplying by the measured mass loss. The $m(t)$ data was corrected for time dependent chamber pressure change from system (caused by temperature changes and de-gas from the chamber/tooling) by removing data recorded using a blank die experiment.

The RD as a function of temperature is shown in **Figure 2.6b**. The dry samples (0wt%) show small amount of continuous densification that significantly increases at ~500 °C.). These curves are similar to densification vs. temperature curves calculated for MgO by Reis and Chaim using diffusion HIP equations proposed by Artz [24], modified to include grain growth [23]. Thus we believe the densification in our "dry" MgO is controlled by diffusional densification mechanisms. By contrast the 7-17 wt% samples have significantly lower onset of densification temperatures ~350 °C.

In order to further investigate possible mechanisms, we found $\dot{\rho}$ by numerically differentiating the $\rho(t)$ curves. The densification rate as a function of temperature for the samples with varying wt% H_2O is shown in **Figure 2.7a**. $\dot{\rho}_{max}$ vs. homologous temperature, T/T_m is plotted in Figure 4b. The $\dot{\rho}$ of the 0 wt% nc-MgO increases continuously at low T and shows a relatively broad peak at ~ 600 °C, 0.21 T/T_m. The curve shapes are similar to $\dot{\rho}$ vs. T we measured previously for nanocrystalline yttrium stabilized ZrO_2 (nc-YSZ) and nc-Si [35]. The magnitude of the maximum densification rate, $\dot{\rho}_{max}$ = 2.7 × 10⁻³ s⁻¹ for nc-MgO densified from larger grain size (42nm) is in the same order of magnitude as that previously measured for nc-YSZ and nc-Si ($\dot{\rho}_{max}$ ~5 × 10⁻³ s⁻¹). The grain size of the starting powder of both nc-Si and nc-YSZ was ~50 nm. By
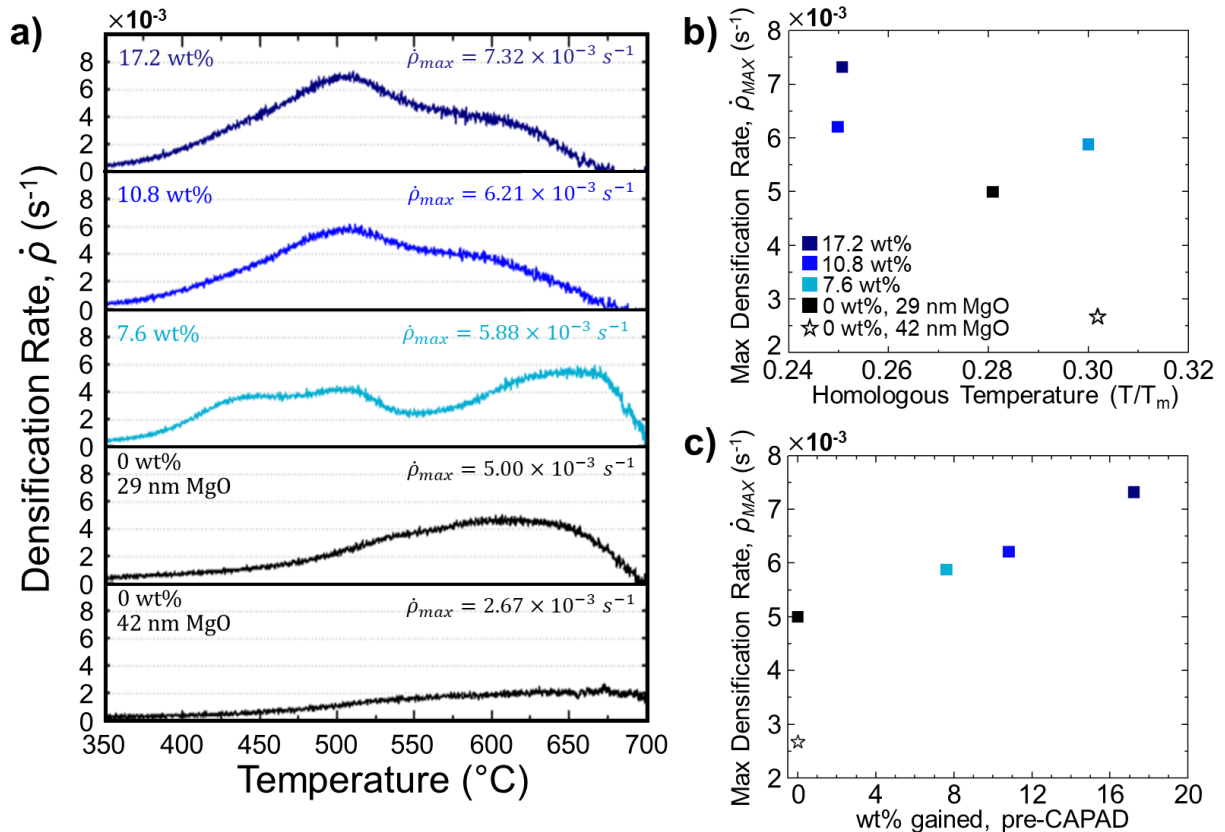
Figure 2.7 Densification rate vs. temperature curves for MgO powder samples of varying grain size and wt% adsorbed (**Fig. 2.7a**). The maximum rates of these curves are plotted with respect to homologous temperature in **Fig. 2.7b**, showing the change in the location and magnitude of the maximum rate depending grain size and wt%. **Fig. 2.7c** shows the maximum densification rate as a function of wt% gained.

contrast, $\dot{\rho}_{max} = 5 \times 10^{-3}$ s^{-1} for nc-MgO from finer grain size powder (29 nm) is approximately 2 times higher. We attribute higher $\dot{\rho}$ to the finer grain as suggested in (Eq. 1)

On the other hand, the 7.6 wt% H_2O sample shows dramatically different shape of the $\dot{\rho}$ vs. T curve compared with the dry 0wt% samples; instead of one broad $\dot{\rho}$ peak, there are now two. The peak in the higher T regime is diffusion-controlled densification as mentioned previously. The $\dot{\rho}_{max}$ is located in a similar as the 0 wt%, but there is an additional peak with similar magnitude located at 500 °C, 0.18 T/T_m. The two distinct peaks suggest that there are differing controlling densification mechanisms in these regions. In addition, the relative magnitude of these two peaks switch, *i.e* the $\dot{\rho}_{max}$ is now at the lower T/T_m regime for the high H_2O content samples. Interestingly, the curve for higher wt% samples (10.8wt% and 17.2wt%) still shows two peaks, but the peaks are more convoluted. This observation implies that there continue to be controlling densification mechanisms, but the dominant densification mechanism is different for samples with higher wt% H_2O. Increases in wt% gained increases $\dot{\rho}$ (**Figure 2.7c**), but do not significantly change the location of the peaks, suggesting that the densification mechanism remain the same. We attribute this lowered densification temperature to particle/grain rearrangement caused/triggered by Mg(OH)$_2$ to MgO conversion. Mg(OH)$_2$ forms around MgO after exposure to moisture and during densification. It converts to MgO resulting -54.8% volume change and triggers grain rearrangement under uniaxial press to reach higher packing density before the volume diffusion as final stage of sintering occurs.

2.4 Chapter 2 Summary and Conclusions

This study demonstrated the role of the grain size and the absorbed water/hydroxide on the densification of MgO below 50nm of grain size. The densification of nanocrystalline ceramic powders is an important approach to obtain nanocrystalline bulk samples with properties significantly different from their larger-grained counterparts. However, significant reduction of grain size increases the specific surface area to a level where surface absorption and formation of hydroxide occur, and the influence of those on the densification became more significant. We believe the demonstrated results in this paper provide additional insight into the densification of nano-ceramic powders.

Chapter 2 is co-authored with Professor Javier E. Garay and Dr. Yasuhiro Kodera, and is published in Scripta Materialia 2019, 169, 33-37. The dissertation author was the primary investigator and author on this paper.

3. FROM NANOPOROUS TO TRANSPARENT MgAl₂O₄ – NANOSTRUCTURAL FLEXIBILITY BY REACTTION DENSIFICAITON OF METASTABLE POWDERS

3.1 Introduction

3.1.1 Motivation

Polycrystalline $MgAl_2O_4$ spinel is one of the most important structural ceramics and has been shown to exhibit robustness in many engineering applications due to its high melting temperature, attractive mechanical properties, chemical stability, and transparency from UV well into the IR. Successful examples of highly dense ceramics include near theoretical light transparency [14], [78]–[80] and high hardness in extremely fine-grained ceramics [44]. Nanoporous ceramics are also extremely important for catalysis[81] and have shown promising results for ductility [82]. Notable advances in nanoporous spinels include fabrication of hollow nanowires of zinc spinel [5], enhanced catalytic behavior in Cu-Al spinel [6], and successful fabrication of spinel nanocomposites [7]. In contrast to dense ceramics, nanoporous magnesium aluminate spinel (MAS) has received considerably less attention. However, the inherently good chemical and mechanical properties make MAS attractive as a robust nanoporous material.

The most popular techniques for achieving dense bulk MAS are free sintering, hot pressing (HP), hot isostatic pressing of pre-reacted spinel powders [14]. Current-Activated, Pressure-Assisted Densification (CAPAD) has also successfully been applied [41]–[43], [80]. Due to lack of commercially available powders, an alternative approach involving the simultaneous reaction/densification of α-Al_2O_3 – MgO in CAPAD was attempted, resulting in highly transparent MAS [52]. The resulting grain sizes were well into the micron range, which could prove detrimental to hardness due to the well-known Hall-Petch relationship.

In this work, we chose to use metastable γ-Al_2O_3 and nano-sized MgO as reactants instead

of the stable α-Al_2O_3 and large-sized MgO. CAPAD was chosen for the consolidation of the reactants due to the highly controllable heating rate, pressure, and temperature parameters. We hypothesize that use of metastable, nanocrystalline reactants would increase reaction and densification rates for two reasons: 1) The inherently small grain sizes (< 30 nm) would decrease diffusion distances 2) γ–Al_2O_3 is a will utilized catalyst well-known to be highly reactive [83]. We show that by understanding both the reaction and densification processes one can utilize the γ-Al_2O_3 – MgO nanocrystalline reaction as a platform for achieving either nanoporous or fully dense transparent ceramics by simple tuning of processing parameters. In addition, we believe this is the first kinetic analysis of the γ-Al_2O_3 – MgO reaction.

3.1.2 Previous Work on Densification of MAS for Transparency

Successful CAPAD experiments for the densification of polycrystalline $MgAl_2O_4$ typically involve methods to achieve transparency, including use of very slow heating rates[34], [42], innovative load application techniques [43], and high pressures [44]. To further enhance transparency several groups have utilized LiF as a densification additive, which has been shown to increase green densities via particle rearrangement during compaction in addition to etching particle surfaces resulting in enhanced diffusion. However, use of LiF in CAPAD densified $MgAl_2O_4$ has yielded very large grain sizes, which may be detrimental to the mechanical properties [45]–[48].

Challenges existing with commercial availability of $MgAl_2O_4$ spinel powder have led some to take advantage of the reaction between MgO-Al_2O_3, where the formation of spinel occurs at elevated temperatures upon combining the reactants 1 to 1 by mole. Both individual compounds are widely accessible and are available in a variety of different particle sizes and purities. This route was first employed via free-sintering, where high temperatures (1900°C) and additives were

used to achieve full density [12].

Pressure-assisted methods for the consolidation of $MgAl_2O_4$ from reactants are sparse as pre-reaction generally occurs before densification, with additives and complicated processing steps frequently being used to enhance reactivity and final density [51]. The use of hot-isostatic pressing (HIP) has been successful with the reaction densification of additive-free, polycrystalline $MgAl_2O_4$ at 1540°C, 200 MPa [14]. HIP in conjunction with the use of smaller-grained, highly-reactive γ-Al_2O_3 as a reactant was shown to enhance densification rates and yield higher densities at lower temperatures in reaction-densified, hot-isostatically pressed (HIP) transparent $MgAl_2O_4$ [84], [85]. HIP has been shown to yield highly transparent $MgAl_2O_4$ samples, but lengthy processing steps and long durations at high temperatures are typical. Despite the work that has been done using reactants for the formation of spinel, none of the works assess the kinetics of reaction.

The use of CAPAD for additive-free, reaction densification of optical materials has been has been shown previously in Ce:YAG [86]. Meir *et al.* utilized CAPAD for the consolidation of $MgAl_2O_4$ from large-grained reactants, with LiF and high temperatures used to enhance density and ensure complete reaction.[52].

The significant benefits LiF/additives have on the densification, transparency, and reactivity of spinel from reactants are obvious, but rapid grain growth occurs in its presence. Additive-free methods that have been explored involve complicated procedures and extended durations at high temperatures, also resulting in runaway grain growth. Both of these techniques to achieve high densities and the resulting large grain sizes can be detrimental to uses involving high mechanical strength. The availability of *very* fine-grained nanocrystalline reactants and the enhanced densification that occurs as a result of nanocrystallinity[53], provides a necessity for further exploration.

3.1.3 Previous Work on Porous MgAl₂O₄

Porous $MgAl_2O_4$ spinel are often formed using complicated and lengthy processing technicques, including foam gelcasting [8], [9], and alumina tempating [10]. A reaction method using low-cost bauxite and magnesite minerals was presented by [87]. Although these prior works achieved some level of success, large, micron sized pores typically resulted. Use of CAPAD as a processing method for porous materials provides enhanced flexibility allowing for control over microstructures and grain sizes, and has been successful with creating porous materials of many different compositions [88]. However, utilizing CAPAD as a tool for consolidation of porous $MgAl_2O_4$ has not been considered, and provides necessity for further study.

3.2 Experimental Procedure

3.2.1 Powder Processing

10nm $MgOH_2$ (99%, US res. Nano) was reacted in a box furnace at 10°C/min to 500°C in air for a total of 2 hours, to ensure full conversion to MgO. The powder was immediately placed under vacuum during cooling to decrease potential for moisture adsorption. Thorough analysis of the reaction from $Mg(OH)_2$ → MgO can be referred to in chapter 1 of this work. Similar processing was used for the preparation of γ-Al_2O_3 (<50nm, 99.99% purity, Inframat Advanced Materials). Upon cooling, powders were weighed 1:1 by mol and planetary ball milled in ultra-high purity water using Si_3N_4 media for 3 hours at 200 RPM. The resulting slurry was centrifuged, fully dried in a vacuum furnace, mortar and pestled, and sieved through 325 mesh. To decrease re-hydroxilation after wet planetary ball milling, the mixed reactants were exposed to a final furnace step occurred at 500°C for 2 hours in air. The final powder was placed under inert gas to avoid

potential for moisture contamination, vacuum packed for storage, until ready for densification. No additives were used in the preparation of nanocrystalline reactant powders.

3.2.2 CAPAD Procedure

The resulting reactant powder was packed in a graphite die with a 9.5 mm inner diameter, inserted into a larger die with 19mm inner diameter. The die and plunger assemblies were uniaxially pressed at 100 MPa for 5 minutes at room temperature prior to densification in CAPAD. Three series of densification experiments were performed. The initial densification temperature sweep was performed at 100 MPa, approximately 180 °C/min to the desired hold temperature, with a 5 min. hold time. Densification and reaction kinetics experiments were performed at 100 MPa, approximately 100 °C/min, with experiments quench cooled or held for 5 minutes. Transparent, polycrystalline $MgAl_2O_4$ was achieved at 100 °C/min to 1400 °C for 5 min using a two-step pressure application procedure similar to what is seen in [43]. The initial pressure (5 MPa) was maintained until 1350°C, where the final pressure was applied (100 MPa) and the hold temperature was reached. All experiments were performed without any densification additives.

Temperature measurements ≤ 1200°C were taken utilizing a thermocouple touching the surface of the graphite die containing powder. For hold temperatures exceeding 1200°C a pyrometer was focused through a hole drilled through the larger die assembly, focused on the surface of the die containing powder.

3.2.3 Phase and Microstructural Characterization

Sample densities were measured using Archimedes method with ultra-high purity water unless porous samples were obtained post-densification, where meticulous geometric measurements were taken. Densification rates were measured using similar method that was previously discussed in chapter 2 of this work.

X-ray diffraction (XRD) of powder and bulk samples was performed using a Panalytical X'pert x-ray diffractometer. Microstructural characterization via scanning electron microscopy was done using a Zeiss Sigma 500 scanning electron microscope. Analysis of grain size occurred via measurement of micrographs of fractured surfaces, where the longest distances of a grain were measured for 300 random grains, for each micrograph.

To quantify the amount of reaction that occurred between each temperature step and hold duration, the peak areas of peaks from approximately 41-48° were assessed. Peak locations were fixed at 43.088°, 44.868°, and 45.806°, corresponding to peak locations of MgO, $MgAl_2O_4$, and γ-Al_2O_3 powders, respectively. The phase quantity (mol and volume fraction) at temperatures/durations was determined by deconvolution of individual peak areas. Peak areas were converted to mol fraction using a calibration curve constructed from XRD measurements of powders of precisely measured phase compositions, which can be seen in A-1 of the appendix.

3.2.4 Transmission Measurements

Transparent $MgAl_2O_4$ samples polished using diamond slurry down to 1μm. Subsequent In-line transmission measurements were taken of using an Agilent Cary 5000 UV-VIS-NIR spectrophotometer.
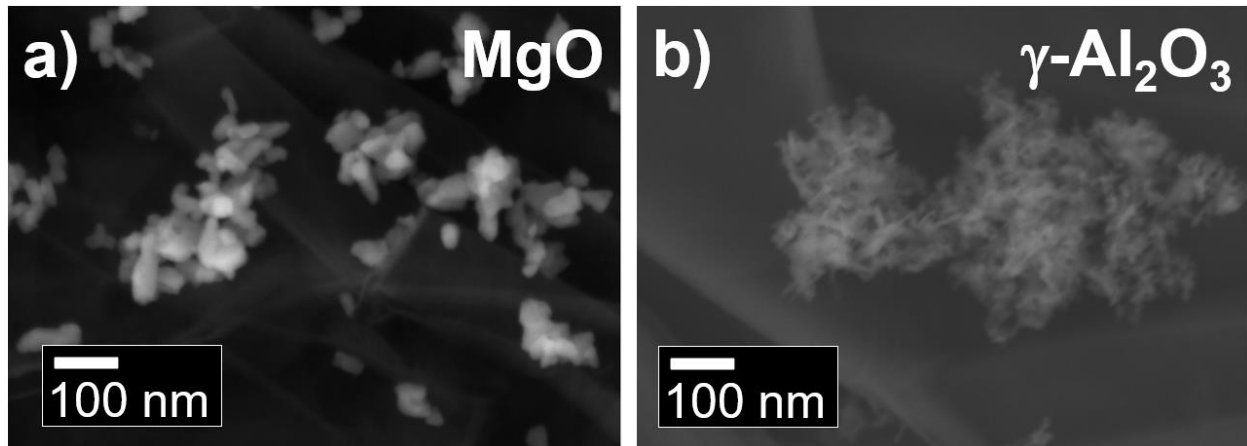
Figure 3.1 SEM Micrographs of starting reactant powders and the resulting processed mixture of reactant powders, showing very fine (sub-30 nm) grain sizes.

3.3 Results

3.3.1 Powder Characterization

SEM micrographs were taken of the processed reactant powders as shown in **Figure 3.1**. The dispersed MgO powder showed a very fine particle size approaching 30nm, and the particle size of the dispersed γ Al_2O_3 was difficult to quantify but appears to be well below 30nm. The initial reactant powders are *significantly* smaller than shown in the work of [52], where ~300nm α-Al_2O and 10-20 µm MgO agglomerates were reaction densified in CAPAD. Upon wet mixing and concluding processing steps previously indicated, the combined reactant powders appear to be comparable in size to that of the initial reactant powders.

XRD of the processed reactant powder was performed to verify phase purity. The resulting 2Ө scan of the reactant powder can be seen in **Figure 3.2** where peaks corresponding to MgO and γ Al_2O_3 are shown to align with their respective ICSD references, indicating a sufficiently mixed reactant powder that consists of both initial phases. Exposure of the combined reactants to 500°C
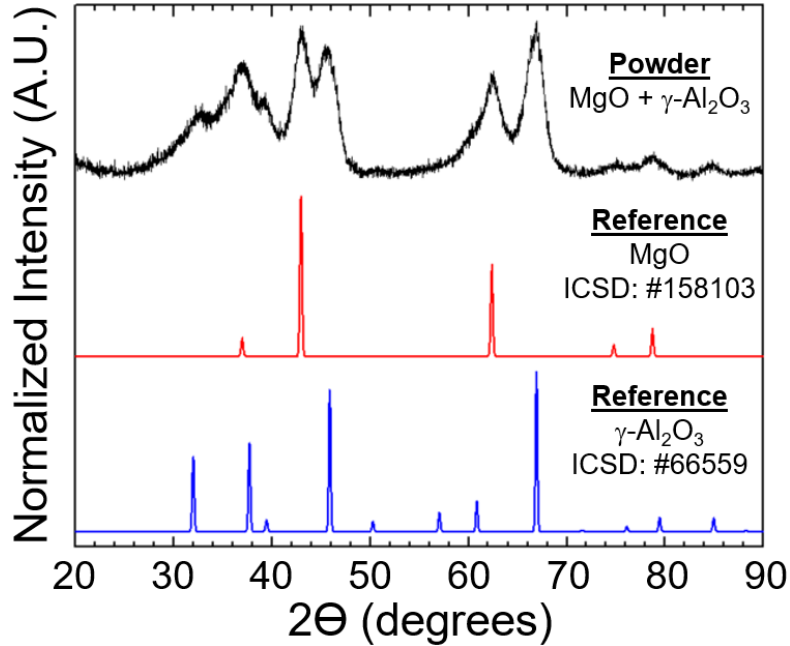
Figure 3.2 XRD of processed MgO – γ Al$_2$O$_3$ reactant powder

for 2 hours in air during processing appears to be low enough to not provoke reaction between the two initial phases, as seen by the absence of MgAl$_2$O$_4$ peaks. This temperature and duration are also sufficient to react any Mg(OH)$_2$ that may have been present after planetary ball milling in water - which has been previously shown to occur spontaneously in nanocrystalline MgO in the room temperature and pressure in the presence of H$_2$O [53]

3.3.2 Analysis of MgO-γ Al$_2$O$_3$ Phase Transformation to MgAl$_2$O$_4$ Spinel

To better understand the evolution of the reaction between the nanocrystalline reactants in CAPAD, no hold and 5-minute hold experiments were performed at temperatures from 550°C to 1000°C. XRD was taken of the initial reactant powder and samples densified at each temperature and hold duration, which can be seen in **Figure 3.3**. These results show spinel formation occurring

at an extremely low temperature of 550°C, with a majority of the reaction completing upon reaching 1000°C.
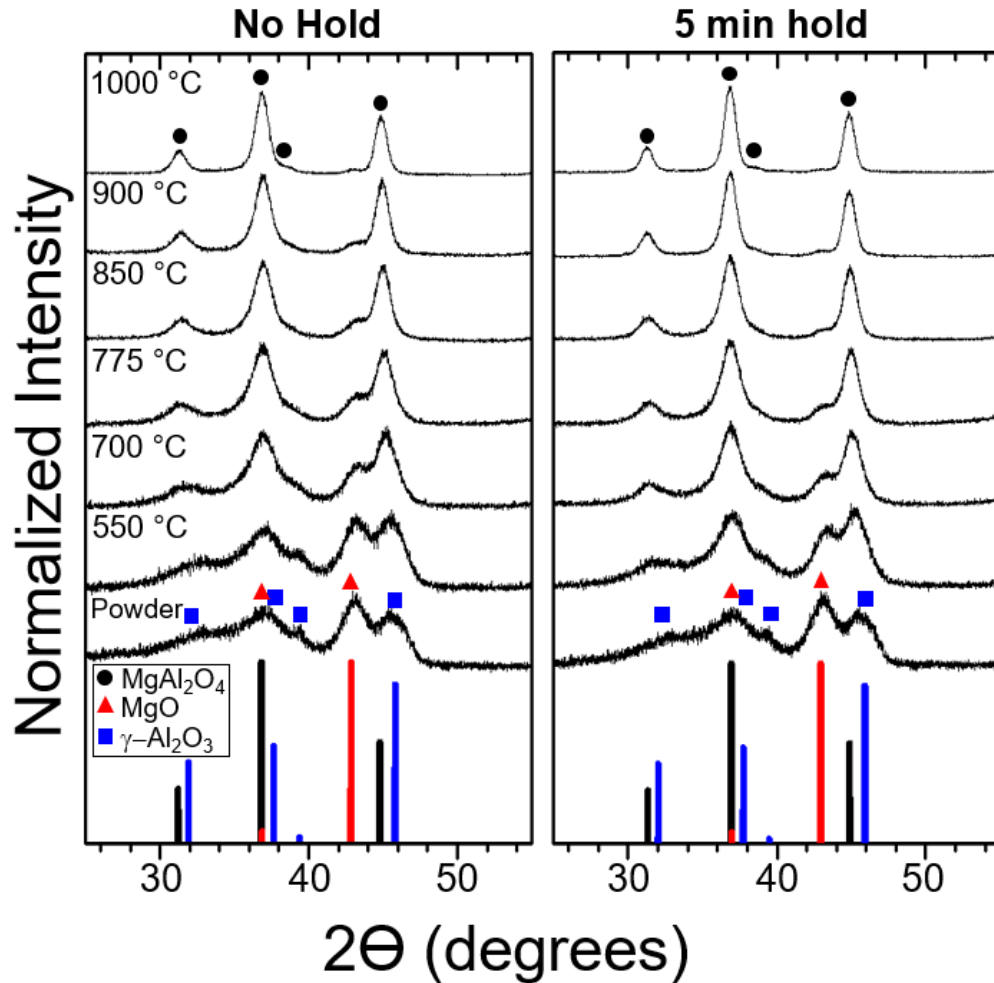
Figure 3.3 XRD of CAPAD samples from MgO – γ Al$_2$O$_3$ for powders subjected to 0 minute and 5 minute hold. MgAl$_2$O$_4$ ICSD collection code: 31373; MgO ICSD collection code: 158103; γ Al$_2$O$_3$ ICSD collection code: 66559

Figure 3.4a shows mole fractions of MgAl$_2$O$_4$ and the remaining reactants for each temperature and hold duration. As temperature increases, the amount of product increases as the amount of reactant decreases. At each temperature, the amount of product increases with hold time. When 1000°C is reached, nearly 70 mol% of the measured sample was MgAl$_2$O$_4$ after 5 minutes (~81 vol%). Larger grained reaction densification experiments in CAPAD showed < 20% relative amount of spinel after 1 hour hold at 1000°C [52]. In the kinetics experiments of Sinhamahapatra

54

et al. [58]*, <10%* relative amount of spinel was achieved in free-sintering of micron-sized reactants at 1240°C after 5 minutes.
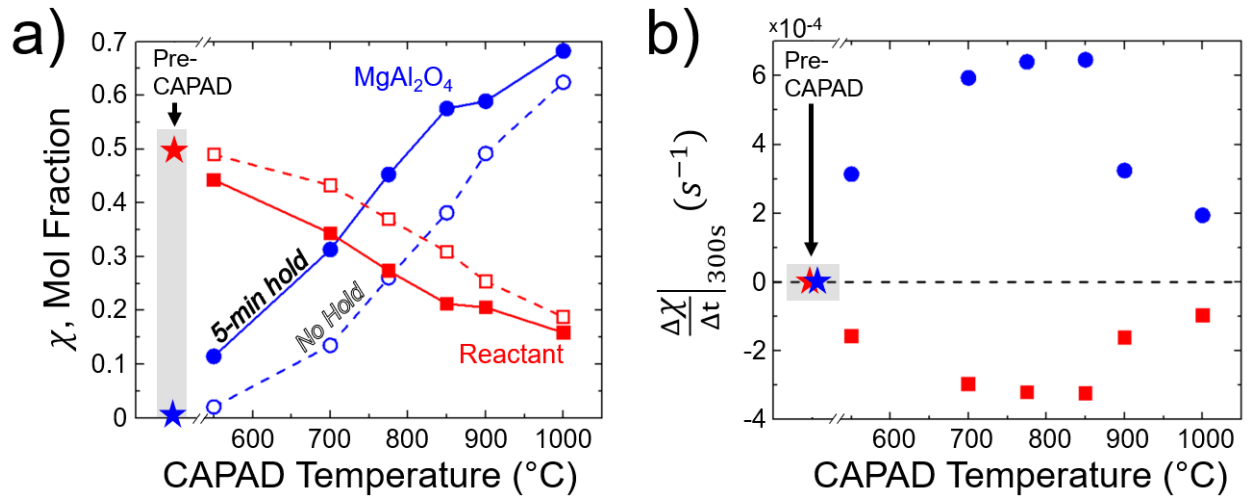
Figure 3.4 a) Mol fraction vs. CAPAD temperature for product ($MgAl_2O_4$) and reactants (MgO, Al_2O_3). Experiments held at 0 (hollow) and 5 minutes (filled). b) Rate of mol reacted per second for products and reactants

To clarify the results in **Figure 3.4a**, the amount of reaction occurring at each temperature for a specific time duration was considered. The difference between mol fractions for 5-minute hold and no hold at each temperature is plotted in **Figure 3.4b**. A considerable amount of reaction is shown to occur at 550°C, a result that is corroborated with previous results. The rate at which the reaction occurs peaks at 850°C and decreases at higher temperatures, which is attributed to the onset of grain growth and a large amount of the reaction already occuring.

The best available kinetic data for spinel reaction (growth) kinetics is from reactive diffusion couples. Isothermal, time dependent reaction has been well studied by various researchers, using classic single-crystal diffusion couple experiments [54] and polycrystalline diffusion couple experiments at both atmospheric [55] and at elevated pressures [56]. These studies all found only one reaction product ($MgAl_2O_4$) between MgO and α-Al_2O_3 interfaces with a parabolic time dependence of growth, indicating diffusion-controlled growth governed by:

$$\Delta x = \sqrt{2kt} \tag{1}$$

where k is the growth rate constant (m^2/s), Δx is the thickness of the spinel layer (m), and t is time (s).

Time dependent experiments were performed for comparison with previous reactive diffusion results by running several CAPAD experiments for varying durations at 700°C. The average spinel volume fraction for these experiments and their corresponding standard deviations are shown in **Figure 3.5a**. We developed a simple geometric model (Appendix, A-2) to compare expected volume fraction from spinel growth rates. We assumed a planar interface and that the reactants, MgO and γ-Al$_2$O$_3$ are both cubes with edge lengths b and growth is diffusion controlled (obeys Eq.1). If we further assume that the overall volume of the reactants and spinel product does not change, we can write the spinel volume fraction as:

$$X_S = \frac{\sqrt{2kT}}{2b} \tag{2}$$

Using a realistic edge length (based on SEM, **Fig. 3.6**) the data in **Figure 3.5a** can be fit with ranging from 5×10^{-20} $m^2/s \le k \le 1 \times 10^{-19}$ m^2/s. This range is indicated with red dashed lines on **Fig. 3.5a.** The constant volume assumption is well justified since the volume change from reactants to MAS product is *less than* 2%.

The diffusion couple work [55] did not study temperatures as low as 700°C, so rate constant was calculated by extrapolation using the Arrhenius relationship:

$$k = A exp\left(\frac{-E_a}{RT}\right) \tag{3}$$

Where R and T are ideal gas constant (J·mol^{-1}·K^{-1}) and temperature (K). Activation energy and pre-exponential constant (E$_a$=540 kJ/mol and $A = 1.276 \times 10^3$ m^2/s, respectively) from P. Zhang *et al.* [55] was used. The extrapolated reaction rate constant is 1.34×10^{-26} m^2/s, which is 6 orders of magnitude different from our k values of our time dependent experiments (**Fig. 3.5**).
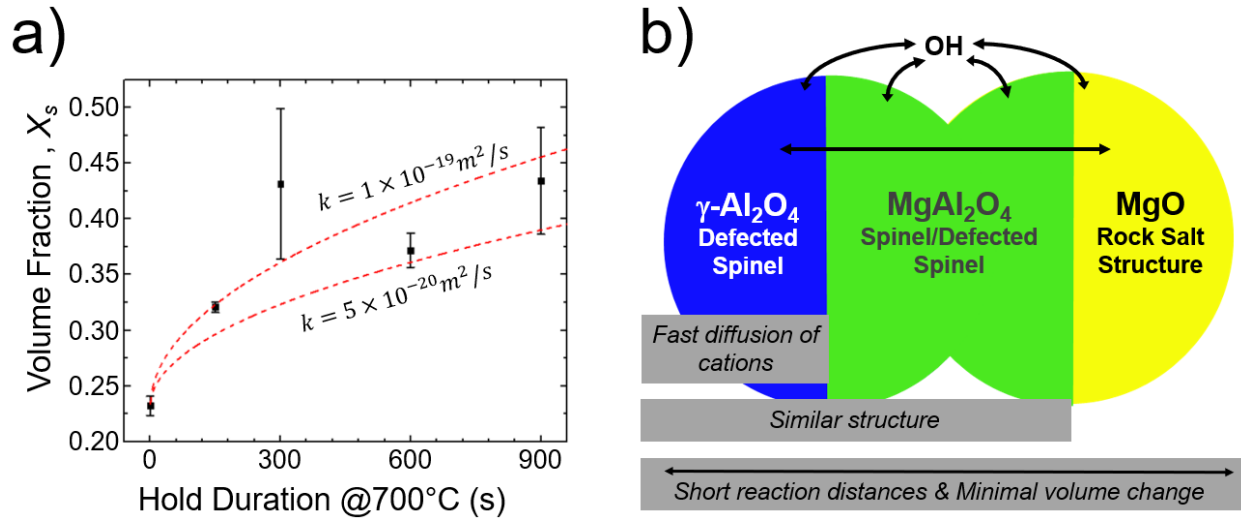
Figure 3.5. a) Volume fraction MgAl$_2$O$_4$ as a function of duration for reactant powders densified in CAPAD, with red dashed lines indicating fits that correspond with minimum and maximum k values. **b)** Proposed mechanisms for enhanced diffusion in MgAl$_2$O$_4$ from metastable/nanocrystalline reactants.

The large difference in reaction rates clearly indicates that the reaction mechanism we observe at 700°C are different from those polycrystalline coupling experiments from 1200°C to 1600°C using α− Al$_2$O$_3$ and MgO. Reaction constants of depend not only on the diffusion though the product phase, but on diffusion through the reactants. Thus, we believe the drastic reduction in temperature and faster reaction kinetics is due to the structural differences between α− Al$_2$O$_3$ and γ− Al$_2$O$_3$.

α− Al$_2$O$_3$ is the most stable alumina phase and has a corundum structure. Both α−Al$_2$O$_3$ and metastable γ-Al$_2$O$_3$ have close-packed O sublattices, but due to the reduced occupancy of the Al cation sublattice, γ-Al$_2$O$_3$ has a much lower density compared to α-Al$_2$O$_3$ (3.98 g/cm^3 compared

to 3.66 g/cm^3). Although the understanding of the complexity of the structure has been continuously evolving [83], [89], γ-Al$_2$O$_3$ can be described as a cubic spinel structure with cation vacancies [89]. The high fraction of cation vacancies explains the density difference and strongly suggests that cation diffusion through the γ-Al$_2$O$_3$ should be considerably faster than the α−Al$_2$O$_3$ lattice, consistent with the faster kinetics we observe.

A further cause for the increased reaction kinetics is the similarity between the spinel product and the reactant γ-Al$_2$O$_3$ lattice. In the MAS structure base (AB$_2$O$_4$), the Mg cations occupy the A tetrahedral and the Al cations occupy the B octahedral sites. In γ-Al$_2$O$_3$, Al occupies both A tetrahedral sites and B octahedral sites. The previously mentioned cation vacancies are required to ensure the stoichiometry of Al$_2$O$_3$. Considering the very similar base structure, it is possible that part of the growth of MAS can be accomplished simply by Mg ions filling the cation vacancies in the reactant γ-Al$_2$O$_3$.

In addition to the faster diffusion and lattice similarities we believe that water/OH adsorption on the surfaces of the of the nano-reactants as well as MAS product plays an important role on the reaction. MgO nano-powders readily absorb water from the atmosphere and forms magnesium hydroxide. We previously showed that densification rates of MgO are strongly affected by OH adsorption [53]. Similarly, the reactivity of γ-Al$_2$O$_3$ is known to depend on OH contents. Wischert *et al.* showed that OH groups stabilize (110) surfaces [83]. OH content decreases with temperature, making γ-Al$_2$O$_3$ more reactive. Dong *et al.* showed that hydrogen within the bulk structure also helps stabilize the OH on the surface [89]. OH content is also important in MAS. Bromiley *et al.* showed that nonstoichiometric MAS can contain a significant amount of OH. Although we did make an effort to reduce OH content by annealing the reactant powders in air at 500°C, the powders likely contain residual water. The mechanism for OH

interaction in the reaction process is complex and cannot be ascertained with the results here, thus future work will be necessary to quantify its role. **Fig. 3.5b** summarizes the mechanisms responsible for the substantially increased reaction kinetics observed here compared to previous work.

3.3.3 Densification Rates of MgAl$_2$O$_4$ From Reactants

Results from section 3.3.2 show that most of the reaction has taken place before 1000°C, with the reaction beginning to slow at 850°C. With this under consideration, samples were densified in CAPAD varying hold temperature from 1000°C to 1300°C (5 min hold at T) under a pressure of 100 MPa to examine the grain growth and bulk density of the densified spinel. **Figure 3.6** shows SEM micrographs of fracture surface of ceramics densified at various temperatures. **Figure 3.7** shows the grain size and relative density of the densified MAS samples. The grain sizes and densities range from 30nm and 65% at 1000°C to 375nm and full density at 1300°C.
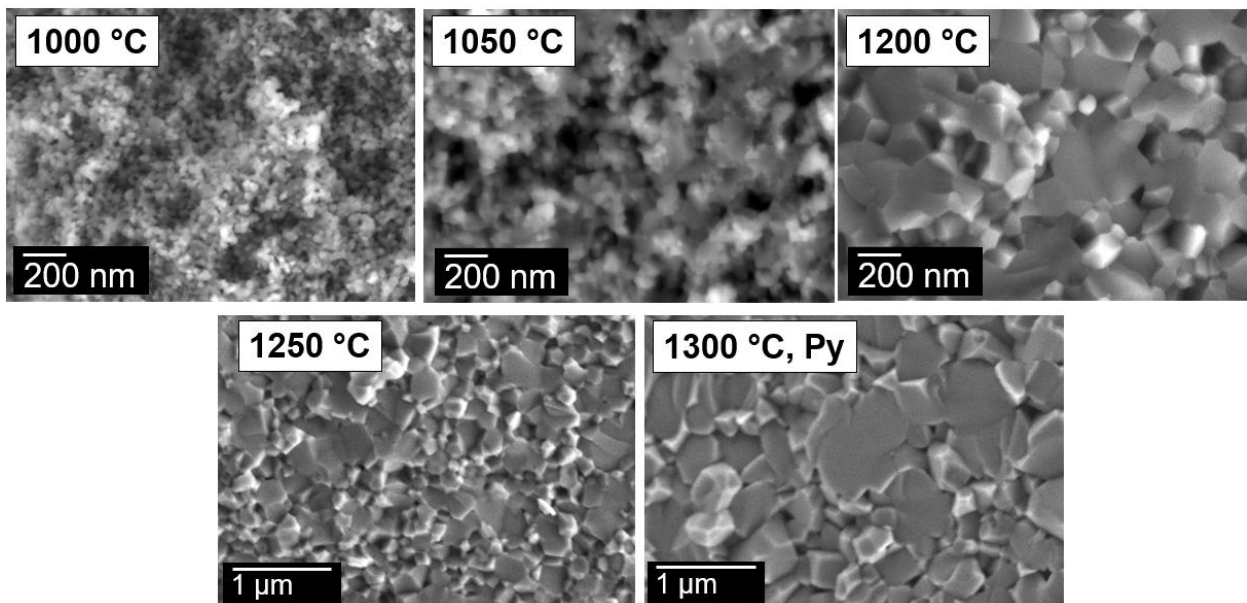
Figure 3.6 SEM micrographs of MgAl$_2$O$_4$ fractured surfaces from CAPAD densified samples heated at ~180-200 °C/min to temperature for 5 minutes under 100 MPa.
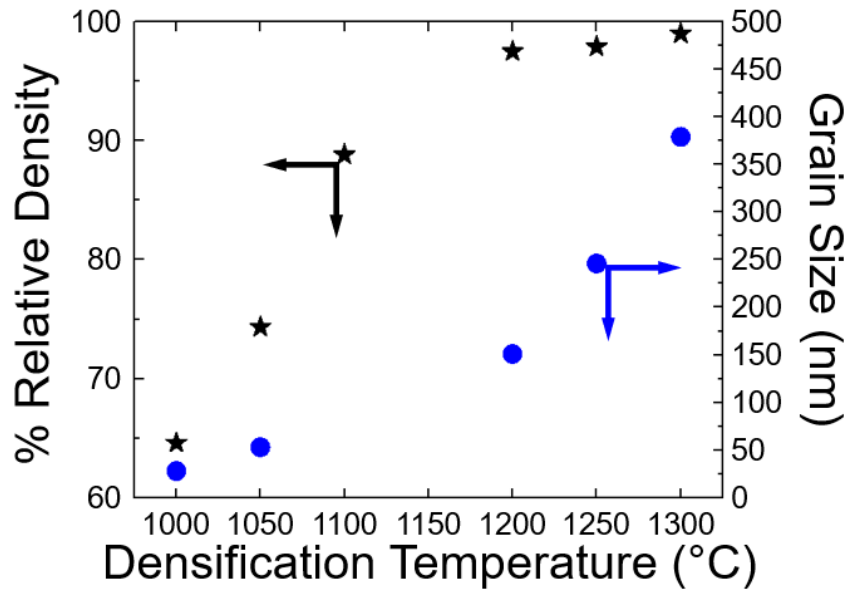
Figure 3.7. Bulk relative density/grain size vs. densification temperature for CAPAD densified samples heated at ~180-200°C/min to temperature for 5 minutes under 100 MPa

Fig. 3.6a and **Fig. 3.7** show that the sample densified at 1000°C has remarkably small (~ 30nm) grains. Comparison with initial reactant grain sizes indicates that although the reactants have been almost fully transformed to mas, surprisingly little grain growth occurred. Moreover, **Fig. 3.6a** reveals nanosized pores, confirming that the resulting sample is nanoporous spinel with a porosity of 35% and grain size of ~30nm. Despite the high porosity, these nanoporous samples are quite robust as will be shown in *section 3.5*.

Relative densities greater than 95% were achieved at temperatures exceeding 1200°C, with near-full density/full density (> 99%) occurring at 1300°C or greater. Grain growth increases substantially at temperatures where densities greater than 95% are achieved (1200°C) as expected since at these densities, pores are no longer effective grain boundary pins. The maximum grain size is 380nm at >99% at 1300°C for 5 minutes. These results vary significantly from previously published $MgAl_2O_4$ reaction densification values, indicating the benefits of fine-grained reactants and CAPAD processing. Experiments where $MgO - \gamma\ Al_2O_3$ (150 and 50nm, respectively) are reaction densified via free-sintering/HIP yielded relative densities >95% at temperatures

exceeding 1300°C, with grain sizes exceeding 500nm [84]. Reaction densification in CAPAD with larger grained reactants in the presence of LiF achieved near full density at approximately 1250°C (1600°C with no additive), with grain sizes well into the micron range.

We also measured the *in-situ* densification rate of the reaction/densification process. This was done by CAPAD processing the reactant powder at a constant heating rate of 100°C/min to 1200°C under 100 MPa pressure. Thermal expansion of the machine, die, and sample were removed by subtracting the crosshead extension data from a blank die experiment utilizing comparable heating rates. Relative density vs. temperature was plotted using a live theoretical density that considered theoretical densities of each component of the composite at specific temperatures, where specific component volume data was acquired via XRD and calibration curve. Values used in composite theoretical density calculations for each component are $MgAl_2O_4$ (3.58 g/cm^3), MgO (3.58 g/cm^3), and g Al_2O_3 (3.66 g/cm^3). Composite theoretical density versus temperature is plotted in the inset in **figure 3.8a**, where theoretical density decreases with increasing temperature (more $MgAl_2O_4$ formation). Densification rates were acquired via taking the derivative of the relative density vs. time curve.
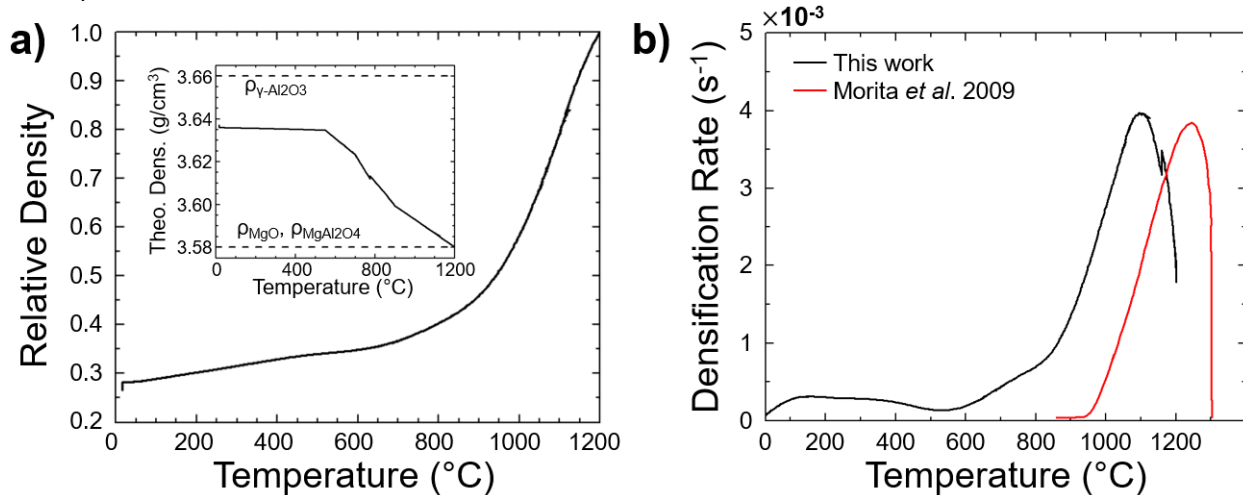
Figure 3.8. a) Relative density vs. temperature with *inset* composite theoretical density vs. temperature for sub 30nm MgO + γ Al_2O_3 reactant powder taken to 1200°C at 100°C/min, 100MPa. b) Densification rate vs. temperature calculated from relative density in fig. 3.8a, with Morita *et al.* (2009) densification rate of 360nm $MgAl_2O_4$ at 100°C/min, 80MPa [34].

61

In-situ measured relative density vs. temperature is shown in **figure 3.8a**. The results show that density increases relatively slowly from room temperature to 600°C. A transition occurs from ~ 600°C – 850°C, followed by a rapid increase in density from approximately 1000°C to 1200°C. These changes in relative density vs. temperature can be better appreciated by observation of the densification rate vs temperature, shown in **figure 3.8b**. The regions in the densification rate curve that correspond with the previously mentioned regions in **figure 3.8a** signify different densification mechanisms as discussed below.

Low densification rates from room temperature to ~550°C are attributed to temperature activated particle rearrangement. The slight increase in rate from 550-850°C corresponds to the temperature range where the reaction rates are highest (**figure 3.4b**), which we attribute densification in this temperature window to particle/grain rearrangement caused by the MAS reaction. The maximum densification rate occurs at approximately 1075°C and approaches 4×10^{-3} s^{-1}.

Comparable maximum densification rates have been measured in the work of Morita *et al.*, where 360nm $MgAl_2O_4$ powder was subjected to the same heating rate as in this work (100°C/min) and 80 MPa in CAPAD. These parameters yielded a maximum densification rate approaching 4×10^{-3} s^{-1} at 1240°C [34], ~165°C lower than measured here. Morita *et al.*suggested that grain-boundary sliding was the predominant densification mechanism, which we also attribute to our work.

It has been previously shown that differences in pressure do not significantly alter the temperature at which maximum densification rates occur [35]. However, the size dependent effects on the densification kinetics have been previously highlighted by the work of Rahaman [21], where the maximum densification rate occurred 500°C less when reducing particle size from 500nm to

10nm in CeO_2. We attribute the reduction in maximum densification rate temperatures (165°C decrease) to the finer grains of the MAS in our work. This can be explained by enhanced surface area with decreasing grain size, where dominant densification mechanisms (grain boundary sliding) are active that have a strong dependence on surface area.

3.3.4 Transparent Polycrystalline Spinel

Typical methods for CAPAD densification of transparent $MgAl_2O_4$ involve slow heating rates [34] or use of additives [45], both of which can yield high transparency but may also yield large-grained microstructures. The use of two-step pressure application for the densification of transparent $MgAl_2O_4$ was shown by Wang and Zhao [43], and allows for use of faster heating rates typically seen in CAPAD.

Transparent $MgAl_2O_4$ samples from nanocrystalline reactants were densified using a 2-step pressure application method where 5 MPa was applied until 1350°C, followed by 100 MPa at 1400°C for 5 minutes. This technique was used successfully on two different reactant powders, where two different types of MgO powder (30nm MgO reacted from $Mg(OH)_2$, 42 nm MgO) were
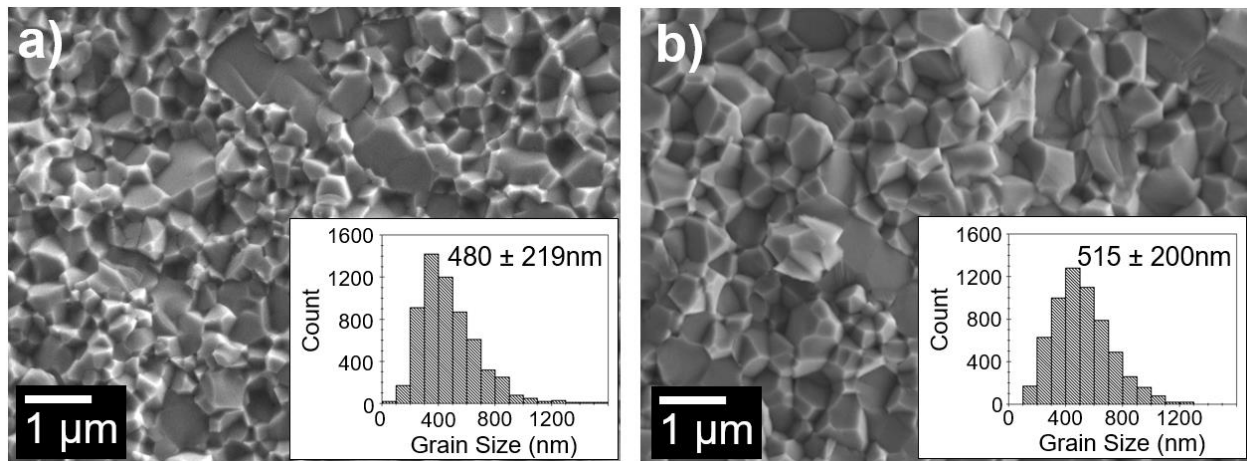
Figure 3.9. SEM micrograph of transparent $MgAl_2O_4$ fractured surfaces, densified using a 2-step pressure application (5 MPa → 100 MPa at 1350 °C) and a 5-minute hold at 1400C in CAPAD. Grain size distributions are inset. **Fig. 9a** densified from reactant powder - 99% $Mg(OH)_2$ → MgO (30 nm) + 99.95% γ-Al_2O_3 (<30nm) **Fig. 9b** densified from reactant powder - 99.95% MgO (42 nm) + 99.95% γ-Al_2O_3 (<30nm)

used in conjunction with γ Al_2O_3 in the initial reactants. SEM micrographs from these two samples can be seen in **figure 3.9**, where a dense (>99.7%), equiaxed microstructure is apparent with no evidence of porosity. Grain sizes of these samples hover around 500nm, which is significantly less than reaction densified $MgAl_2O_4$ CAPAD experiments that utilize additives for densification (well into μm range) [52] – further exemplifying the benefits of very-fine nanocrystalline reactants.

Reflection-scattering-absorption (RSA) plots including the in-line transmission data (black line) for the samples considered in **figure 3.9** can be seen in **figure 3.10**. A detailed explanation of the acquisition of RSA plots can be found in [90]. Transparent samples made from 30nm MgO (from 99% $Mg(OH)_2$ reaction) (**figure 3.10a**) and g Al_2O_3 (99.95%) approach 20% transmission at 550nm, whereas samples made from 42 nm MgO (99.95%, as received) (**figure 10b**) approach 30% transmission at 550nm. Both samples exhibit high levels of transparency in the near IR, with the sample in **figure 3.10b** approaching 80% at 2500nm. The decreased transmission in the visible in **figure 3.10a** is likely due to considerable amounts of absorption, indicated by the green line. Absorption in CAPAD densified $MgAl_2O_4$ has previously been attributed to carbon contamination
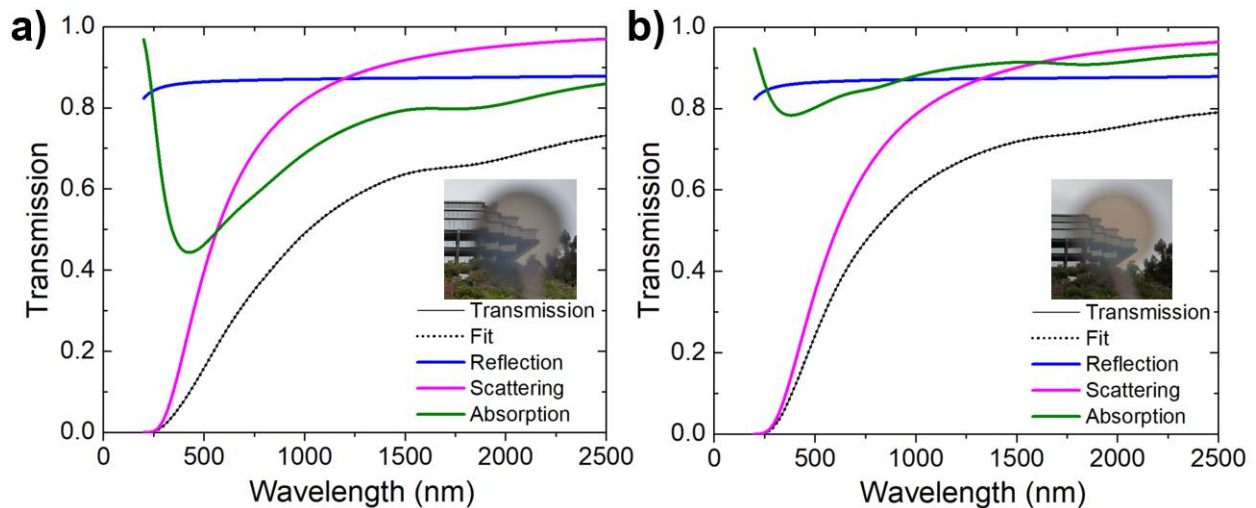
Figure 3.10. Reflection-Scattering-Absorption (RSA) plots of transmission data for reaction densified using parameters discussed in Fig. 3.9. **Fig 3.10.a)** RSA plot of sample densified from reactant powder - 99% $Mg(OH)_2$ → MgO (30 nm) + 99.95% γ-Al_2O_3 (<30nm) **Fig 3.10.b)** RSA plot of sample densified from reactant powder - 99.95% MgO (42 nm) + 99.95% γ-Al_2O_3 (<30nm)

and color centers (F$^+$ -center) generated from oxygen vacancies [91], but the exact source in these samples is unclear. Scattering also exists in both samples (magenta line) and could potentially be caused by phase segregates yielded by incomplete reaction or slight offsets in stoichiometry. However, XRD results of samples at these temperatures indicate phase purity. Modifications of the initial reactant stoichiometry have previously been shown to enhance transparency [85] in reaction densified samples via free-sintering, although a comparable study in CAPAD has not been considered.

3.3.5 Compression Testing of Nanoporous Ceramics

To highlight the robustness of the nanoporous samples, several partially dense samples were sinter-forged via load and hold experiments at various hold temperatures. The intentions of these experiments are not to achieve full density, but to exhibit the capabilities of this processing method and the strength of the resulting nanoporous sample post densification. Transparent MAS by sinter-forging has been shown in the recent work of Nečina *et al.*[92], for reference.
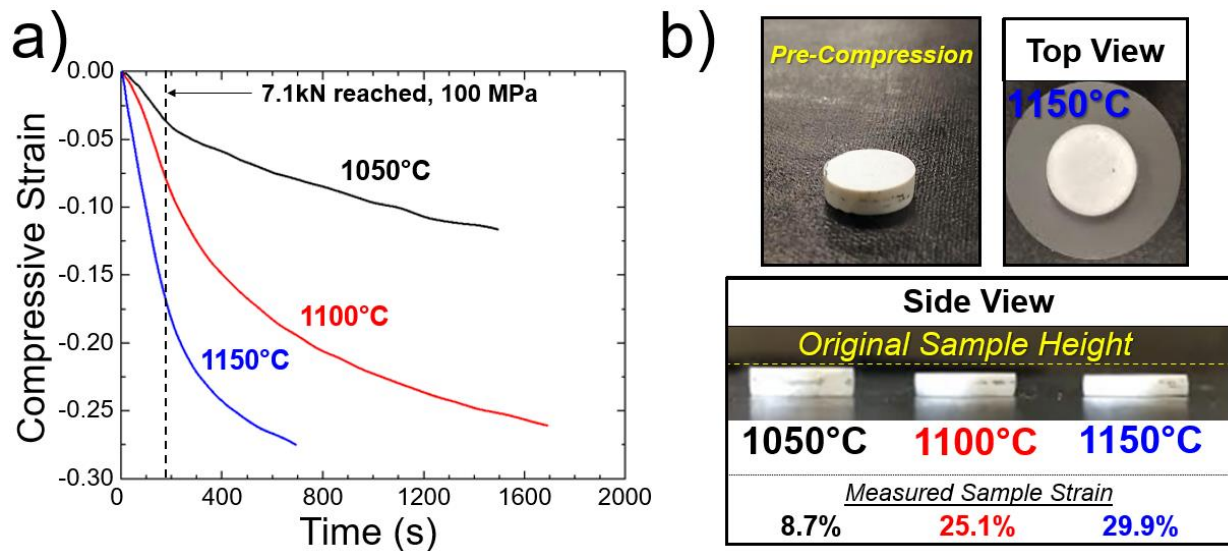
Figure 3.11. a) Compressive strain vs. Time (s) for 3 samples deformed in CAPAD at varying temperatures. **b)** Sample photos, including pre compression and post compression. Deformation temperatures and measured strain values are also shown.

Samples used for load and hold experiments were first densified in CAPAD at 1000C for 5 minutes, under 100 MPa. Microstructures of these samples can be seen in **Figure 7**, where a grain size of ~30nm and composite relative density of ~65% were measured. Sample surfaces were polished flat and parallel prior to compressive strain experiments. **Figure 11a.** shows compressive strain for 3 different samples held at specified temperatures while a load of 7.1 kN (initially 100 MPa, no confining pressure) is applied and held in CAPAD. A clear dependence of temperature and compressive strain is apparent, where upon full load application (180s) the sample at 1150 C has strained ~15%, whereas at 1050 C only ~3% strain has occurred.

All samples remained intact regardless of experimental conditions, with no evidence of cracking. **Figure 11b.** shows sample photos post CAPAD densification and after compression experiments. The sample compressed at 1150C resulted in ~30% strain in *less than* 15 minutes and yielded a full sample.

3.4 Chapter 3 Summary & Conclusions

The results in chapter 3 display the benefits of using nanocrystalline materials for the reaction densification of $MgAl_2O_4$ spinel, and the overall flexibility of the nanocrystalline reactant/CAPAD densification route for the production of samples with varying densities, grain sizes and functionalities.

First, a significant temperature (several hundred °C) reduction for the onset and completion of reaction is accomplished. This is likely due to a significant decrease in diffusion lengths (powders <30nm), or enhanced reactivity of the nanocrystalline reactants. Whatever the case, it is either the previous mechanisms in the diffusion literature appear to not apply at the temperatures we are investigating, or the activation energies for formation of spinel from $\alpha-Al_2O_3+MgO$ are

different to that of γ-Al_2O_3+MgO. These results leave room for subsequent kinetics investigations using the γ-Al_2O_3+MgO reactant combination.

Second, the use of nanocrystalline reactants yields enhanced densification kinetics and densities at lower temperatures. Maximum densification rates occurred at >150°C less than those seen in larger grained $MgAl_2O_4$ densification. In addition, full density was achieved at 300°C less than comparable reaction densification studies with larger grained reactants/no additives. Reduced densification temperatures with smaller grained powders are likely caused by enhanced grain boundary dependent densification mechanisms that arise from smaller grain size. These results pave the way for possible use of sub 50nm reactants in place of larger grained precursors combined with additives, which have previously been shown to have a large effect on grain growth.

Finally, the flexibility of very fine nanopowders in conjunction with CAPAD processing procedures has yielded the potential for spinel with a variety of densities and microstructures, shown by highly porous and highly dense transparent nanocrystalline samples. Further investigation using reactants of similar grain sizes could enhance the understanding of the reaction kinetics and potentially allow for optimization/enhancement of the process.

Chapter 3 is co-authored by M. H. Shachar, Dr. Yasuhiro Kodera, and Professor Javier E. Garay, and is currently in preparation for submission to publish. The dissertation author was the primary investigator and author on this paper.

4. BROADBAND BLUE EMISSION IN TRANSPARENT, POLYCRYSTALLINE TITANIUM-DOPED SPINEL

4.1 Background and Introduction

Luminescent oxide ceramics have existing and potential uses for lighting [93], temperature measurement [94] and laser gain media [95]. The excellent thermal and mechanical properties of magnesium aluminate spinel (MAS, $MgAl_2O_4$) have made it one of the most successful high temperature optical-structural materials. The light emission properties in spinels have also been widely studied. Researchers have explored the doping of MAS single crystals with a variety of rare earths and transition metal ions, such as Tb^{3+} [96], Ni^{2+} [97], Cr^{3+} [98], and Mn^{2+} [72]. MAS polycrystalline ceramic doping and PL has also received attention [61], [62], [65]–[67]

Successful doping studies of $MgAl_2O_4$ single crystals with Ti have shown broadband emission, particularly interesting for tunable pulsed lasers [68]–[72]. These $Ti:MgAl_2O_4$ single crystals showed broad band emission centered around 455-465nm (FWHM ~100nm) and 805nm (FWHM ~200nm) when pumped with 266nm and 532nm, respectively[68], [71].

The use of blue luminescence for *in-situ* temperature monitoring in high temperatures is also interesting. Chambers and Clarke [99] showed that low wavelength emission is favorable for temperature monitoring because low wavelengths are out of the blackbody background inherent at high temperatures.

Titanium-doped Al_2O_3 (commonly known as titanium sapphire) is the most commercially successful tunable laser material. Doping Ti^{3+} into Al_2O_3 single crystals yields a laser crystal with one of the widest tunable emission bands (~600-1000nm), which also provides capabilities for producing very short pulse widths . However, the short radiative lifetime of $Ti:Al_2O_3$ of ~4 µs [74], [100] prohibits the use of flashlamp pumping as short pulses limit their lifetimes due to high peak

currents, providing motivation for exploration of different host materials for Ti-doping. In addition, alternative host materials can potentially allow for tunability at different emission ranges and alternative pumping schemes. Despite the successes with doping of single crystals with a variety of dopants, high temperatures (exceeding melting), long durations, and dopant gradients (axially and in pulling direction) are often encountered [75], [76].

The fast processing kinetics of Current-Activated, Pressure-Assisted Densification (CAPAD, also known as Spark Plasma Sintering) can yield doped transparent ceramics with homogeneous dopant distribution, out of equilibrium dopant concentrations, and fine-grained microstructures. [3], [11]. The capabilities of CAPAD for producing high quality laser-host materials can be seen in the work of Penilla *et al.*, where gain was demonstrated in CAPAD densified Nd:Al_2O_3. Researchers have also used CAPAD for successful consolidation of transparent $MgAl_2O_4$ with both rare-earth [61]–[65] and transition metal ions [66], [67]. However, consolidation of polycrystalline $MgAl_2O_4$ doped with Ti has yet to be shown.

In this work, reaction densification of Ti-doped $MgAl_2O_4$ is explored using metastable/nanocrystalline γ-Al_2O_3 and MgO as reactants for spinel formation, and Ti_2O_3 as a transition metal doping source. Previously, reaction densification has successfully produced high quality Nd:YAG via vacuum sintering [59] and Ce:YAG by CAPAD processing [86]. Use of reaction densification for the consolidation of $MgAl_2O_4$ has been previously explored by S. Meir *et al* using α-Al_2O_3 and MgO agglomerates. However, this method in conjunction with dopants remains unexplored. In addition, we are unaware of any published works on the densification and characterization of Ti:$MgAl_2O_4$ via CAPAD.

4.2 Experimental Procedure

4.2.1 Powder Processing

10nm $MgOH_2$ (99%, US res. Nano) was reacted in a box furnace at 10°C/min to 500°C in air for a total of 2 hours, to ensure full conversion to MgO. The powder was immediately placed under vacuum during cooling to decrease potential for moisture adsorption. Similar furnace steps were used for the preparation of γ-Al_2O_3 (<50nm, 99.99% purity, Inframat Advanced Materials). Upon cooling, powders were weighed 1:1 by mol and planetary ball milled in ultra-high purity water using Si_3N_4 media for 3 hours at 200 RPM. The resulting slurry was centrifuged, fully dried in a vacuum furnace, mortar and pestled, and sieved through 325 mesh. To remove absorbed moisture and possible hydroxide phase formation during planetary ball milling in H_2O, the mixed reactants were annealed at 500°C for 2 hours in air. The reactant powder was stored in vacuum until dopant incorporation.

Ti_2O_3 powder (Alpha Aesar, 99.8%) was dry planetary ball-milled for particle refinement at 300 RPM for 6 hours, redistributing every hour. The resulting Ti_2O_3 was incorporated into the reactant powder at varying atomic % (0, 0.25, 0.35, 0.75) using mortar and pestle and subsequently dry planetary ball milled at 200 RPM for 6 hours, redistributing every hour. The resulting Ti-doped reactant powder was mortar and pestled, sieved (325 mesh), and dried in air at 10°C/min to 500°C in air for a total of 2 hours. The doped reactant powder was stored in vacuum until densification.

4.2.2 CAPAD Procedure

The resulting Ti-doped reactant powder was packed in a graphite die with a 9.5 mm inner diameter, inserted into a larger die with 19mm inner diameter. The die and plunger assemblies

were uniaxially pressed at 100 MPa for 5 minutes at room temperature prior to densification in CAPAD. Transparency in Ti-doped polycrystalline $MgAl_2O_4$ was achieved at 100 °C/min to 1400 °C for 5 min using a two-step pressure application procedure similar to what is seen in [43]. The initial pressure (5 MPa) was maintained until 1350°C, where the final pressure was applied (100 MPa) and the hold temperature was reached. Temperature measurements were taken utilizing a pyrometer focused on the surface of the die containing powder through a hole drilled through the larger die assembly.

4.2.3 Microstructural Characterization

X-ray diffraction (XRD) of powder and bulk samples was performed using a Panalytical X'pert x-ray diffractometer. Microstructural characterization via scanning electron microscopy was done using a Zeiss Sigma 500 scanning electron microscope. Analysis of grain size occurred via measurement of micrographs of fractured surfaces, where the longest distances of a grain were measured for 300 random grains, for each micrograph.

4.2.4 Transparency and Photoluminescence Measurements

Densified samples were polished to 0.5 μm using diamond slurry prior to any spectroscopic measurements, to a final thickness of 1.1 +/- 0.05mm. Subsequent In-line transmission measurements were taken of using an Agilent Cary 5000 UV-VIS-NIR spectrophotometer from 300 to 2500nm.

PL was measured on a Horiba Spex Fluorog 3 Spectrophotometer, with the sample measured at 45° relative to the angle of incidence.

4.3 Results and Discussion

4.3.1 Powder Characterization

Figure 4.1. shows the SEM micrographs of the processed combined reactant mixture (**Fig. 4.1a**) along with the as-received Ti_2O_3 powder pre- and post-planetary ball-milling step (**Fig 4.1b.** and **Fig 4.1c.**, respectively). The dispersed reactant powder showed a very fine particle size, well below 30nm. Prior to refinement the Ti_2O_3 dopant powder particles exceed 1μm, which is reduced to <1μm after planetary ball milling for 6hr (**Fig. 4.1c**).
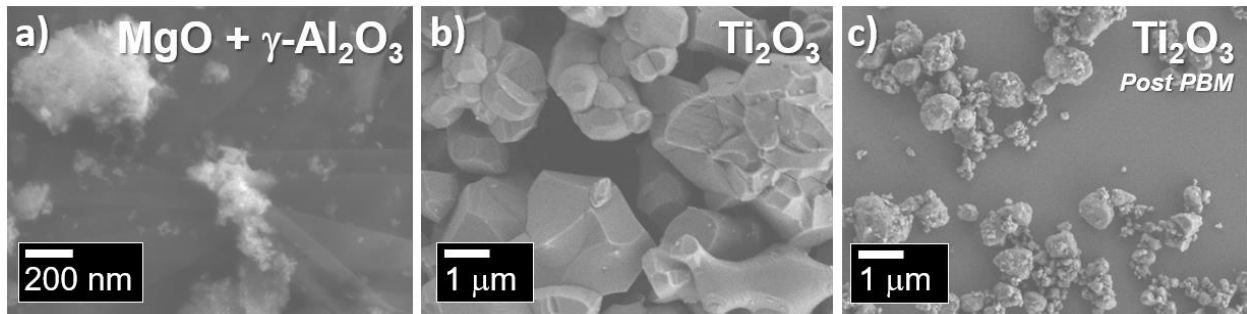
Figure 4.1. SEM Micrographs of dispersed reactant and dopant powders. **4.1a)** processed, combined MgO +γ-Al_2O_3 reactant powder **4.1b)** As-received Ti_2O_3 powder **4.1c)** refined Ti_2O_3 powder, post planetary ball
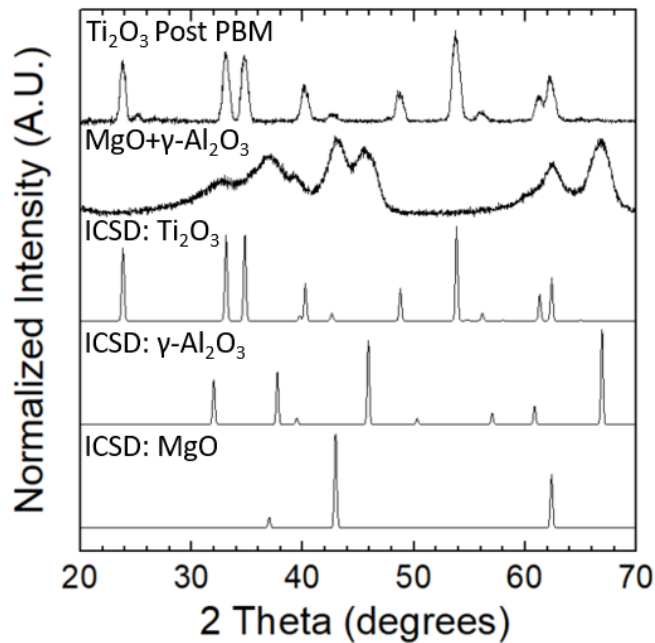
Figure 4.2. XRD of combined MgO +γ-Al_2O_3 reactant powder (MgO +γ-Al_2O_3) and PBM refined Ti_2O_3 dopant powder

XRD of the processed combined reactant mixture and Ti_2O_3 dopant was done to ensure phase purity prior to inclusion of dopant. **Figure 4.2** shows the resulting 2Θ scan of the combined reactant mixture and the Ti_2O_3 dopant where the peaks corresponding to the ICSD references of MgO and γ Al_2O_3 align with the peaks of the combined rea ctant mixture, and the ICSD reference for Ti_2O_3 aligns with the peaks corresponding to the refined Ti_2O_3 powder.

4.3.2 Effects of Water Adsorption on Transmission

Our previous experiments (Chapter 2 and [53]) showed that nanocrystalline MgO powder readily gains weight and can be explained by hydroxide formation (hydroxylation) of MgO particle surfaces that occurs spontaneously in the presence of H_2O. In order to assess the effect $Mg(OH)_2$ content on the reaction densification process, we exposed reactant powder mixtures to ambient atmosphere for prolonged time on the order of months. We will refer to the atmosphere exposed powders as *high Mg(OH)_2 content.*

Figure 4.3a. shows the CAPAD chamber (gas) pressure vs. temperature of combined reactant/dopant powder of varying dopant concentration that has been subjected to a final furnace step after dopant incorporation mentioned in section 2.1 (*annealed*), and a combined reactant/dopant *High Mg(OH)_2 content* powder.

A sharp increase in chamber pressure is shown at approximately $400°C$ in the experiment using *High Mg(OH)_2 content* powder, whereas the increase in chamber pressure is absent in the *annealed* powder. This spike in chamber pressure corresponds to de-hydroxilation occurring at around $400°C$, that we showed previously in [53]. **Figure 4.3b.** shows the effects of this pressure spike on the transmission of the bulk samples densified from powders subjected to these two

different processing conditions. In the samples densified from the powders which are not dried/immediately densified, a drastic decrease (>10%) in transmission arises.

We showed previously the effects of moisture adsorption on the densification rates of MgO [53], where exposure to moisture can be beneficial by enhanced densification rates due to enhanced particle rearrangement facilitated by de-hydroxylation. However, exposure to humidity for excessive durations yielded too high $Mg(OH)_2$ content, which was shown to be detrimental to densification. Decreased density was also encountered with increasing levels of moisture adsorption. This lower density and secondary phase formation is likely the cause of decreased light transmission seen in **Figure 4.3b.** It is also likely that water is adsorbed by γ-Al_2O_3 as is discussed in Chapter 3, and also contributes to increased porosity. The rest of the experiments discussed below use doped reactant powders dried well above the de-hydroxilation temperature and that were stored under vacuum until densification.
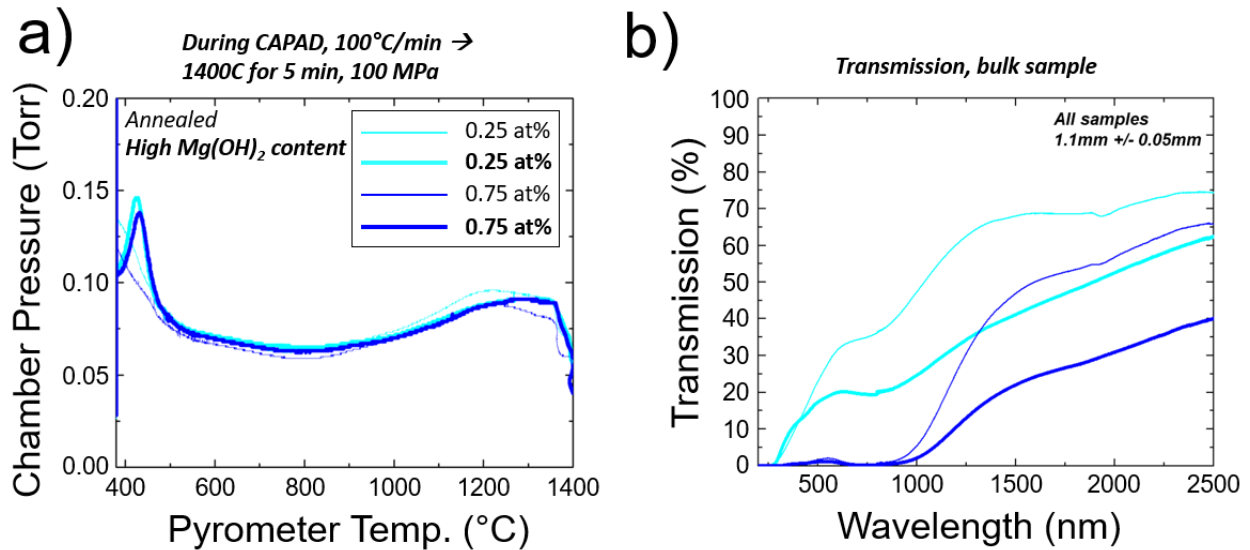
Figure 4.3. a) Chamber pressure (Torr) vs. Pyrometer temperature (°C) for *annealed* (thin line) and *high Mg(OH)₂ content* (thick line) Ti-doped MAS powders in densified in CAPAD. **b)** Corresponding Transmission (%) vs. Wavelength (nm) for densified samples from *annealed* and *high Mg(OH)₂ content* Ti-doped MAS powders

4.3.3 Bulk Sample Characterization

XRD of all bulk samples is shown in **Figure 4.4**, where ICSD references of individual reactants and $MgAl_2O_4$ are included for comparison. No evidence of reactant peaks are seen in any of the densified samples, indicating 1400°C for 5 minutes is sufficient for complete reaction to spinel regardless of doping concentration. Ti_2O_3 peaks are also absent in the XRD of Ti_2O_3 containing samples, indicating incorporation of the dopant into the host material. Previous Ti doping of MAS using single crystal production techniques showed Ti solubility in MAS. These XRD results confirm that MAS can also be doped by a solid-state reaction approach. Ti is multivalent and is stable at Ti^{3+} and Ti^{4+} and thus it should be more energetically favorable to dope onto the Al^{3+} sublattice in MAS rather than the Mg^{2+} where it would require charge compensation.
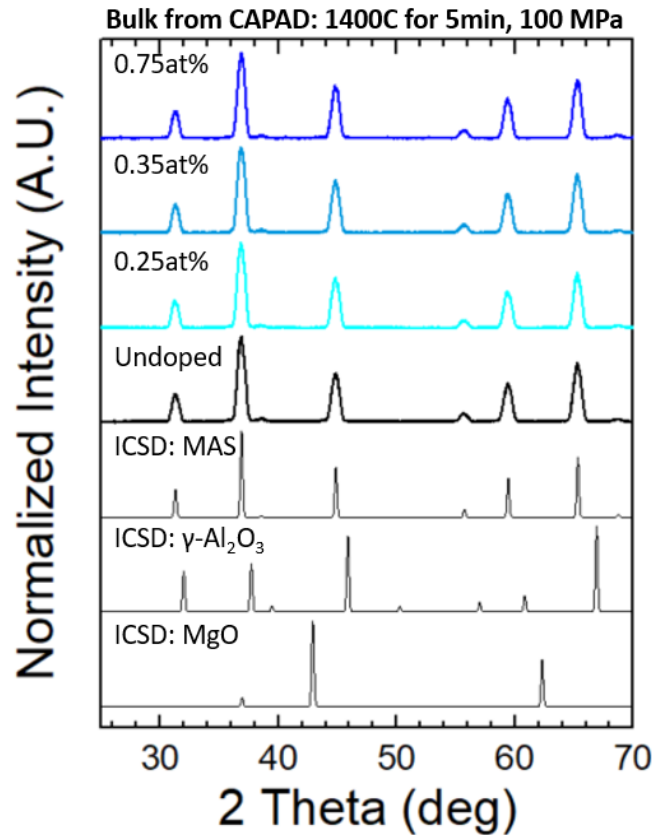
Figure 4.4 XRD of undoped and Ti-doped (varying concentrations) bulk samples densified in CAPAD at 1400C for 5min, 100 MPa. ICSD references included for comparison

Figure 4.5 shows fractured surfaces for CAPAD densified undoped MAS (**Fig. 4.5a**) and 0.75at% Ti:MAS. Both samples have equiaxed microstructures, with measured average grain sizes of 480nm and 577nm for undoped and 0.75at%, respectively. Neither sample micrograph showed evidence of observable porosity. Our previous results with undoped MAS (Chapter 3) showed that the MAS reaction occurs at temperatures below 1000°C, followed by the densification of reacted MAS at higher temperatures. Ti_2O_3 requires relatively low densification temperatures (<1000°C) by both conventional sintering and CAPAD [101]. It is likely that the Ti_2O_3 acts as a densification aid so that the doped samples reach full density at a lower temperature resulting in the slightly higher average grain size of the doped samples.
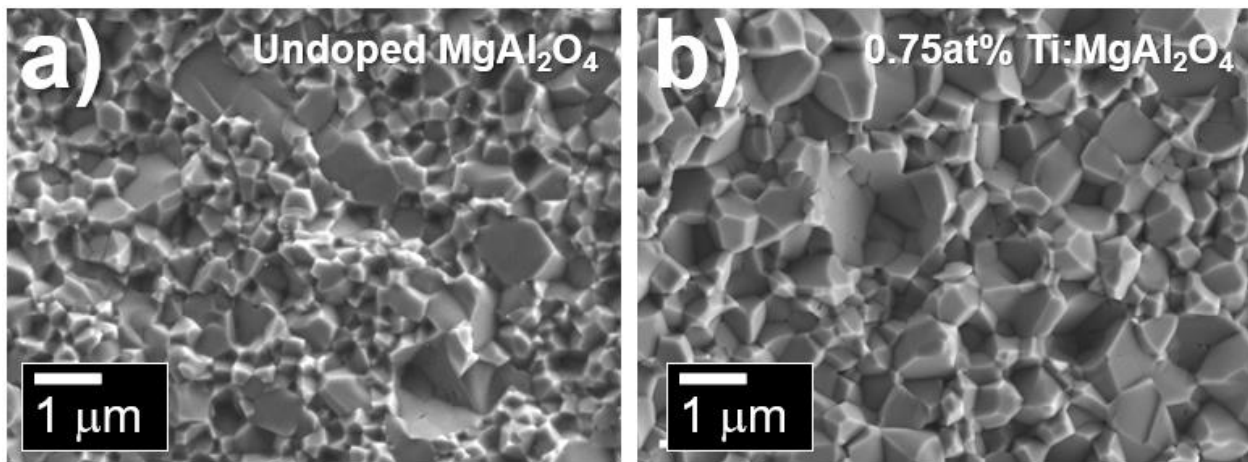
Figure 4.5. SEM micrographs of fractured surfaces of CAPAD densified samples from **a)** undoped MAS powder and **b)** 0.75at% Ti:MAS powder

4.3.4 Bulk Sample Transmission

In-line transmission vs. wavelength for undoped and doped samples is shown in **Figure 4.6a,** along with sample photos in **Figure 4.6b.** Reflection, absorption, and scattering all contribute to transmission losses. Th ae primary cause for scattering in a well-polished ceramic is porosity or birefringence, so high levels of transparency beyond 2000nm for all samples indicates

low microstructurally induced scattering. There is likely microstructural scattering at low wavelengths, but the primary differences between doped and un-doped MAS samples is wavelength dependent absorption, as discussed below.
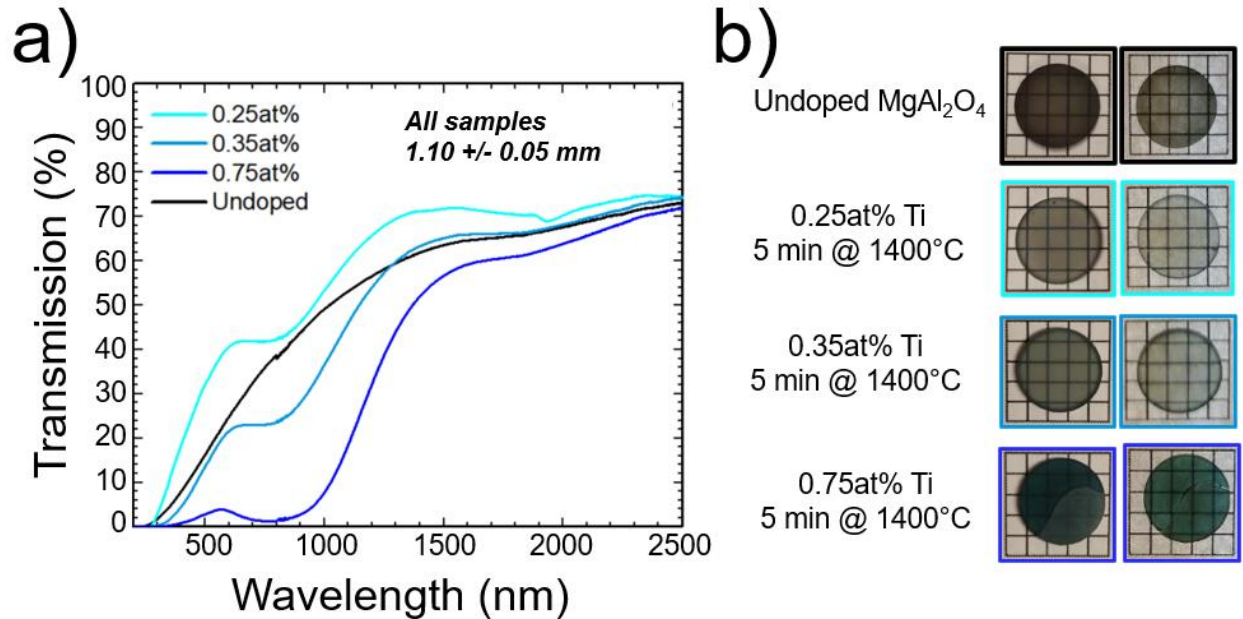
Figure 4.6. a) Transmission (%) vs. Wavelength (nm) for CAPAD densified undoped and Ti-doped MAS of varying concentrations. **b)** Corresponding sample photos for undoped and Ti-doped MAS CAPAD densified samples referred to in Chapter 4.

An apparent red shift of the absorption edge is seen with increasing dopant concentration. Similar red-shifts have been seen in Ti:MAS single crystals [69], [71], and have been previously attributed to charge-transfer between Ti^{3+} and Ti^{4+} ions.

The large absorption peak centered at ~ 790nm increases with increasing dopant concentration and is associated with the $Fe^{2+} + Ti^{4+} \rightarrow Fe^{3+} + Ti^{3+}$ charge transfer transition. This large absorption peak is seen in all previously doped Ti:MAS single crystal work [68], [71], [72] and Ti:Al_2O_3 [74], [76], [100], [102]. This particular charge transfer transition is the origin of the color in "blue sapphire"[103], and can also be seen in **Figure 4.6b** with increasing dopant concentration. Chemical analysis of the Ti_2O_3 powders indicates <5ppm Fe, which is likely the

source of the iron contamination. Ti:MAS single crystals grown in oxidizing atmosphere lack this large absorption peak at 790nm [69], [70], as do single Ti:MAS single crystals annealed in oxygen [71] after growth in oxygen free environment. The absence of this peak is likely caused by the oxidation of the Ti^{3+} and Fe^{2+} to Ti^{4+} and Fe^{3+} when exposed to high temperatures in the presence of oxygen.

Absorption corresponding to the Ti^{3+} cation corresponding to the $T_{2g} \rightarrow E_g$ electronic transition at ~490nm [68], [104], cannot be distinguished in the transmission data.

4.3.5 Photoluminescence

Figure 4.7a shows an excitation scan with emission held at 455nm. The emission intensity of the undoped sample peaks at approximately 240nm, whereas the emission intensity of the doped samples peaks at 270nm. **Figure 4.7b** shows emission when excited with 266nm. Emission of the doped samples peaks between 440-455nm, with an FWHM increasing with increasing dopant concentration from 162-181nm. Previous works of Ti:MAS grown in oxygen free environments show peaks centered from 455nm [71], [72] to 465nm [68]. S. Sawai *et al.* showed slight deviations in peak location with slight offsets in stoichiometry in $MgAl_2O_4$, which may explain the slight discrepancies with our results[105]. FWHM for Ti:MAS single crystals at these emission locations is ~100nm, which greatly differs from these results. The change in shape and width of the emission band was shown in the work of Penilla *et al.* in $Nd:Al_2O_3$, where polycrystalline samples were significantly more broad than their single crystal counterparts [95]. This change in peak shape and width is attributed to multi-site doping, where dopant ions exist within the grain interior, at grain boundaries, and at triple points. This feature of doped polycrystalline materials yields possibilities for enhanced tunability when compared to single crystals doped with similar ions. Y. Fuimoto *et*

al. suggests the large emission peak centered at ~710nm that exists in the undoped sample and decreases with increasing dopant concentration is attributed to a cation deficiency [93]. **Figure 4.7c** shows normalized emission peaks of **Figure 4.7b**, where no significant change in peak shape is seen.

Figure 4.7. Photoluminescence measurements of CAPAD densified undoped and Ti-doped MAS of varying concentrations: **a)** excitation scan, emission wavelength fixed at 455nm **b)** emission scan, excitation wavelength fixed at 266nm **c)** normalized emission peaks seen in **Fig. 4.7b**

Bausa *et al.* reports a very wide emission peak centered at 790nm when pumped with 532nm, attributed to the $T_{2g} \rightarrow E_g$. charge transition of Ti^{3+} cation [68]. It is unclear whether or not the large absorption at this region is causing this lack of measurable emission or the lack of Ti^{3+} ions in our samples. However, when pumped with 532nm, all CAPAD densified samples (undoped and doped) show a sharp emission peak at 689nm (**Figure 4.8b**). When emission is monitored at 689nm, an excitation scan shows two large peaks centered at ~390nm and 540nm (**Figure 4.8a**). These peak shapes and locations of both excitation and emission scans are nearly identical to the results shown in Cr:MAS single crystal spectroscopy shown by GH. Sun *et al.* [98], with further agreement in the emission data from Aizawa *et al.* [94]. The existence of these peaks confirms that Cr can be successfully incorporated into MAS using a solid-state reaction approach. Also, it confirms the successful demonstration of Cr,Ti co-doped polycrystalline MAS, which we do not believe has been previously reported. Note that this inadvertent Cr doping is not detrimental to the purpose of this study, which was obtaining blue emission confirmed in **Figure 4.7**. It is likely that

using purer powders would result in reduced Cr doping and remove the peak centered at 689nm. However, it is also likely that co-doped Cr,Ti:MAS could be useful as a multi-wavelength emitter operated using distinct pumping schemes.
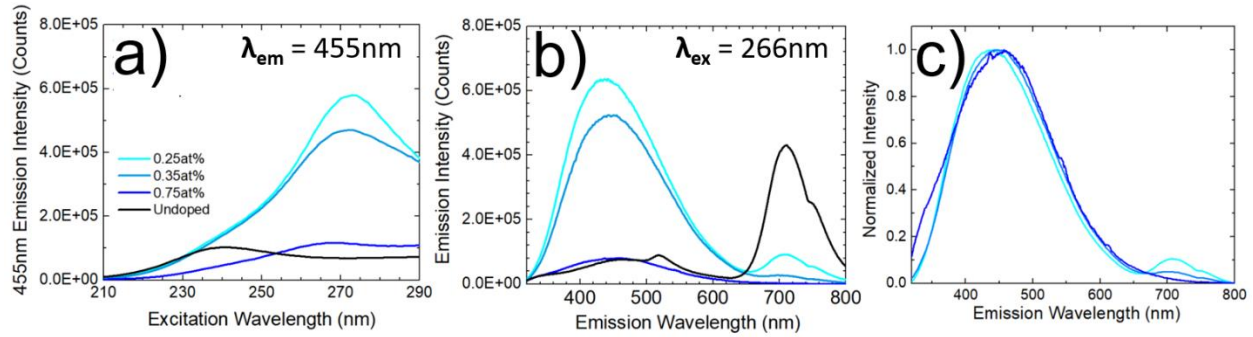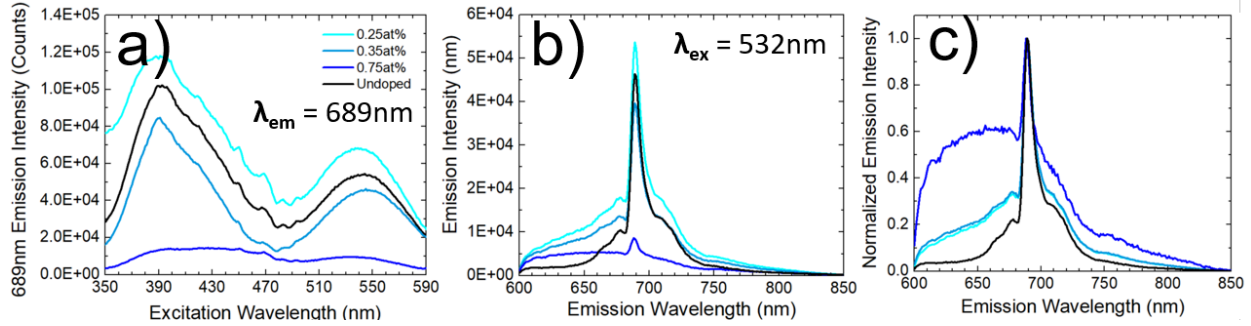

Figure 4.8. Photoluminescence measurements of CAPAD densified undoped and Ti-doped MAS of varying concentrations: **a)** excitation scan, emission wavelength fixed at 689nm **b)** emission scan, excitation wavelength fixed at 532nm **c)** normalized emission peaks seen in **Fig. 4.8b**

4.4 Chapter 4 Summary

CAPAD densified Ti-doped shows broad band blue emission, with broader peaks relative to Ti-doped single crystals. This dopant/host combination are capable of being used in applications where tunability in the visible range and short pulse width are necessary. In addition, blue emission in conjunction with the high melting temperature of $MgAl_2O_4$ yield possibility for integrated temperature measurement.

The flexibility of using nanocrystalline/metastable reactants and CAPAD is further emphasized with the additions of dopant and characterization of Ti:MAS by reaction densification. Chapter 4 also further emphasizes the importance that H_2O has on the consolidation of nanocrystalline oxide materials, observed in the decreased transmission in densified samples from powders allowed to adsorb significant levels of humidity.

Chapter 4 is co-authored by Dr. Yasuhiro Kodera, and Professor Javier E. Garay, and is currently in preparation for submission to publish. The dissertation author was the primary investigator and author on this paper.

5. SUMMARY AND CONCLUSIONS

Nanocrystalline ceramic oxides are a broad class of ceramics that are used in many different applications, of materials with varying densities, microstructures, and integrated dopants. Specifically, Al_2O_3, MgO, and $MgAl_2O_4$ are of interest due to their high melting temperatures and mechanical properties, leading to significant use as structural and optical ceramics. However, materials processing is typically use-specific, resulting in limited flexibility. In addition, typical use-specific consolidation techniques yield materials with large grain sizes in optical materials and large pore sizes in porous materials. In this work, we sought out to understand the consolidation of very fine nanocrystalline MgO and metastable γ-Al_2O_3. This work sought to first understand the effects of grain size and adsorption on hygroscopic oxide materials, then to effectively reaction densify a combination of these oxides to varying densities and microstructures. This route exhibited flexibility with the consolidation of fully dense transparent MAS and nanoporous MAS, from the same reactant powder. Using the lessons learned with initial densification studies and the effects of particular variables, successful inclusion of dopant into the reaction densified host was demonstrated and characterized.

Prior works by Meir *et al.* [52] showed flexibility of using reactants for the densification of $MgAl_2O_4$ in CAPAD, although larger grained/stable α-Al_2O_3 and agglomerated MgO resulted in very high temperatures or additives required for full density. Use of more metastable γ-Al_2O_3 in conjunction with MgO as reactants has been explored [84], and showed enhanced densification at lower temperatures, but a lack of information exists regarding the reaction evolution and kinetics. Use of metastable γ-Al_2O_3 and very fine nanocrystalline MgO should yield enhanced densification and reactivity. In addition, CAPAD has been shown to provide enhanced flexibility

in the production of materials with many different microstructures . However, investigations on CAPAD densification of this particular combination of powders has not occurred.

As both of these materials are hygroscopic and < 50nm, **Chapter 2** focused on understanding the effects of nanocrystallinity and adsorption on densification. It was found that enhanced densification rates occurred with decreasing grain sizes. Enhanced densification rates were shown at lower temperatures with exposure of nanocrystalline powders to humidity, which had detrimental effects on density with increasing exposure. However, short durations of exposure to moisture showed both enhanced densification rates and negligible effects on sample densities when compared to samples densified from completely dry powders.

The understanding of moisture effects was crucial to the success of the reaction densification in metastable γ-Al_2O_3 and very fine nanocrystalline MgO – both of which have been shown to have very active surfaces capable of adsorption. **Chapter 3** showed the reaction densification of dry, metastable/nanocrystalline reactants yielded enhanced reaction and densification at significantly lower temperatures than previously experienced in larger grained experiments – provoked by cation vacancies in γ-Al_2O_3 and defected non-stoichiometric $MgAl_2O_4$, similar structures in γ-Al_2O_3 and $MgAl_2O_4$, and short diffusion distances in nanocrystalline reactants. The flexibility of this particular route was shown in the production of materials of very high densities, or partially dense materials with nanopores.

The capabilities of this route were further exemplified by inclusion of dopant into mentioned reactants, which has yet to be attempted using metastable reactants and CAPAD. **Chapter 4** focused on the doping of metastable/nanocrystalline reactant powder with Ti, which has been previously shown to have broad emission in Ti:Al_2O_3 and could potentially yield broad emission at different locations or allow different pumping schemes upon doping in alternative

hosts. Polycrystalline Ti:MAS was shown to have broad blue emission, with wider emission than single crystal counterpart – likely due to multi-site doping.

This work demonstrated the capabilities of hygroscopic, metastable, and very fine nanocrystalline powders for the flexible consolidation of $MgAl_2O_4$. These processing techniques and findings will likely be advantageous to any materials scientist working with nanocrystalline/metastable oxide powders, porous materials, or highly dense materials.

APPENDIX

A-1 MgAl₂O₄ Calibration Curve

The figure shows a plot of Mol Ratio MAS versus Peak Area Ratio, MAS. An inset table contains the following fit information:

Equation	y = Intercept + B1*x^1 + B2*x^		
Weight	No Weighting		
Residual Sum of Squares	0.0020 6		
Adj. R-Square	0.9983		
		Value	Standard Err
	Intercep	0	--
J	B1	0.0993	0.07098
	B2	0.8893	0.08209
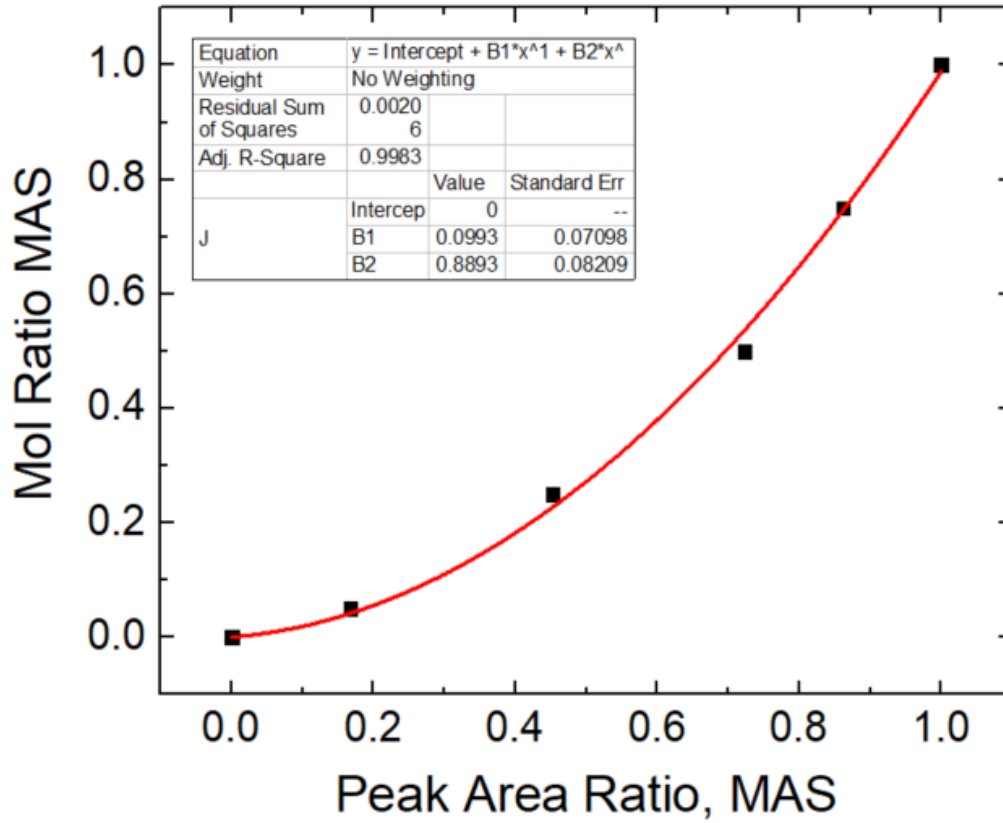
Figure A-1. Mol ratio vs. Peak Area ratio for varying mol% of $MgAl_2O_4$, mixed with equal mol% reactants. Fitted line provides estimate of mol ratio MAS corresponding to particular peak area measured using XRD.

A-2. A Simple Geometric Model to Determine Kinetics of Spinel Growth
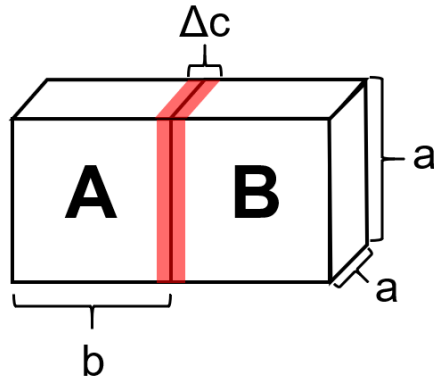
$$\Delta c = \sqrt{2kt}$$

where k = rate constant

$$V_c = a^2 \Delta c$$

$$V_c = a^2 \sqrt{2kt}$$

$$\text{Volume Fraction} = \chi_c = \frac{V_c(t)}{V_{total}} = \frac{a^2 \cdot \sqrt{2kt}}{a^2 \cdot 2b}$$

Assume total volume constant

$$\boxed{\chi_c = \frac{\sqrt{2kt}}{2b}}$$

Figure A-2. Simple geometric model for spinel growth, assuming planar interface and diffusion-controlled growth.

REFERENCES

[1] R. L. Coble, "Transparent Alumina and Method of Preparation," 1962.

[2] A. Ikesue, I. Furusato, and K. Kamata, "Fabrication of Polycrystalline, Transparent YAG Ceramics by Solid-State Reaction Method," J. Am. Ceram. Soc., vol. 78, no. 1, pp. 225–228, 1995.

[3] Y. Kodera, C. L. Hardin, and J. E. Garay, "Transmitting , emitting and controlling light : Processing of transparent ceramics using current-activated pressure-assisted densification," Scr. Mater., vol. 69, no. 2, pp. 149–154, 2013, doi: 10.1016/j.scriptamat.2013.02.013.

[4] J. McBain, The Sorption ofGases and Vapours by Solids. George Routledge & Sons, Ltd: London, 1932.

[5] Knez, Mato, Roland Scholz, Kornelius Nielsch, Eckhard Pippel, Dietrich Hesse, Margit Zacharias, and Ulrich Gösele. "Monocrystalline spinel nanotube fabrication based on the Kirkendall effect." Nature materials 5, no. 8 (2006): 627-631.

[6] X. Hou, S. Qing, Y. Liu, L. Li, Z. Gao, and Y. Qin, "Enhancing effect of MgO modification of Cu-Al spinel oxide catalyst for methonol steam reforming," Int. J. Hydrogen Energy, vol. 45, no. 1, pp. 477–489, 2020.

[7] M. M. S. Wahsh, R. M. Khattab, N. M. Khalil, F. Gouraud, M. Huger, and T. Chotard, "Fabrication and technological properties of nanoporous spinel/forsterite/zirconia ceramic composites," Mater. Des., vol. 53, pp. 561–567, 2014, doi: 10.1016/j.matdes.2013.07.059.

[8] L. Han, F. Li, X. Yao, L. Dong, M. Luo, H. Zhang, Q. Jia, and S. Zhang., "Fabrication of porous MgAl2O4 ceramics using V2O5 as sintering additive," Ceram. Int., vol. 46, no. 14, pp. 22819–22825, 2020, doi: 10.1016/j.ceramint.2020.06.049.

[9] X. Deng, J. Wang, J. Liu, H. Zhang, L. Han, and S. Zhang, "Low cost foam-gelcasting preparation and characterization of porous magnesium aluminate spinel (MgAl2O4) ceramics," Ceram. Int., vol. 42, no. 16, pp. 18215–18222, 2016, doi: 10.1016/j.ceramint.2016.08.145.

[10] S. Hashimoto, S. Honda, T. Hiramatsu, and Y. Iwamoto, "Fabrication of porous spinel (MgAl2O4) from porous alumina using a template method," Ceram. Int., vol. 39, no. 2, pp. 2077–2081, 2013, doi: 10.1016/j.ceramint.2012.08.062.

[11] J. E. Garay, "Current-activated, pressure-assisted densification of materials," Annu. Rev. Mater. Res., vol. 40, pp. 445–468, 2010, doi: 10.1146/annurev-matsci-070909-104433.

[12] A. Gatti, "Development of a process for producing transparent spinel bodies," Gen. Electr. CO PHILADELPHIA PA Sp. DIV, 1969., 1969.

[13]   C. J. Ting and H. Y. Lu, "Hot-pressing of magnesium aluminate spinel - I. Kinetics and densification mechanism," Acta Mater., vol. 47, no. 3, pp. 817–830, 1999, doi: 10.1016/S1359-6454(98)00400-5.

[14]   A. Krell, J. Klimke, and T. Hutzler, "Advanced spinel and sub-μm Al2O3 for transparent armour applications," J. Eur. Ceram. Soc., vol. 29, no. 2, pp. 275–281, 2009, doi: 10.1016/j.jeurceramsoc.2008.03.024.

[15]   R. Chaim, Z. Shen, and M. Nygren, "Transparent nanocrystalline MgO by rapid and low-temperature spark plasma sintering," J. Mater. Res., vol. 19, no. 9, pp. 2527–2531, 2004, doi: 10.1557/JMR.2004.0334.

[16]   T. B. Tran, S. Hayun, A. Navrotsky, and R. H. R. Castro, "Transparent nanocrystalline pure and Ca-doped MgO by spark plasma sintering of anhydrous nanoparticles," J. Am. Ceram. Soc., vol. 95, no. 4, pp. 1185–1188, 2012, doi: 10.1111/j.1551-2916.2012.05103.x.

[17]   S. Wakahara, T. Yanagida, Y. Yokota, Y. Fujimoto, V. Chani, M. Sugiyama, Y. Futami, and A. Yoshikawa., "Phosphorescent luminescence of pure magnesium oxide transparent ceramics produced by spark plasma sintering," Opt. Mater. (Amst)., vol. 35, no. 3, pp. 558–562, 2013, doi: 10.1016/j.optmat.2012.10.028.

[18]   N. Jiang, R. jun Xie, Q. Liu, and J. Li, "Fabrication of sub-micrometer MgO transparent ceramics by spark plasma sintering," J. Eur. Ceram. Soc., vol. 37, no. 15, pp. 4947–4953, 2017, doi: 10.1016/j.jeurceramsoc.2017.06.021.

[19]   S. Li, C. Song, X. Qin, and Z. Zeng, "Densification and grain growth behavior of highly dense MgO ceramics in pressureless sintering," Ceram. Int., vol. 41, no. 8, pp. 10148–10151, 2015, doi: 10.1016/j.ceramint.2015.04.115.

[20]   D. Ehre, E. Y. Gutmanas, and R. Chaim, "Densification of nanocrystalline MgO ceramics by hot-pressing," J. Eur. Ceram. Soc., vol. 25, no. 16, pp. 3579–3585, 2005, doi: 10.1016/j.jeurceramsoc.2004.09.023.

[21]   M. N. Rahaman, "Hydrothermal synthesis and sintering of ultrafine Ceo2 powders," J. Mater. Res., vol. 8, no. 7, pp. 1680–1686, 1993, doi: 10.1557/JMR.1993.1680.

[22]   K. Itatani, R. Yasuda, F. S. Howell, and A. Kishioka, "Effect of starting particle size on hot-pressing of magnesium oxide powder prepared by vapour-phase oxidation process," J. Mater. Sci., vol. 32, no. 11, pp. 2977–2984, 1997, doi: 10.1023/A:1018649222749.

[23]   J. Reis and R. Chaim, "Densification maps for spark plasma sintering of nanocrystalline MgO ceramics: Particle coarsening and grain growth effects," Mater. Sci. Eng. A, vol. 491, no. 1–2, pp. 356–363, 2008, doi: 10.1016/j.msea.2008.02.011.

[24]   E. Artz, "The influence of an increasing particle coordination on the densification of spherical powders," Acta Metall., vol. 30, no. 10, pp. 1883–1890, 1982, doi: 10.1016/0001-6160(82)90028-1.

[25] P. J. Anderson, and P. L. Morgan, "Effects of Water Vapour on Sintering of MgO," Trans. Faraday Soc., vol. 44, no. 12, pp. 930–937, 1991.

[26] J. A. Varela and O. J. Whittemore, "Structural Rearrangement During the Sintering of MgO," J. Am. Ceram. Soc., vol. 66, no. 1, pp. 77–82, 1983, doi: 10.1111/j.1151-2916.1983.tb09973.x.

[27] P. F. Eastman and I. B. Cutler, "Effect of Water Vapor on Initial Sintering of Magnesia," J. Am. Ceram. Soc., vol. 49, no. 10, pp. 526–530, 1966, doi: 10.1111/j.1151-2916.1966.tb13156.x.

[28] J. P. Maria, X. Kang, R. D. Floyd, E. C. Dickey, H. Guo, J. Guo, A. Baker, S. Funihashi, and C. A. Randall., "Cold sintering: Current status and prospects," J. Mater. Res., vol. 32, no. 17, pp. 3205–3218, 2017, doi: 10.1557/jmr.2017.262.

[29] J. Nie, Y. Zhang, J. M. Chan, R. Huang, and J. Luo, "Water-assisted flash sintering: Flashing ZnO at room temperature to achieve ~ 98% density in seconds," Scr. Mater., vol. 142, pp. 79–82, 2018, doi: 10.1016/j.scriptamat.2017.08.032.

[30] A. S. Helle, K. E. Easterling, and M. F. Ashby, "Hot-isostatic pressing diagrams: New developments," Acta Metall., vol. 33, no. 12, pp. 2163–2174, 1985, doi: 10.1016/0001-6160(85)90177-4.

[31] R. Suryanarayanan Iyer and S. M. L. Sastry, "Consolidation of nanoparticles - development of a micromechanistic model," Acta Mater., vol. 47, no. 10, pp. 3079–3098, 1999, doi: 10.1016/S1359-6454(99)00116-0.

[32] L. C. De Jonghe and M. N. Rahaman, "Sintering of Ceramics," Handbook of Advanced Ceramics: Materials, Applications, Processing and Properties, vol. 1–2. pp. 187–264, 2003, doi: 10.1016/B978-012654640-8/50006-7.

[33] R. M. German, Thermodynamic and Kinetic Treatments. 2014.

[34] K. Morita, B. N. Kim, H. Yoshida, and K. Hiraga, "Spark-plasma-sintering condition optimization for producing transparent MgAl2O4 spinel polycrystal," J. Am. Ceram. Soc., vol. 92, no. 6, pp. 1208–1216, 2009, doi: 10.1111/j.1551-2916.2009.03074.x.

[35] J. E. Alaniz, A. D. Dupuy, Y. Kodera, and J. E. Garay, "Effects of applied pressure on the densification rates in current-activated pressure-assisted densification (CAPAD) of nanocrystalline materials," Scr. Mater., vol. 92, pp. 7–10, 2014, doi: 10.1016/j.scriptamat.2014.07.015.

[36] C. Bruch, "Transparent Magnesia-Alumina Spinel and Method to Produce," United States Pat. Off., pp. 1–3, 1971.

[37] I. Reimanis and H. J. Kleebe, "A review on the sintering and microstructure development of transparent spinel (MgAl 2O 4)," J. Am. Ceram. Soc., vol. 92, no. 7, pp. 1472–1480, 2009, doi: 10.1111/j.1551-2916.2009.03108.x.

[38] I. Ganesh, "A review on magnesium aluminate (MgAl2O4) spinel: Synthesis, processing and applications," Int. Mater. Rev., vol. 58, no. 2, pp. 63–112, 2013, doi: 10.1179/1743280412Y.0000000001.

[39] A. Goldstein, "Correlation between MgAl 2O 4-spinel structure, processing factors and functional properties of transparent parts (progress review)," J. Eur. Ceram. Soc., vol. 32, no. 11, pp. 2869–2886, 2012, doi: 10.1016/j.jeurceramsoc.2012.02.051.

[40] Z. Shi, Q. Zhao, B. Guo, T. Ji, and H. Wang, "A review on processing polycrystalline magnesium aluminate spinel (MgAl2O4): Sintering techniques, material properties and machinability," Mater. Des., vol. 193, p. 108858, 2020, doi: 10.1016/j.matdes.2020.108858.

[41] M. Sokol, B. Ratzker, S. Kalabukhov, M. P. Dariel, E. Galun, and N. Frage, "Transparent Polycrystalline Magnesium Aluminate Spinel Fabricated by Spark Plasma Sintering," Adv. Mater., vol. 30, no. 41, pp. 1–11, 2018, doi: 10.1002/adma.201706283.

[42] K. Morita, B. N. Kim, K. Hiraga, and H. Yoshida, "Fabrication of transparent MgAl2O4 spinel polycrystal by spark plasma sintering processing," Scr. Mater., vol. 58, no. 12, pp. 1114–1117, 2008, doi: 10.1016/j.scriptamat.2008.02.008.

[43] C. Wang and Z. Zhao, "Transparent MgAl2O4 ceramic produced by spark plasma sintering," Scr. Mater., vol. 61, no. 2, pp. 193–196, 2009, doi: 10.1016/j.scriptamat.2009.03.039.

[44] M. Sokol, S. Kalabukhov, M. P. Dariel, and N. Frage, "High-pressure spark plasma sintering (SPS) of transparent polycrystalline magnesium aluminate spinel (PMAS)," J. Eur. Ceram. Soc., vol. 34, no. 16, pp. 4305–4310, 2014, doi: 10.1016/j.jeurceramsoc.2014.07.022.

[45] N. Frage, S. Cohen, S. Meir, S. Kalabukhov, and M. P. Dariel, "Spark plasma sintering (SPS) of transparent magnesium-aluminate spinel," J. Mater. Sci., vol. 42, no. 9, pp. 3273–3275, 2007, doi: 10.1007/s10853-007-1672-0.

[46] A. Rothman, S. Kalabukhov, N. Sverdlov, M. P. Dariel, and N. Frage, "The effect of grain size on the mechanical and optical properties of spark plasma sintering-processed magnesium aluminate spinel MgAl2O 4," Int. J. Appl. Ceram. Technol., vol. 11, no. 1, pp. 146–153, 2014, doi: 10.1111/j.1744-7402.2012.02849.x.

[47] Y. Mordekovitz, L. Shelly, M. Halabi, S. Kalabukhov, and S. Hayun, "The effect of lithium doping on the sintering and grain growth of SPS-processed, non-stoichiometric magnesium aluminate spinel," Materials (Basel)., vol. 9, no. 6, 2016, doi: 10.3390/ma9060481.

[48] A. Talimian, V. Pouchly, K. Maca, and D. Galusek, "Densification of magnesium aluminate spinel using manganese and cobalt fluoride as sintering aids," Materials (Basel)., vol. 13, no. 1, 2020, doi: 10.3390/MA13010102.

[49] G. R. Villalobos, J. S. Sanghera, and I. D. Aggarwal, "Degradation of magnesium aluminum spinel by lithium fluoride sintering aid," J. Am. Ceram. Soc., vol. 88, no. 5, pp. 1321–1322, 2005, doi: 10.1111/j.1551-2916.2005.00209.x.

[50] B. Hallstedt, "Thermodynamic Assessment of the System MgO–Al2O3," J. Am. Ceram. Soc., vol. 75, no. 6, pp. 1497–1507, 1992, doi: 10.1111/j.1151-2916.1992.tb04216.x.

[51] A. Alhaji, M. H. Taherian, S. Ghorbani, and S. A. Sharifnia, "Development of synthesis and granulation process of MgAl2O4 powder for the fabrication of transparent ceramic," Opt. Mater. (Amst)., vol. 98, no. October, p. 109440, 2019, doi: 10.1016/j.optmat.2019.109440.

[52] S. Meir, S. Kalabukhov, N. Froumin, M. P. Dariel, and N. Frage, "Synthesis and densification of transparent magnesium aluminate spinel by SPS processing," J. Am. Ceram. Soc., vol. 92, no. 2, pp. 358–364, 2009, doi: 10.1111/j.1551-2916.2008.02893.x.

[53] D. M. Dewitt, Y. Kodera, and J. E. Garay, "High (10−3 s−1)densification rates at <0.25 homologous temperature in pressure assisted densification of nanocrystalline MgO: Effects of water absorption and grain size," Scr. Mater., vol. 169, pp. 33–37, 2019, doi: 10.1016/j.scriptamat.2019.04.020.

[54] W. P. Whitney and V. S. Stubican, "Interdiffusion studies in the system MgOAl2O3," J. Phys. Chem. Solids, vol. 32, no. 2, pp. 305–312, 1971, doi: 10.1016/0022-3697(71)90015-1.

[55] P. Zhang, T. Debroy, and S. Seetharaman, "Interdiffusion in the MgO-Al2O3 spinel with or without some dopants," Metall. Mater. Trans. A Phys. Metall. Mater. Sci., vol. 27, no. 8, pp. 2105–2114, 1996, doi: 10.1007/BF02651865.

[56] E. B. Watson and J. D. Price, "Kinetics of the reaction MgO + Al2O3 → MgAl2O4 and Al-Mg interdiffusion in spinel at 1200 to 2000°C and 1.0 to 4.0 GPa," Geochim. Cosmochim. Acta, vol. 66, no. 12, pp. 2123–2138, 2002, doi: 10.1016/S0016-7037(02)00827-X.

[57] K. J. D. Mackenzie, R. K. Banerjee, and M. R. Kasaai, "Effect of electric fields on solid-state reactions between oxides - Part 1 Reaction between calcium and aluminium oxides," J. Mater. Sci., vol. 14, no. 2, pp. 333–338, 1979, doi: 10.1007/BF00589823.

[58] S. Sinhamahapatra, M. Shamim, H. S. Tripathi, A. Ghosh, and K. Dana, "Kinetic modelling of solid state magnesium aluminate spinel formation and its validation," Ceram. Int., vol. 42, no. 7, pp. 9204–9213, 2016, doi: 10.1016/j.ceramint.2016.03.017.

[59] A. Ikesue, T. Kinoshita, K. Kamata, and K. Yoshida, "Fabrication and Optical Properties of High-Performance Polycrystalline Nd:YAG Ceramics for Solid-State Lasers," Journal of the American Ceramic Society, vol. 78, no. 4. pp. 1033–1040, 1995, doi: 10.1111/j.1151-2916.1995.tb08433.x.

[60] E. H. Penilla, Y. Kodera, and J. E. Garay, "Blue-green emission in terbium-doped alumina (Tb:Al2O 3) transparent ceramics," Adv. Funct. Mater., vol. 23, no. 48, pp. 6036–6043, 2013, doi: 10.1002/adfm.201300906.

[61] D. Valiev, O. Khasanov, S. Stepanov, E. Dvilis, and V. Paygin, "MgAl2O4 ceramics doped with rare earth ions: Synthesis and luminescent properties," AIP Conf. Proc., vol. 2174, no. December, pp. 2–7, 2019, doi: 10.1063/1.5134413.

[62] D. Valiev, O. Khasanov, E. Dvilis, S. Stepanov, E. Polisadova, and V. Paygin, "Luminescent properties of MgAl2O4 ceramics doped with rare earth ions fabricated by spark plasma sintering technique," Ceram. Int., vol. 44, no. 17, pp. 20768–20773, 2018, doi: 10.1016/j.ceramint.2018.08.076.

[63] D. Valiev, S. Stepanov, O. Khasanov, E. Dvilis, E. Polisadova, and V. Paygin, "Synthesis and optical properties of Tb3+ or Dy3+-doped MgAl2O4 transparent ceramics," Opt. Mater. (Amst)., vol. 91, no. March, pp. 396–400, 2019, doi: 10.1016/j.optmat.2019.03.049.

[64] M. M. Hasan, P. P. Dholabhai, S. Dey, B. P. Uberuaga, and R. H. R. Castro, "Reduced grain boundary energies in rare-earth doped MgAl2O4 spinel and consequent grain growth inhibition," J. Eur. Ceram. Soc., vol. 37, no. 13, pp. 4043–4050, 2017, doi: 10.1016/j.jeurceramsoc.2017.04.073.

[65] R. Boulesteix, A. Maître, K. Lemański, and P. J. Dereń, "Structural and spectroscopic properties of MgAl2O4:Nd3+ transparent ceramics fabricated by using two-step Spark Plasma Sintering," J. Alloys Compd., vol. 722, pp. 358–364, 2017, doi: 10.1016/j.jallcom.2017.06.101.

[66] A. Wajler, A. Kozłowska, M. Nakielska, K. Leśniewska-Matys, A. Sidorowicz, D. Podniesiński, and P. Putyra., "Nonlinear absorption of submicrometer grain-size cobalt-doped magnesium aluminate transparent ceramics," J. Am. Ceram. Soc., vol. 97, no. 6, pp. 1692–1695, 2014, doi: 10.1111/jace.12965.

[67] M. Sokol, S. Kalabukhov, and N. Frage, "Fabrication of Polycrystalline Transparent Co+2: MgAl2O4 by a Combination of Spark Plasma Sintering (SPS) and Hot Isostatic Pressing (HIP) Processes," MATEC Web Conf., vol. 109, pp. 2–7, 2017, doi: 10.1051/matecconf/201710903002.

[68] L. E. Bausá, I. Vergara, J. García-Solé, W. Strek, and P. J. Deren, "Laser-excited luminescence in Ti-doped MgAl2O4 spinel," J. Appl. Phys., vol. 68, no. 2, pp. 736–740, 1990, doi: 10.1063/1.346807.

[69] T. Sato, M. Shirai, K. Tanaka, Y. Kawabe, and E. Hanamura, "Strong blue emission from Ti-doped MgAl2O4 crystals," J. Lumin., vol. 114, no. 2, pp. 155–161, 2005, doi: 10.1016/j.jlumin.2004.12.016.

[70] E. Hanamura, Y. Kawabe, H. Takashima, T. Sato, and A. Tomita, "Optical Properties of Transition-Metal Doped Spinels," J. nonlinear Opt. Phys. Mater., 2003.

[71] A. Jouini, H. Sato, A. Yoshikawa, T. Fukuda, G. Boulon, G. Panczer, K. Kato, and E. Hanamura., "Ti-doped MgAl2O4 spinel single crystals grown by the micro-pulling-down method for laser application: Growth and strong visible blue emission," J. Mater. Res., vol. 21, no. 9, pp. 2337–2344, 2006, doi: 10.1557/jmr.2006.0280.

[72] A. Jouini, A. Yoshikawa, A. Brenier, T. Fukuda, and G. Boulon, "Optical properties of transition metal ion-doped MgAl2O 4 spinel for laser application," Phys. Status Solidi Curr. Top. Solid State Phys., vol. 4, no. 3, pp. 1380–1383, 2007, doi: 10.1002/pssc.200673872.

[73] A. J. H. Macke, "Investigations on the luminescence of titanium-activated stannates and zirconates," J. Solid State Chem., vol. 18, no. 4, pp. 337–346, 1976, doi: 10.1016/0022-4596(76)90116-X.

[74] P. F. Moulton, "Spectroscopic and laser characteristics of Ti:Al_2O_3," J. Opt. Soc. Am. B, vol. 3, no. 1, p. 125, 1986, doi: 10.1364/josab.3.000125.

[75] Jouini A. (2007) MgAl2O4 Spinel Laser Crystals: Pure and Ti-, Mn-, or Ni-Doped. In: Fukuda T., Chani V.I. (eds) Shaped Crystals. Advances in Materials Research, vol 8. Springer, Berlin, Heidelberg. https://doi.org/10.1007/978-3-540-71295-4_13

[76] A. Nehari, A. Brenier, G. Panzer, K. Lebbou, J. Godfroy, S. Labo, H. Legal, G. Cheriaux, J. P. Chambaret, T. Duffar, and R. Moncorge., "Ti-doped sapphire (Al2O3) single crystals grown by the kyropoulos technique and optical characterizations," Cryst. Growth Des., vol. 11, no. 2, pp. 445–448, 2011, doi: 10.1021/cg101190q.

[77] Y. Yan, M. F. Chisholm, G. Duscher, A. Maiti, S. J. Pennycook, and S. T. Pantelides, "Impurity-induced structural transformation of a mgo grain boundary," Phys. Rev. Lett., vol. 81, no. 17, pp. 3675–3678, 1998, doi: 10.1103/PhysRevLett.81.3675.

[78] A. Goldstein, A. Goldenberg, Y. Yeshurun, and M. Hefetz, "Transparent MgAl2O4 spinel from a powder prepared by flame spray pyrolysis," J. Am. Ceram. Soc., vol. 91, no. 12, pp. 4141–4144, 2008, doi: 10.1111/j.1551-2916.2008.02788.x.

[79] A. Goldstein, A. Goldenberg, and M. Vulfson, "Development of a technology for the obtainment of fine grain size, transparent MgAl2O4 spinel parts," J. Ceram. Sci. Technol., vol. 2, no. 1, pp. 1–8, 2011, doi: 10.4416/JCST2010-00018.

[80] G. Bonnefont, G. Fantozzi, S. Trombert, and L. Bonneau, "Fine-grained transparent MgAl2O4 spinel obtained by spark plasma sintering of commercially available nanopowders," Ceram. Int., vol. 38, no. 1, pp. 131–140, 2012, doi: 10.1016/j.ceramint.2011.06.045.

[81] T. J. Barton, L. M. Bull, W. G. Klemperer, D. A. Low, B. McEnaney, M. Misono, P. A. Monson, G. Pez, G. W. Scherer, J. C. Vartuli, and O. M. Yaghi., "Tailored porous materials," Chem. Mater., vol. 11, no. 10, pp. 2633–2656, 1999, doi: 10.1021/cm9805929.

[82]   L. M. Rueschhoff, L. A. Baldwin, R. Wheeler, M. J. Dalton, H. Koerner, J. D. Berrigan, N. M. Bedford, S. Seifert, M. K. Cinibulk, and M. B. Dickerson., "Fabricating Ceramic Nanostructures with Ductile-like Compression Behavior via Rapid Self-Assembly of Block Copolymer and Preceramic Polymer Blends," ACS Appl. Nano Mater., vol. 2, no. 1, pp. 250–257, 2019, doi: 10.1021/acsanm.8b01820.

[83]   R. Wischert, P. Laurent, C. Copéret, F. Delbecq, and P. Sautet, "γ-Alumina: The essential and unexpected role of water for the structure, stability, and reactivity of 'defect' sites," J. Am. Chem. Soc., vol. 134, no. 35, pp. 14430–14449, 2012, doi: 10.1021/ja3042383.

[84]   D. Han, J. Zhang, P. Liu, and S. Wang, "Effect of polymorphism of Al2O3 on the sintering and microstructure of transparent MgAl2O4 ceramics," Opt. Mater. (Amst)., vol. 71, pp. 62–65, 2017, doi: 10.1016/j.optmat.2016.06.016.

[85]   D. Han, J. Zhang, P. Liu, G. Li, and S. Wang, "Densification and microstructure evolution of reactively sintered transparent spinel ceramics," Ceram. Int., vol. 44, no. 10, pp. 11101–11108, 2018, doi: 10.1016/j.ceramint.2018.03.109.

[86]   E. H. Penilla, Y. Kodera, and J. E. Garay, "Simultaneous synthesis and densification of transparent, photoluminescent polycrystalline YAG by current activated pressure assisted densification (CAPAD)," Mater. Sci. Eng. B Solid-State Mater. Adv. Technol., vol. 177, no. 14, pp. 1178–1187, 2012, doi: 10.1016/j.mseb.2012.05.026.

[87]   F. Wang, J. Ye, G. He, G. Liu, Z. Xie, and J. Li, "Preparation and characterization of porous MgAl2O4 spinel ceramic supports from bauxite and magnesite," Ceram. Int., vol. 41, no. 6, pp. 7374–7380, 2015, doi: 10.1016/j.ceramint.2015.02.044.

[88]   D. V. Dudina, B. B. Bokhonov, and E. A. Olevsky, "Fabrication of porous materials by spark plasma sintering: A review," Materials (Basel)., vol. 12, no. 3, 2019, doi: 10.3390/ma12030541.

[89]   J. Dong, J. Wang, L. Shi, J. Yang, J. Wang, B. Shan, and M. Shen., "Hydrogenous spinel γ-alumina structure," Phys. Chem. Chem. Phys., vol. 19, no. 40, pp. 27389–27396, 2017, doi: 10.1039/c7cp04704e.

[90]   M. H. Shachar, G. Uahengo, E. H. Penilla, Y. Kodera, and J. E. Garay, "Modeling the effects of scattering and absorption on the transmission of light in polycrystalline materials," J. Appl. Phys., vol. 128, no. 8, 2020, doi: 10.1063/5.0014937.

[91]   K. Morita, B. N. Kim, H. Yoshida, K. Hiraga, and Y. Sakka, "Spectroscopic study of the discoloration of transparent MgAl2O4 spinel fabricated by spark-plasma-sintering (SPS) processing," Acta Mater., vol. 84, pp. 9–19, 2015, doi: 10.1016/j.actamat.2014.10.030.

[92]   V. Nečina and W. Pabst, "Transparent MgAl2O4 spinel ceramics prepared via sinter-forging," J. Eur. Ceram. Soc., Feb. 2021, doi: 10.1016/j.jeurceramsoc.2021.02.017.

[93]   Y. Fujimoto, H. Tanno, K. Izumi, S. Yoshida, S. Miyazaki, M. Shirai, K. Tanaka, Y. Kawabe, and E. Hanamura., "Vanadium-doped MgAl2O4 crystals as white light source," J. Lumin., vol. 128, no. 3, pp. 282–286, 2008, doi: 10.1016/j.jlumin.2007.07.022.

[94]   H. Aizawa, N. Ohishi, S. Ogawa, E. Watanabe, T. Katsumata, S. Komuro, T. Morikawa, and E. Toba., "Characteristics of chromium doped spinel crystals for a fiber-optic thermometer application," Rev. Sci. Instrum., vol. 73, no. 8, p. 3089, 2002, doi: 10.1063/1.1491998.

[95]   E. H. Penilla, L. F. Devia-Cruz, M. A. Duarte, C. L. Hardin, Y. Kodera, and J. E. Garay, "Gain in polycrystalline Nd-doped alumina: Leveraging length scales to create a new class of high-energy, short pulse, tunable laser materials," Light Sci. Appl., vol. 7, no. 1, 2018, doi: 10.1038/s41377-018-0023-z.

[96]   Y. Takebuchi, H. Fukushima, T. Kato, D. Nakauchi, N. Kawaguchi, and T. Yanagida, "Dosimetric properties of Tb-doped MgAl 2 O 4 Single Crystals," Jpn. J. Appl. Phys., vol. 59, no. 052007, pp. 1–5, 2020.

[97]   N. V. Kuleshov, V. G. Shcherbitsky, V. P. Mikhailov, S. Kück, J. Koetke, K. Petermann, and G. Huber.., "Spectroscopy and excited-state absorption of Ni2+-doped MgAl2O4," J. Lumin., vol. 71, no. 4, pp. 265–268, 1997, doi: 10.1016/S0022-2313(96)00284-0.

[98]   G. H. Sun, Q. L. Zhang, J. Q. Luo, W. P. Liu, X. F. Wang, S. Han, L. L. Zheng, W. M. Li, and D. L. Sun., "Bulk Crystal Growth of Cr-doped MgAl2O4 spinel by Czochralski method and properties characterization," Mater. Chem. Phys., vol. 204, pp. 277–281, 2018, doi: 10.1016/j.matchemphys.2017.10.049.

[99]   M. D. Chambers and D. R. Clarke, "Doped oxides for high-temperature luminescence and lifetime thermometry," Annu. Rev. Mater. Res., vol. 39, pp. 325–359, 2009, doi: 10.1146/annurev-matsci-112408-125237.

[100]   R. C. Powell, J. L. Caslavsky, Z. AlShaieb, and J. M. Bowen, "Growth, characterization, and optical spectroscopy of Al2O3:Ti3+," J. Appl. Phys., no. 58, pp. 2331–2336, 1998, doi: https://doi.org/10.1063/1.335955.

[101]   P. Angerer, L. G. Yu, K. A. Khor, and G. Krumpel, "Spark-plasma-sintering (SPS) of nanostructured and submicron titanium oxide powders," Mater. Sci. Eng. A, vol. 381, no. 1–2, pp. 16–19, 2004, doi: 10.1016/j.msea.2004.02.009.

[102]   M. Yamaga, T. Yosida, S. Hara, N. Kodama, and B. Henderson, "Optical and electron spin resonance spectroscopy of Ti 3+ and Ti 4+ in Al 2 O 3," J. Appl. Phys., vol. 75, pp. 1111–1117, 1994, doi: https://doi.org/10.1063/1.356494.

[103]   K. Nassau, "The Origins of Color in Minerals," Am. Mineral., vol. 63, pp. 219–229, 1978.

[104]   D. S. McClure, "The distribution of transition metal cations in spinels," J. Phys. Chem. Solids, vol. 3, no. 3–4, pp. 311–317, 1957, doi: 10.1016/0022-3697(57)90034-3.

[105] S. Sawai and T. Uchino, "Visible photoluminescence from MgAl2O4 spinel with cation disorder and oxygen vacancy," J. Appl. Phys., vol. 112, no. 10, 2012, doi: 10.1063/1.4767228.

[106] K. Wall and A . Sanchez, "Titanium sapphire laser.," Lincoln Lab. J., vol. 3, no. 3, pp. 447–462, 1990, doi: 10.2184/lsj.21.73.